ULTRA-HIGH PRECISION GRINDING OF BK7 GLASS

By

Onwuka, Goodness Raluchukwu
(214006611)

A dissertation submitted in fulfilment of the requirements for the Degree: Master of Engineering (Mechatronics)

in

The Faculty of Engineering, Information Technology and the Built Environment

at the

Nelson Mandela Metropolitan University

March 2016

Promoter: Prof. Khaled Abou-El-Hossein

DECLARATION

I, **Onwuka, Goodness Raluchukwu** hereby declare that:

- The work done in this thesis is my own;
- All sources used or referred to have been documented and recognized; and
- This thesis has not been previously submitted in full or partial fulfilment of the requirements for an equivalent or higher qualification at any other educational institution.

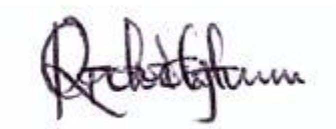

Author's Signature Date: 18th March 2016

DEDICATION

To everyone who faced setbacks and challenges in life but still had the courage to rise up, fight and endure the process of learning how to win after failing. This treatise is dedicated to the Sun in all its admirable glory, whose unfailing rising teaches us to hope and reach out for the opportunities embedded in each new day. To the beauty of the sun in its regalia, presiding over the affairs of the solar system and establishing a controlled balance in our sphere of existence.

Finally, this work is dedicated to the creator of the sun whose impeccable wisdom and understanding is experienced in the beautiful and sustainable creativity all around us. You sustain ALL things by the power of Your word.

ACKNOWLEDGEMENT

Wholehearted gratitude goes to my indefatigable promoter, Prof. Khaled Abou-El-Hossein, for his guidance, support and mentorship throughout the period of the research. I would like to appreciate the entire research team in the Ultra-high Precision Machining Laboratory for the support, thoughtful input and ideas all through the course of the study. Peter Odedeyi, you joined our team at very strategic time, you are God sent.

I would also like to appreciate National Research Foundation of South Africa and the Research capacity Development at NMMU for the financial support to actualize this study.

To my parents Mr and Mrs Peter Onwuka, Rev. Clem and Patricia Emekene, words cannot be enough to express my gratitude. To my immediate and extended family, thanks for standing by me and supporting me through difficult times.

Special gratitude to the staff of the Centre for Teaching Learning and Media/student academic development (CTLM), in the likes of Ronelle Plaatjes, Samantha Greef, Fransesco de Vega and the ever willing Selwyn Milborrow for providing their strong shoulders for standing on. Truly, I now see farther because you are giants in experience and wisdom. You are the best team!! And to the Manliness guard dogs, thanks for doing life with me at this phase of my journey.

I remain grateful to all my friends – Ajoke Emekene, Kayode Ayankoya, Chinedu Ahia, Marchello Dontoni, Sisa Pazzi, Ife Fashoro, Emmanuel Oreva, John Fernandes, Tega Okiti and Andrew Thuo for the wise counsel, timely intervention and for providing shoulders to lean on during difficult times. And to those who time and space may not permit me to mention, I appreciate you all. Thank you.

ABSTRACT

With the increase in the application of ultra-precision manufactured parts and the absence of much participation of researchers in ultra-high precision grinding of optical glasses which has a high rate of demand in the industries, it becomes imperative to garner a full understanding of the production of these precision optics using the above-listed technology. Single point inclined axes grinding configuration and Box-Behnken experimental design was developed and applied to the ultra-high precision grinding of BK7 glass. A high sampling acoustic emission monitoring system was implemented to monitor the process. The research tends to monitor the ultra-high precision grinding of BK7 glass using acoustic emission which has proven to be an effective sensing technique to monitor grinding processes. Response surface methodology was adopted to analyze the effect of the interaction between the machining parameters: feed, speed, depth of cut and the generated surface roughness. Furthermore, back propagation Artificial Neural Network was also implemented through careful feature extraction and selection process. The proposed models are aimed at creating a database guide to the ultra-high precision grinding of precision optics.

LIST OF ABBREVIATIONS

1	UHPG	Ultra-High Precision Grinding
2	UPG	Ultra-precision Grinding
3	AE	Acoustic Emission
4	SPIA	Single Point Inclined Axes Grinding
5	MRR	Material Removal Rate
6	FEA	Finite Element Analysis
7	SMPM	Surface Meter Per Minute
8	ARM	Autoregressive modelling
9	SS	Spectral Subtraction
10	ANN	Artificial Neural Network
11	FFT	Fast Fourier Transform
12	STFT	Short Time Fourier Transform
13	DFT	Discrete Fourier Transform
14	WAVEDEC	Wavelet Decomposition
15	BK7	Borosilicate 7
16	BPNN	Back Propagation Neural Network.
17	2FI	Two Factor Interaction
18	BBD	Box-Behnken Design
19	ELID	Electrolytic In Process Dressing

TABLE OF CONTENTS

LIST OF FIGURES

LIST OF TABLES

CHAPTER ONE
INTRODUCTION

1.1: PREFACE

Borosilicate crown glass was invented in the 19th century by the famous German glassmaker Otto Schott. Hence the emergence of the name Schott-Bk7 glass (1). Over the years, there has been a lot of development in its manufacturing process and an increase in its applications. It contains at least 5% boric acid and other chemical compounds like silicon oxide, aluminum oxide and sodium oxide in their various proportions (1). This glass is a high-quality technical workpiece, it is commonly used due to its special inherent properties like being practically bubble and inclusion free. Furthermore, it possesses a clear and colorless appearance with a low amount of inclusions, etcetera (2-4).

Asides the inherent properties mentioned above, Bk7 glass possesses unique mechanical, optical and physical characteristics which include its resistance to chemical and environmental damage, excellent transmission range in the visible and infrared spectra down to 350nm, low coefficient of thermal expansion making it resistant to thermal shock and good scratch resistance. These combined unique mechanical characteristics and stable chemical properties of Bk7 glass make it a desirable workpiece coupled with the fact that no special treatment is required for grinding and polishing it, but it's hard and brittle nature is a major disadvantage creating a reason for concern in precision grinding (3, 5).

The importance of Bk7 glass in our environment cannot be over-emphasized as it has found application in many areas. For example, in optics: as precision lens, achromatic doublets, laser optics and reflecting telescopes. In implantable medical devices: as artificial hip joints, bone cement, prosthetic eyes, dental composite materials and breast implants. In electronics and semiconductor industry: as commercial transmitters and microelectromechanical systems. Other areas include sensor and measurement technology, substrates for mirror and filter coating, neuro-stimulators for treatment of epilepsy, physiological sensors and veterinary tracking devices (6, 7)

1.2: BACKGROUND TO RESEARCH

Ultra-high precision grinding (UHPG) is a cutting edge technology that has fast replaced conventional grinding techniques and is fast replacing more recent techniques like ultra-precision grinding. There is a current increase in the demand for ductile machined and advanced brittle engineering materials like silicon, tungsten carbide, borosilicate 7 glass, borosilicate 9 glass and other optical glasses. The reason for this increase is because these materials are being used in the semiconductor, telecommunications, microelectronics, automotive and defence industries to manufacture silicon chips, optical lens for night vision, micro electro mechanical systems. These materials are machined to tight stringent requirements involving mirror surface finishes, nanometric surface roughness values and very low form deviations in order to be used in such applications. These stringent requirements can be met by applying ultra-precision grinding techniques.

One of the major drawbacks in UHPG is insufficient data on process monitoring and optimization of the process as it is not a highly researched area. Therefore, there is a need to create a data bank to efficiently predict the process and determine optimum parameters for specific surface roughness results. The research focuses on implementing acoustic emission sensing technique to effectively monitor the ultra-high precision grinding of Borosilicate 7 glass. Furthermore, the acquired signals are processed and important features extracted from them. These extracted features are used as a basis for machine learning inputs using neural networks to characterize and predict the surface roughness. In conclusion, the research drives towards the sustainability and optimization of the ultra-high precision grinding of advanced engineering materials.

1.3: STATEMENT OF THE PROBLEM

Previously glass was ground conventionally only at fracture mode to an average surface roughness of a few microns. This introduced micro cracks on the ground surface, as a result glass was termed difficult to machine. Final finishing was done using lapping or polishing processes to achieve desired surface integrity but this could be time-consuming and expensive depending on the magnitude of subsurface damage involved. Over the last decade, research in the field of ductile mode grinding of hard and brittle materials has fostered the grinding of glass to Nano-metric surface finish levels in ductile mode while maintaining good form accuracy. As a result of this development, the focus is mainly on cost and time savings in achieving high surface integrity hence it is now of huge importance to optimize the traditional process employed in generating high surface integrity with little or no need for finishing processes (8, 9). However, the development in the fields of ultra-high precision machining does not have enough existing literature especially in the area of ultra-high precision grinding of optical glasses.

1.4: STUDY OBJECTIVES

This research aimed at monitoring the ultra-precision grinding of BK7 glass through Acoustic Emission sensing technique implemented by a high-resolution data acquisition system and optimizing the process to determine optimum grinding parameters for good surface finishes.

The research will monitor ultra-precision grinding of BK7 glass at different stages using a different combination of process parameters to generate different surface roughness values to link the generated surface roughness to the acquired AE data. The developed high-resolution acoustic sensing technique will enable effective monitoring and prediction of the ultra-precision grinding of BK7 and other hard and brittle materials. Also, the research is expected to develop a response surface model that will determine the relationship between the process parameters and surface roughness.

The following objectives were identified for the research:

i. Conduct a concise literature survey on ultra-high precision grinding and process monitoring of optical glass grinding.
ii. Develop a sensor based AE data acquisition system with virtual instrumentation for monitoring the ultra-high precision grinding process.
iii. Create a response surface model to link the machining parameters to the generated surface roughness to be able to determine the optimal selection of parameters
iv. Signal processing and feature extraction from acquired AE signals
v. Implement neural network to predict surface roughness values.

1.6: SCOPE OF STUDY

The research will serve as a guide for the single point inclined axes grinding of Bk7 glass to help decipher the appropriate grinding parameters required for an optimal surface integrity and also develop the application of AE techniques for suitable monitoring of the ultra-high precision process. However the scope of the research is clarified as follows:

I. Surface integrity measurements will be limited to the average surface roughness parameter. No measurement of surface damage or microscopic observation in the form of micrographs will be carried out. Subsurface damage will only be prevented as much as possible through the careful selection of appropriate grinding parameters.

II. The acoustic emission set up will implement a single sensor setup and not multiple sensors. Sensor fusion technique will not be employed in the monitoring process.

1.7: HYPOTHESIS

Null hypothesis:

I. Acoustic Emission sensing technique is not suitable to monitor the ultra-high precision grinding of Bk7 glass.

II. Response surface modeling is not suitable to analyze and predict the effect of machining parameters in the ultra-high precision grinding of bk7 glass.

1.8: SIGNIFICANCE OF RESEARCH

Currently, there is little or no available literature relating to the ultra-high precision grinding of BK7 optical glass. Since the goal of precision grinding is to reach the minimum surface roughness with the least machining steps the research will be useful in developing a model that will achieve this amongst others and also bridge the literature gap in the specified field of study which will serve as a data bank. Also, the research will be able to develop a neural network training and prediction scheme through monitoring with AE sensing technique.

1.9: STRUCTURE OF THESIS

Chapter 2 describes the optical glass grinding process and classifies the ultra-high precision grinding process according to the different material removal rates and obtainable precisions including determinants of ductile mode machining concept and extends to the monitoring of the grinding process with acoustic emission sensing. Chapter 3 details the experimental design and setup while the detailed analysis of results and observations can be found in chapter 4. This chapter also includes the development of a response surface model, signal processing and neural network scheme for predicting the surface roughness values. Chapter 5 concludes the findings in the research and highlights suggested recommendations for future improvement on the research (Figure 1.1).

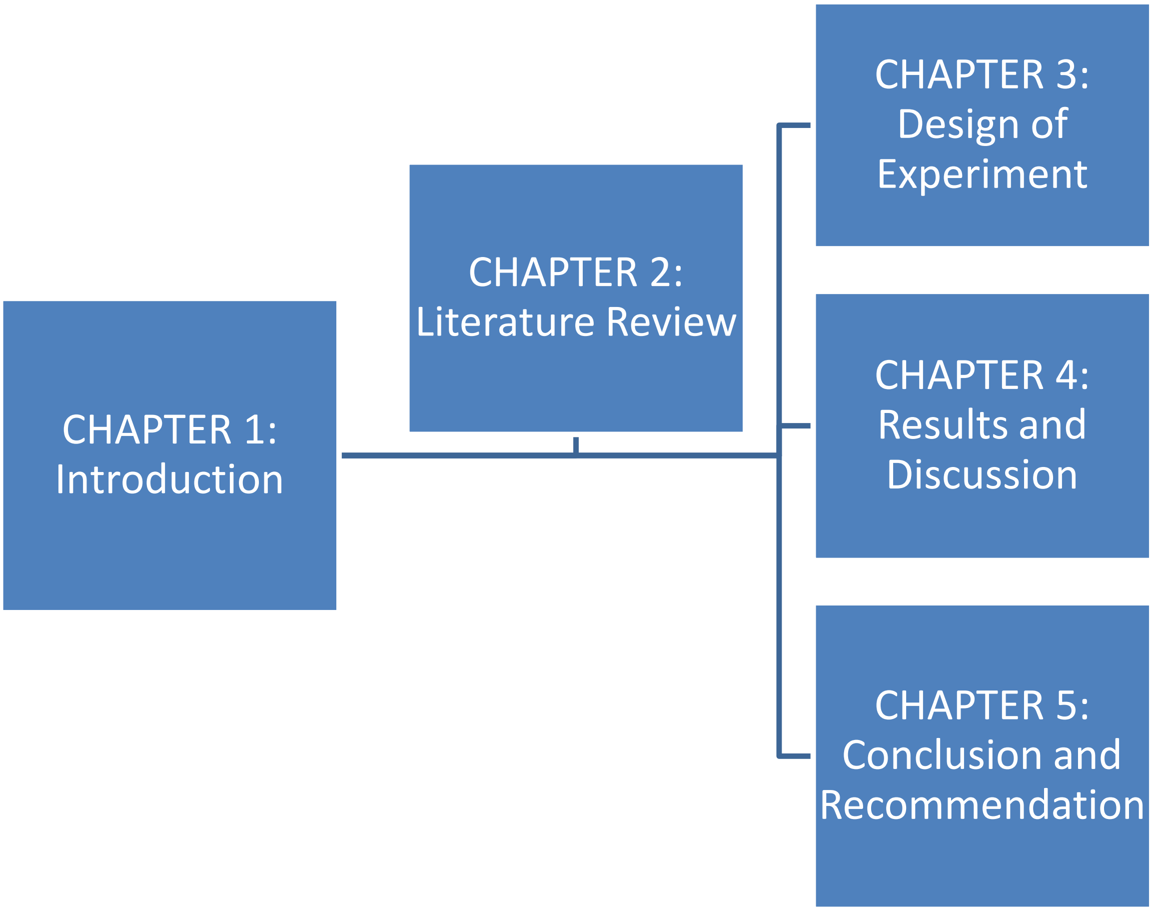

Figure 1.1: Organisational structure of the thesis

CHAPTER TWO
LITERATURE REVIEW

2.1: INTRODUCTION

The literature survey in this chapter dwells on the principles, concepts and developing technology involved in grinding optical glass. Furthermore, process monitoring techniques are highlighted with emphasis on acoustic emission sensing technique and the development of neural networks.

2.2: GRINDING OF OPTICAL GLASS

The mechanical properties of a workpiece and the required part quality of the workpiece are yardsticks for determining the abrasive process to be used in machining the workpiece(10). Glass which is brittle and hard is usually machined by ultra-precision grinding. Ultra-precision grinding of glass is an abrasive process which requires the use of fine grain wheels, wear-resistant abrasives, low run-out spindles and machine tools with high loop stiffness (10). Grinding of hard and brittle materials like glass, ceramic and semiconductors by an abrasive process is more complex and probabilistic especially since high precision parts are required, unlike precision cutting of ferrous metals which is highly predictable (10).Due to the nature of glass, grinding initiates micro cracks which deteriorate surface quality hence glass was previously ground conventionally at a hundred percent brittle fracture.

The concept of glass grinding has evolved over the years as a result of the development of ultra-precision machining and introduction of the ductile mode machining concept which has increased the achievable tight tolerances necessary to actualise grinding of optical glass. Hence, it can be rightly said that the concept of modern glass grinding and its evolution cannot be fully grasped without an understanding of the unique but interrelated concepts of precision engineering, precision machining, accuracy and ductile mode machining. A combination of precision machining systems and the ductile mode theory facilitates mirror like surface finish on hard and brittle materials without the need for several subsequent polishing processes (11).

2.2.1: Brief overview of precision machining

From Nakazawa's point of view, the intensively researched precision engineering field strictly concerns the creation, design, fabrication and measurements involved with highly precise machine tools (12). On the other hand, Venkatesh quoted Mc keown's view on the subject matter which goes beyond the mere creation of high-precision machinery to involve a collection of engineering, scientific skills and techniques which evolved over four decades in response to the ever-increasing applications of metrology to precision machining (13). As a result, the concept of precision expands to accommodate precision processing of materials, control systems and unmanned machining with CAD and CAM systems, plus information processing systems. Hence, it is correct to state that application of precision machining in optics ranges from the manufacture of extremely large telescopes to microchips and micro-optical flats.

2.2.2: Precision and accuracy

The term precision is normally confused with accuracy, it is necessary to clarify these terms for the sake of understanding precision machining. Accuracy in a layman's term is the ability to hit what is aimed at. It is the degree of conformity of the measured dimension with its true magnitude whereas precision is the repeatability of a process. In other words, precision is the degree with which an instrument can give the same value when repeated measurement of the same limits and standards are made (13). In the manufacturing of optical glass, a combination of these two terms comes into play. Beyond hitting the targeted requirements, the system should be able to continually repeat the process at the same required accuracy.

2.3: CLASSIFICATION OF MACHINING

Japanese researcher Norio Taniguchi is credited for classifying machining and defining many of the terms used in micro-scale manufacturing today. Based on achievable machining accuracy he classified machining as follows:

I. Normal or conventional machining
II. Precision machining
III. High-precision machining
IV. Ultra precision machining

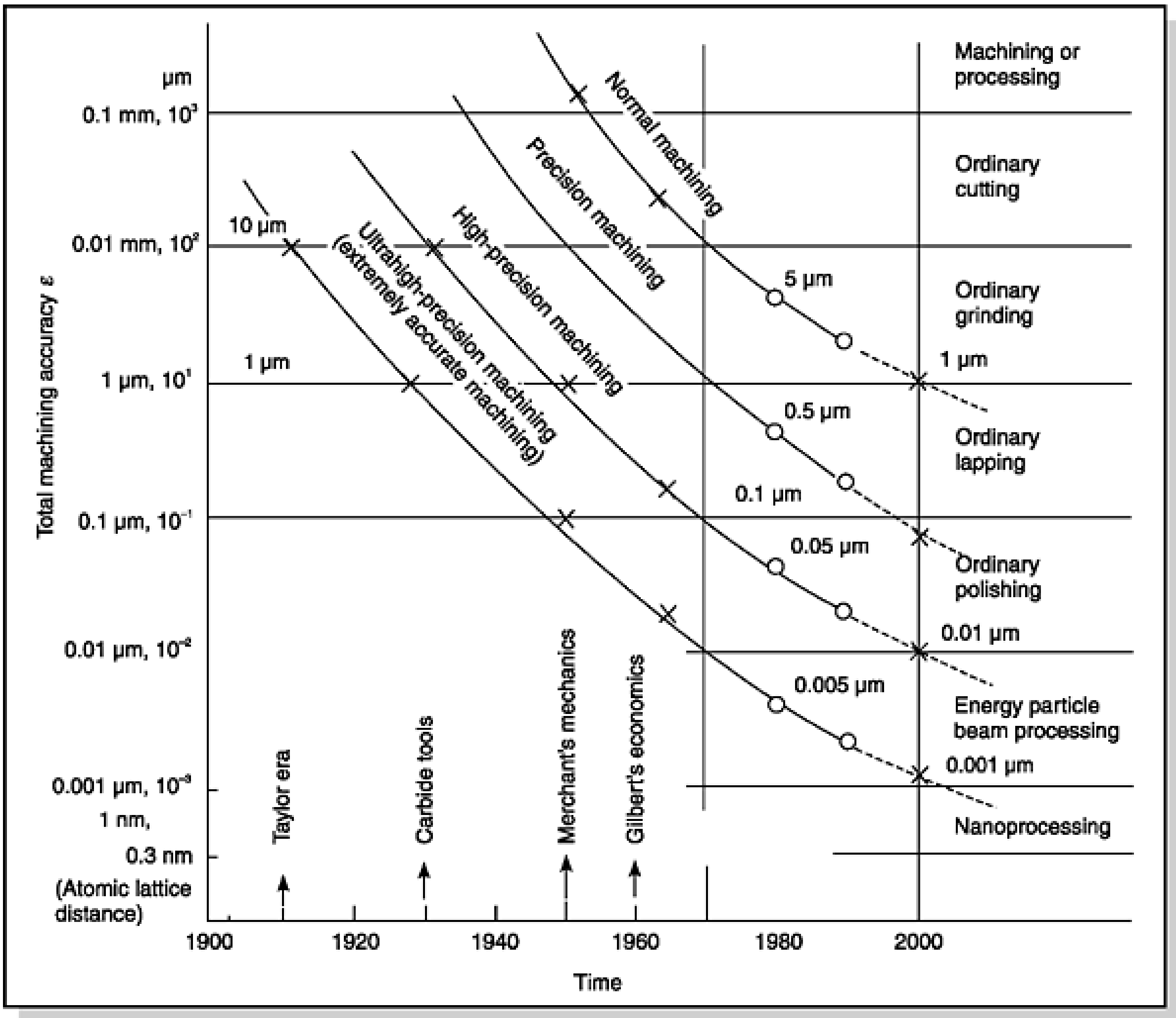

Figure 2.1: Modified Taniguchi's curve with decade intervals (13).

Figure 2.1 is the modified form of Taniguchi's chart by Venkatesh showing the historical progression of achievable machining accuracy over the last century. Taniguchi defined ultra-precision machining as a process by which the highest possible dimension accuracy is or has been achieved at a given point in time having dimension tolerance of 0.01μm and achievable average surface roughness of 0.001 μm (14). From Taniguchi's curve (Figure 2.1), the increase in achievable machining accuracy increasess with time and it is evident that ultra-precision accuracy in a previous dispensation can be regarded as normal machining accuracy in a more recent dispensation for the same country or region.

2.3.1 Evolution of precision grinding

Although the evolution of diamond turning has not attained the desired ultimate stage, the current focus is on the increase in productivity rather than an improvement in flexibility and accuracy. The reverse is the case for ultra-precision grinding. As a result, similar ultra-machining systems for diamond turning are applicable in precision grinding. However, the ideal grinding tool has not been invented yet (10, 15).

Precision grinding as a branch of precision machining falls between Mc Keown's broad classification of Microtechnology and Nanotechnology. From Brinksmeier and Preuss' point of view, precision grinding and ultra-precision grinding are the application of micro-grinding processes for small scale material removal from large workpiece other than microstructures and micro-parts to achieve extremely tight figure and roughness tolerances (15). Miyashita in his series classified precision grinding based on the specific material removal rate and grain size (Figure 2.2). He posited precision grinding as the space between conventional grinding and polishing.

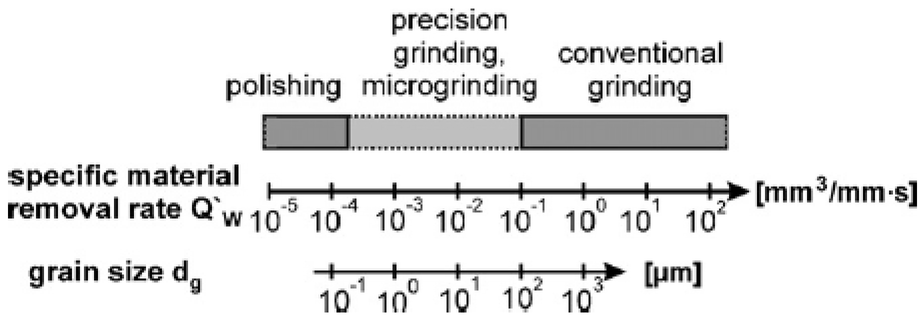

Figure 2.2: Classification of precision grinding(10)

Amongst other machining processes like turning, milling, drilling and grinding, the latter started as a precision process, achieved high precision status with the advent of super abrasives, then became an ultra-precision process with the development of rigid machine tools. Therefore, ultra-precision grinding now competes with ultra-precision diamond turning and is no longer labelled as a highly random process at the ultra-precision level(11).

Ultra-precision grinding cannot be possible without the developing technology in machining systems which improves on the areas of thermal stability, stiffness, damping and smoothness of motion which are integrated with ultra-precision metrology and isolated from the response of the machine tool during machining(13).

Schulz and Moriwaki classified an ultra-precision grinding system as one with the following movement accuracies (13, 16):

I. Slide geometric accuracy less 1µm
II. Spindle error motion accuracy less than 50nm
III. Control and feedback resolution less than 10nm

With the above achievable movement accuracies, it is expected that the ultra-precision grinding machine is capable of generating (10, 13):

I. Dimension accuracies in the micrometre range
II. Surface form accuracy of 100nm or better
III. Surface accuracy of 5nm range.
IV. Figure roughness and damage tolerances in one single machining step-deterministic. And
V. Damage free subsurface zone for avoiding light scatter in optically transparent materials.

These high-tech machining systems are available in 2-5 axes configuration and are only developed by few companies in the world including Moore nanotechnology systems, Precitech, Toyoda, Nashi Fujikoshi and Toshiba (13).

2.3.1.1: Ultra-high precision grinding

The question arises: where are we today on Taniguchi's curve? Eight years ago, Venkatesh believed that Precitech's Nanoform 200 series is the most advanced form of the precision machines in the world because it was close to delivering 1nm on Taniguchi's curve (17). The currently developed technologies involving the Nanoform 250 and 750 series and other machines and grinding spindles higher accuracies in the picometre machining range can be classified as ultra-high precision machining and would likely not remain in that category in the nearest future. Furthermore, the present day high precision grinding will most likely be regarded as normal grinding in the nearest future.

2.4: DUCTILE MODE GRINDING

According to Bifano, ductile mode grinding was first applied in the frictional wear of rock salts by King et al (18). As mentioned earlier, conventional grinding of brittle materials generate fractured surface sometimes with severe subsurface damage hence needing further polishing to derive the desired surface finish. Ductile mode machining enables the generation of nearly 100% ductile streaks while machining brittle materials thereby reducing or eliminating further polishing. The goal of ductile mode machining is to reduce brittle fracture, generate ductile streaks as much as possible hence reducing the need for numerous subsequent polishing and lapping (19).

Ductile-to-brittle transition is the phenomenon that enables the ultra-precision grinding of brittle materials to produce optically smooth surface without subsurface damage. In the absence of plastic deformation, a material is supposed to undergo brittle fracture. However on the nanoscale, brittle materials behave plastically if the potential energy increase in the volume subject to indentation is not enough to initiate cracks (15). The transition from brittle to ductile material removal is considered to be of great importance in ultra-precision grinding of optical materials (10).

2.4.1: Determinants of ductile mode grinding

Ductile mode machining of brittle materials is a complex interaction between tool geometry, process materials and material response (20). The most important deciding factors for the transition from brittle to ductile materials are the stress conditions around the cutting edge in the workpiece and the depth of cut(10).

Optical glass can be subjected to visco-plastic flow or plastic deformation if hydrostatic compression and shear stresses are sufficiently high(10). From Coulomb Mohr's hypothesis, plastic deformation is totally dependent on the strain rate, temperature, multi-axial compression and tensile stress in a workpiece, also hydrostatic compression stress fields in the shear plane are necessary for the ductile cutting of optical glass materials (10). Venkatsh and Sudin in their review on the mechanics of material cutting Shrinker et al posited that this required condition can be met in grinding by applying bonded abrasives which are capable of maintaining the required stress field. More so since each flattened, evenly protruding grain on the grinding wheel initiates an intense local stress field between the glass lamella which in overall initiates frictional heat and plastic flow of material (21). This even protrusion effect is better explained by Konig and Sinhoff's model (Figure 2.3). However, the presence of sharp grains with unevenly distributed height can initiate severe deep cracks on the workpiece.

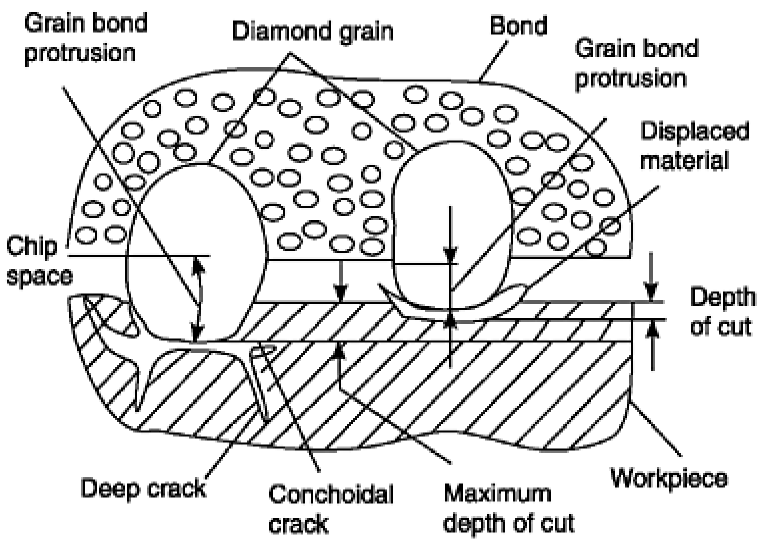

Figure 2.3: Konig and Sinhoff's model adjusted by Venkatesh(21)

The absence of brittle fracture is attainable by using a depth of cut less than the unique critical depth of cut of a particular glass. Venkatesh while analysing Zhong's modified model posited that uneven protrusion within the critical depth of cut cannot initiate brittle fracture instead plastic deformation occurs by ploughing action hence ductile streaks are produced on the surface. Otherwise, the material removal degenerates from micro-grooving and micro-ploughing to micro-crack generation due to excessive Hertzian surface pressure exerted by the abrasive grains (21) (Figure 2.4).

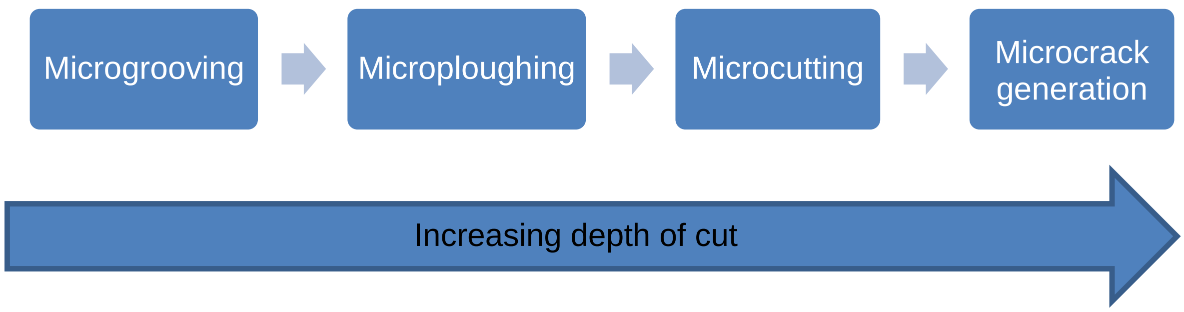

Figure 2.4: Material response to increasing depth of cut

Blackley, Scattergood, Bifano and Fawcet developed models for precision machining which relate the maximum chip thickness to the critical depth of cut (22). Below the critical depth, the converted grinding energy is insufficient for crack formation and the material is plastically deformed. Marshall et al through indentation tests showed that maintaining maximum chip thickness at a value below the critical and material specific chip thickness is necessary to avoid crack initiation and propagation. In other words, the maximum chip thickness must be maintained below the critical depth of cut all through the grinding process. From these models the maximum chip thickness (h_{max}) and critical depth of cut (d_c) depend on material and wheel properties like: young modulus (E), fracture toughness (K) and knoop hardness(H) , wheel diameter(d_s), wheel depth of cut(a_c), work speed (V_w), wheel speed (V_c) and the distance between adjacent grits (L_s) (22, 23).

The developed models for the estimation of the critical depth of cut (dc) for BK7 glass are presented below (Equations 2.1, 2.2 and 2.3) (24):

$$d_c = 0.15 \left(\frac{E}{H}\right)\left(\frac{K_c}{H}\right)2 \dots\dots\dots\dots\dots\dots\dots\dots\dots\dots 2.1$$

$$h_{max} = 2L_s \left(\frac{V_w}{V_c}\right)\sqrt{\frac{a_c}{d_s}} \dots\dots\dots\dots\dots\dots\dots\dots\dots 2.2$$

$$h_{max} < d_c \dots\dots\dots\dots\dots\dots\dots\dots\dots\dots\dots 2.3$$

According to the developed models, the critical depth of cut for different optical glasses ranges from 50nm to 1micrometer (10). Fatima et al estimated critical depth (dc) of BK7 optical glass to be approximately 45nm (24).

Gu et al from their investigative works on varying the depth of cut on Bk7 glass categorised four transition regimes for the horizontal surface grinding of optical glass as brittle mode, semi-brittle mode, partial ductile mode and ductile mode. These distinct modes are also dependent on the kinematic characteristics of horizontal surface grinding as well as grinding-induced cracks (19). In the partial ductile mode, lateral cracks and ductile streaks were observed to exist even when the maximum penetration depth is greater than the critical depth of cut. However the lateral cracks initiated by brittle fracture do not extend below the grinding surface plane, hence ductile mode grinding was achieved with the occurrence of brittle fracture (19, 23)

Brinskemier et al notably observed that ductile regime grinding is not only determined by the maximum depth of cut but also by the kinematic characteristics of the grinding process(10). This implies that a constant maximum penetration depth which is below the critical depth could result in ductile or brittle material removal depending on the ratio of feed rate to the depth of cut (10).

Chen et al through simulation of single grain grinding of Bk7 glass showed that the brittle-ductile transition of optical glass is influenced by the cutting depth of a single grain hence ductile mode grinding of glass is achieved when the cutting depth is less than the critical depth (25).

Ductile mode grinding cannot be perfectly quantified by surface characteristics of the workpiece only. Malking and Hwang et al through indentation experiments also showed that brittle mode grinding of glass resulted in two types of crack which are lateral cracking; responsible for material removal and surface formation and radial/medial cracking; responsible for strength degradation (19, 26). Pie et al through microscopy observation of brittle materials concluded that subsurface cracks exist below seemingly fracture free or ductile ground surfaces . However, the study of subsurface damage observations in ultra-high precision grinding of BK7 is beyond the scope of this research (27).

In conclusion, it is obvious that grinding of optical glass cannot be achieved without small-scale dimensions not essentially in the part of the workpiece size but in the ability developing a system with the accuracy for repeatable cutting of small and accurate dimensions which are required conditions for ductile grinding of optical glass (28).

2.5: GRINDING WHEELS

The behaviour of any grinding process is highly dependent on the performance of the grinding wheel because the wheel performance is susceptible to significant change during the grinding process (29). Grinding wheels which consist of an abrasive material held to together by a befitting bond exist in different shapes, grades, abrasive composition, bond material, structure and sizes. The nature of the abrasive process, type of workpiece, surface finish required and grinding conditions all determine the selection of a grinding wheel. The cutting action of a grinding wheel is reliant on grinding wheel features like the bonding material, the grit size, the abrasive type, wheel grade and the wheel structure. To obtain a desired optimum solution, the selection of the appropriate combination of these features is highly essential. (28)

Diamond and cubic boron nitride are the most commonly used abrasives for ultra-precision grinding of optical glass while epoxy or polyester resins and metal bond are the most commonly used bonds in precision grinding of optical glasses(30, 31). As a rule of thumb, hard bonded wheels are used for soft materials while soft bonds are used for hard materials. Generally, resin bonded wheels have been applied in grinding optical glass but resin bonds are prone to high wear rate. In a comparative analysis of the performance of resin bonds and bronze with 2µm-4µm diamond abrasives on Bk7 glass, it was observed that resin bond produced a better surface finish but wore out faster. Meanwhile, its Preston coefficient drastically reduced hence resulting in grain pull out (32). Metal bonded wheels have lower wear rate but require constant dressing, therefore, Ohmori proposed the use of ELID on metal bonded wheels to cater for the consistent need for dressing (33).

With the development in precision grinding of optical glass came the advent of super abrasives which are characterised as fine grained. Apart from being made of diamond, super abrasives fulfil the necessary grit size and height distribution requirements to facilitate ductile mode grinding. The roundness requirements for glass grinding cannot be achieved with average grain size greater than 15 µm because such exhibit variations in statistical height distribution of the abrasive grits even when perfectly dressed (15).

Brinksmeier and Shore posited that the grain size of a grinding wheel is the most important consideration for surface roughness of optical glass and, therefore, recommended that grits of less than 6µm in size should be employed in achieving a surface roughness of 1-3nm (10, 34, 35). In Chen's point of view, super smooth finishes can be achieved when the average grain size is less than 10µm (25). On the contrary, Grimme et al achieved surface roughness in the nanometre range by using coarse-grained, single-layered, electroplated diamond wheels of sizes 91µm, 151µm and 181µm, this was achieved at low specific material removal rates and proper dressing conditions (36). Hence, they concluded that it is possible to achieve nanometre range surface finishes with coarse grain diamond wheels.

Research development in the area of grinding wheels led to the birth of engineered wheels for deterministic grinding which is a huge improvement on the conventional grinding wheels. Therefore, the evolution to engineered wheels includes wear resistant coated abrasives with high bond strength, single layered metal bonding system, uniformed grain cutting edge orientations, etcetera (37).

2.6: PROBLEMS OF PRECISION GRINDING

As earlier stated, fine-grain diamond wheels achieve the best result but grinding with super-abrasives has its inherent challenges. Firstly, resin bonded grinding wheels are prone to high wear. Hence, the wheels must be reconditioned frequently to maintain roundness. When the wheels are reconditioned, it results in shrinking diameter and a change in the depth of cut. The cutting depth changes in an unpredictable way initiating new problems like figure error. However, refusal to recondition the wheels result in the loss of wheel roundness and creates a difficulty in maintaining ductile mode grinding (15).

Another challenge encountered with the use of small grit sizes is the tendency of wheel loading to occur. Wheel loading reduces grinding efficiency and could even make grinding impossible. The available chip storage space drastically reduces with a decrease in grits size because they have few voids. Hence, wheel loading occurs as the material removal rate exceeds the available chip storage space (31, 38). Chips tend to be lodged in the pores between active grits on the surface of the wheel. This prolonged effect reduces the level of grit protrusion and the available space for the storing of new chips hence initiating dull rubbing action between the wheel and the workpiece causing poor surface quality and severe subsurface damage on the workpiece (31).

The extreme hardness of metal bonded super-abrasive wheels makes its truing and dressing very difficult with problems. While using diamond tools, mechanical truing and dressing have the following limitations: A newly dressed wheel surface becomes too smooth and dense therefore reducing the chip storage space (38, 39), and generates high truing/dressing forces, high tool wear and maximum grit protrusion equalling 20%-30% of the grit size which affects the performance of the wheel (40).

Furthermore, the difficulty in grinding wheel manufacture results in grain agglomerations(8), changes of the abrasive layer topography and configuration during the grinding process and difficulty in the development of a process planning system since grinding is very sensitive to the product properties and requirements(41). Other problems include the occurrence of chatter vibration and grinding burn.

In conclusion, the advancement of diamond turning has not yet attained its final stage as the present concern is more on the improvement in productivity rather than increase in flexibility and accuracy. The reverse is the case for ultra-precision grinding where accuracy and flexibility is a major concern. Though similar machining equipment is used for precision grinding and diamond turning, the ultimate grinding tool has not been invented yet (10, 15). Furthermore, Fung and Tong stressed the need for engineers to imbibe scientific skills in order to tackle the prevalent challenges facing them (42). Some of the problems encountered in ultra-precision grinding today cannot be fully solved without an understanding of the grinding process at the sub-atomic level. Therefore, it is high time for precision engineers to add quantum mechanics to their tool box to be able to study and understand grinding at the subatomic level.

2.7: SINGLE POINT INCLINED AXES GRINDING

SPIA is one of the several grinding configurations for specific applications amongst other configurations like centerless grinding, internal surface grinding and arc envelope grinding. SPIA which is similar to arc envelope grinding or inclined axes grinding is normally applied in the manufacture of meso and micro optical elements in the form of aspheric surfaces(43). However, the arc envelope grinding uses an arc wheel while SPIA utilises the cube point contact of a wheel. As illustrated in Figure 2.4, point A1 on the grinding wheel makes contact with P1 on the workpiece while A2 contacts with P2 for arc envelope grinding but the same tip point A1 contacts the grinding surface at P1 and P2. This is enabled by rotating the grinding wheel on the B axes at α_1 and alpha α_2.

Asides overcoming the limitations encountered with the arc envelope grinding, the SPIA configuration helps to avoid interference while grinding small aspheric inserts. In SPIA configuration, the velocity of the workpiece is parallel to the velocity of the grinding wheel hence a possible improvement in the surface roughness. Chen et al observed that surface roughness improves when the velocity of grinding wheel is parallel to the velocity of the workpiece. Hence, SPIA helps to achieve a better surface roughness (44). More advantages of the SPIA configuration over arc envelope configuration are listed highlighted in Table 2.1.

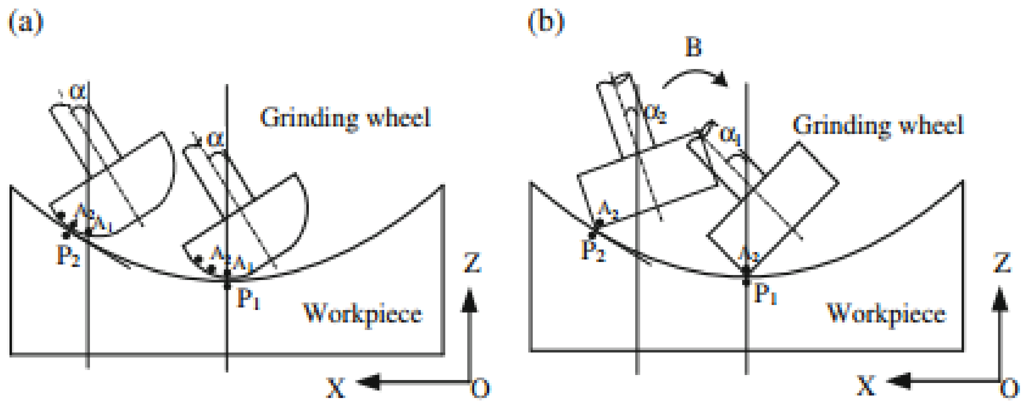

Figure 2.4: Single point inclined axes grinding and conventional arc grinding(43)

The adaptation of SPIA to the horizontal surface grinding of flat optical lenses will help to overcome some problems of precision grinding listed in section 2.6 as it helps avoid wheel rubbing and glazing that may occur due to chip formation being interlocked in the grits. This is also an avenue for the reduction of the thermal wear and flexibility. However while adapting this method to horizontal surface grinding for a flat surface, there will be no need to rotate alpha during the grinding process instead the spindle is rotated on the B-axis (Figure 2.4 and 2.5).

Table 2.1: Comparison of SPIA with inclined axes grinding

Grinding Mode	Inclined axes mode	SPIA
Grinding wheel	Arc shape	Cube corner
Wheel radius	Greater than 0.1mm	Can 0.005mm
Control centre	Centre of grinding wheel	Grinding tip
Positioning controlling	Difficult	Easy
Inclination angle between workpiece and wheel spindle	45^0 in YOZ plane	Variable
Controlling axis	X-Z axes	X-Z-B axes
Trueing	Difficult	Easy

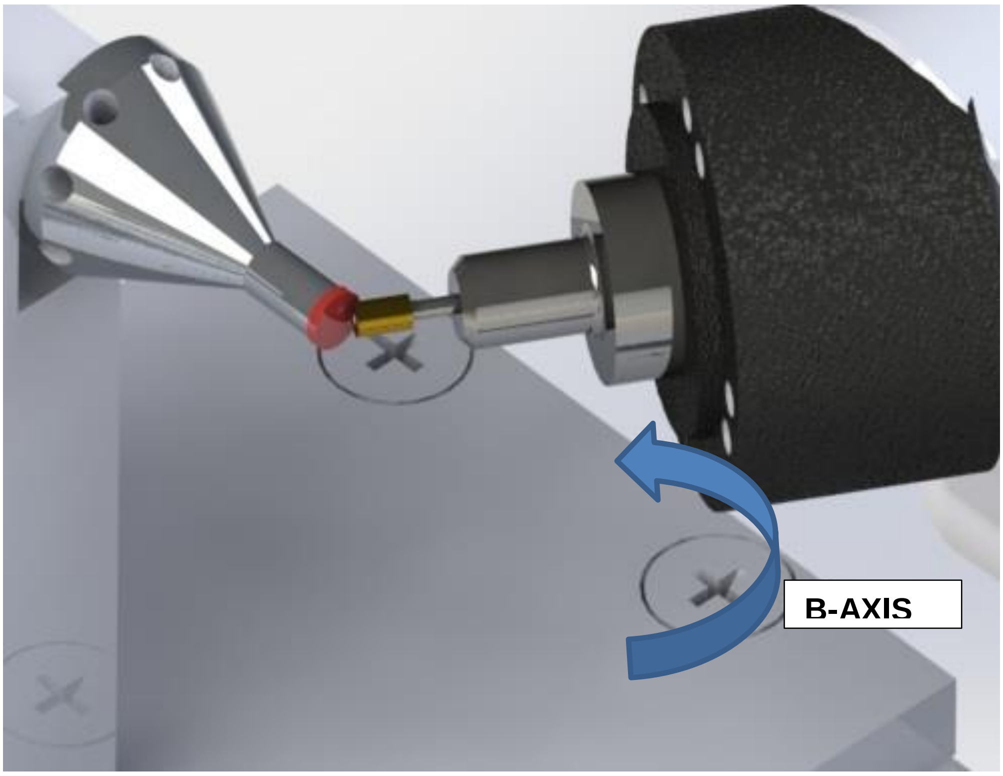

Figure 2.5: Single point inclined axis grinding configuration

2.8: SURFACE INTEGRITY

The surface Integrity of a machined workpiece is one of the greatest factors used in measuring the efficiency of the abrasive process applied in the manufacture of the workpiece (10). It affects the material properties of a workpiece and the preservation of surface integrity is a manufacturing consideration (45). Particularly for precision grinding of optical parts which has a wide area of application, the important considerations of surface integrity cannot be over emphasized. Michael Field and John. F. Kahles defined surface integrity as the condition of a workpiece after modification by a manufacturing process (46). Surface integrity can be viewed from two aspects:

I. Topography characteristics: The first part is made up of surface roughness, waviness, errors of form and flaws
II. Surface layer characteristics: Comprises plastic deformation, hardness and residual stress (45).

In the long run, the surface integrity of a workpiece will be damaged if improper parameters are used such as dull tools, excessively high speed, inadequate grinding wheel hardness, improper coolant or lubrication. Generally surface integrity is affected by the following variables:

I. Grinding wheel selection
II. The workpiece properties
III. Wheel dressing and truing
IV. The environment
V. Process variables and condition of the machine
VI. Grinding parameters

The above variables can affect the surface integrity of an optical glass by producing high temperatures during grinding and chemical reaction between the tool and the workpiece (45).

Since the integrity of a surface affects its suitability for specific functional applications, the relationship between a grinding process and the resulting surface integrity should be perfectly understood. The interaction of the cutting edges of the wheel and the microstructure of the workpiece should be properly analyzed in relation to the final surface finish. The most commonly measured or the most important surface integrity parameter is the surface roughness value.

2.8.1: Surface roughness

This is a measure of inherent, fine closely-spaced surface irregularities created by the production process. It is usually regarded as surface finish in engineering and is normally expressed in its root mean square value or average surface roughness.

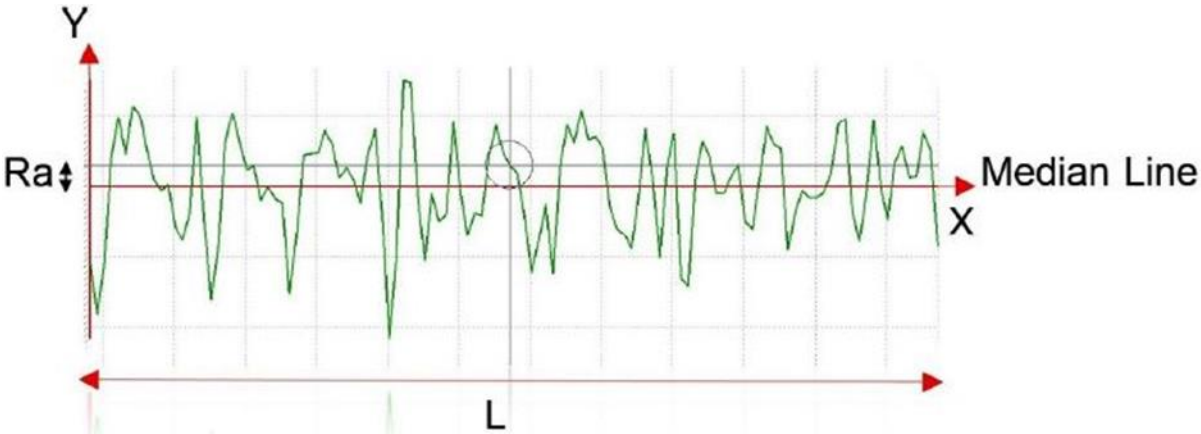

Figure 2.6: Surface roughness profile

Several surface roughness measurements exist (Table 2.2) but the average surface roughness is the most commonly measured. From Figure 2.6, the average surface roughness (Ra) can be expressed mathematically as:

$$Ra = \frac{1}{L}\int_0^L |f(x)|dx \ldots\ldots\ldots\ldots\ldots\ldots\ldots\ldots\ldots\ldots\ldots\ldots\ldots\ldots\ldots\ldots 2.4$$

Table 2.2: Surface roughness parameters

Parameter	Definition
Ra	Average of the measured peaks and valleys
Rq	Root mean square of the measured peaks and valleys
Rti	Peak to valley value of roughness profile.
Ry	Largest value of *Rti* over the sampling length
Rtm	Mean value of all *Rti* values within a sampling length (L)
Rv	Maximum depth of a surface profile from the centre line
Rp	Maximum height of a surface profile from the centre line
Rpm	Mean value of Rp

Gu et al analysed the dependence of Bk7 surface roughness on grinding parameters and they posited that wheel speed and feed rate have strong effects on surface roughness because increasing feed yields a poor surface quality while high wheel rotation is relevant for good surface finishes (19).

Zhao et al analysed the dependence of surface roughness on grinding parameters and they posited that wheel speed and feed rate have strong effects on surface roughness and they went further to establish a predictive model relationship between surface roughness and subsurface damage. This relationship is dependent on the half apex angle of abrasive grain and the magnitude of extra grain extrusion (37).

2.8.2: Measurement of surface Integrity

Several techniques have been employed in the past to measure the surface roughness of machined surfaces. These techniques range from the subjective judgment based on visual inspection and fingernail tests to the objective measurement which comprises: capacitance, pneumatic, ultrasound and inductance methods. Other methods include noncontact with the use of optical profilers, optical microscopy, scanning tunnelling microscopy (STM) and much lately atomic force microscopy (AFM). Asides the non-contact methods, contact mechanical stylus instruments are also used for surface roughness measurements (47).

Surface finish is usually measured using the contact and the non-contact methods. Contact methods employ the use of profilers by dragging a stylus across a surface while non-contact methods employ the use of electron microscopy, photogrammetry, interferometry and electrical capacitance. The most popular method for measuring surface characteristics of a workpiece is the use of a stylus-based measuring instrument also known as a profiler (48). As a result of the inadequacies encountered in analysing surfaces in 2D, emphasis has been laid on 3D analysis, hence scanning techniques have been implemented to accomplish 3D assessment (48). Thus essential features of a surface characterization system employ 2D projections of a 3D data in the form of an axonometric plot and a contour map.

3D data characterization can be accomplished with the use of both visual and numerical techniques. Numerical characterization consists of area parameters like area mean height, the average roughness of area (Ra), root mean square roughness (Ra) of area and volume parameters, skewness of area about the mean, kurtosis of the area about the mean, distance from mean to the highest peak and distance from mean to lowest valley. Volume parameters include material volume, void volume and debris volume, also graphical characterization will include axonometric plotting and contour plotting (48).

2.9: PROCESS MONITORING IN GRINDING

The grinding process is typically a non-stationary process which is characterized by a high number of cutting edges simultaneously undergoing non-uniform wear (10). Therefore effective monitoring of the grinding process is necessary to demystify the difficulties encountered. Ichiro Inasaki and Wang in their respective classical texts highlighted the important goals of grinding process monitoring as (29, 49):

I. Detecting major grinding problems in the form of chatter vibration, grinding burn and surface deterioration.
II. Information obtained by the monitoring system on the process parameter should be useful for the optimization of the grinding process.
III. The input-output casualties of the grinding process should be useful for creating a databank as part of an intelligent monitoring system.

Since ultra-precision grinding of optical glass takes place at the submicron to nano-scale dimensions and the ultra-precision machining process and surface finish are more closely affected by the ductile/brittle transition properties of brittle materials, It is seen as a herculean task to obtain essential process signal features which are difficult to obtain at the submicron and nanoscale. Depending on the monitoring targets which are: surface roughness, grinding wheel wear, wheel and bond performance, grinding burn and etcetera, monitoring techniques could be applied online, in-situ or in-process monitoring.

From a systems approach to grinding, the monitoring targets for grinding is dependent on the system behaviour and grinding environment which affect the output (Figure 2.7). It is of extreme importance to make these targets predictable. Hence grinding process modeling is not feasible without effective monitoring and understanding of the grinding process (50).

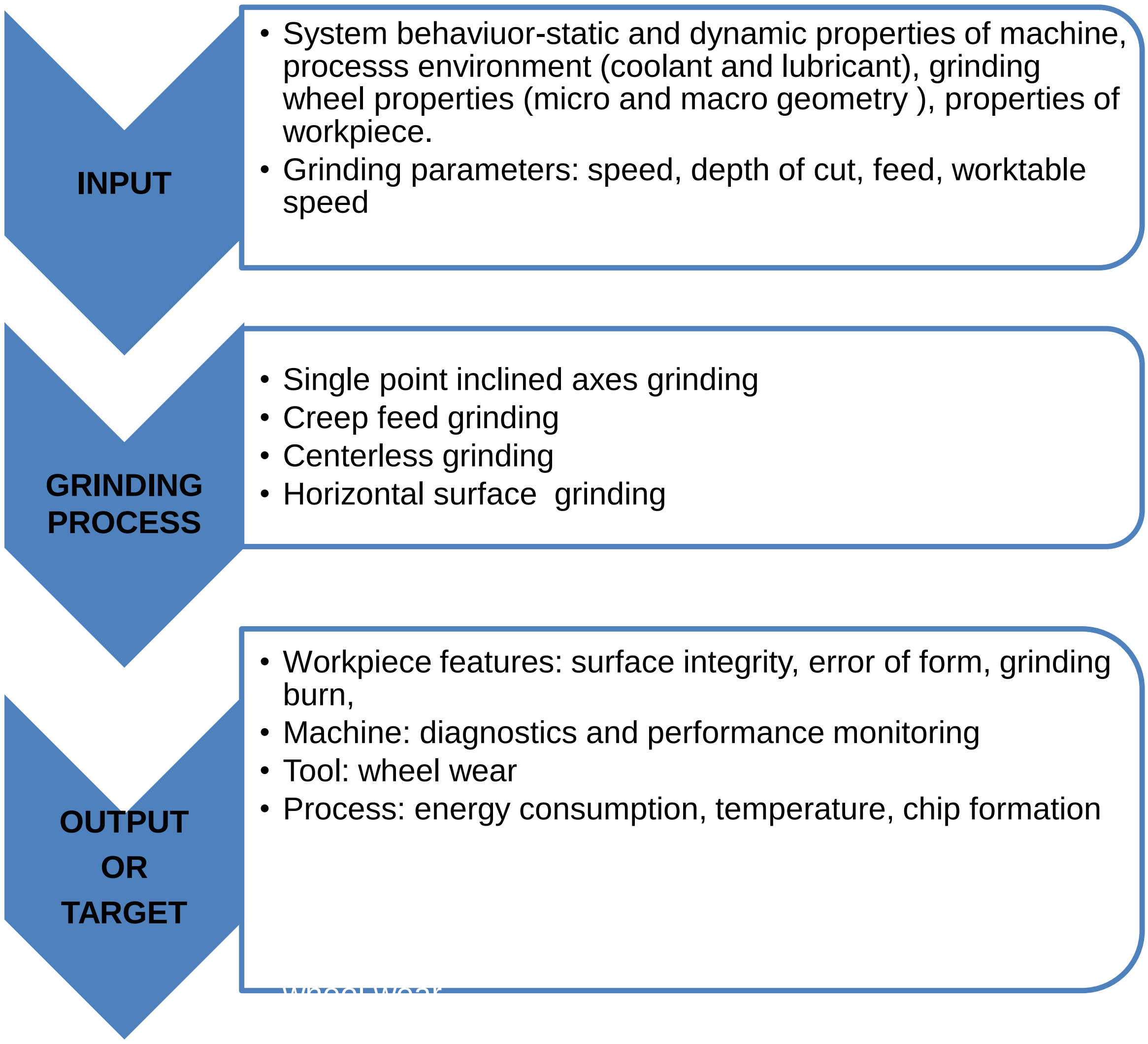

Figure 2.7: System overview of grinding process monitoring

2.9.1: Data Acquisition and sensor development

The process monitoring flow emanates from a data acquisition process, through signal processing and interpretation (Figure 2.8). When executing a process monitoring system, an important factor to consider is to select which signals are most suitable to achieving the end result. Grinding process monitoring techniques imbibe the use of grinding force, power, vibration, ultrasonic and acoustic emission sensing. The latter has developed to be one of the most promising sensing techniques.

An understanding of the instantaneous AE characteristics in the transition of wheel/workpiece contact is necessary for contact selection and process control (51). It is an objective to measure process quantities of interest as direct and as close to their origin as possible. The grinding process, in general, has a large number of input quantities which dominate on the process quantities. Once there is an interaction between grinding wheel and workpiece, process quantities exist. An effective measurement of these quantities is a step to efficient characterizing of the grinding process(29).

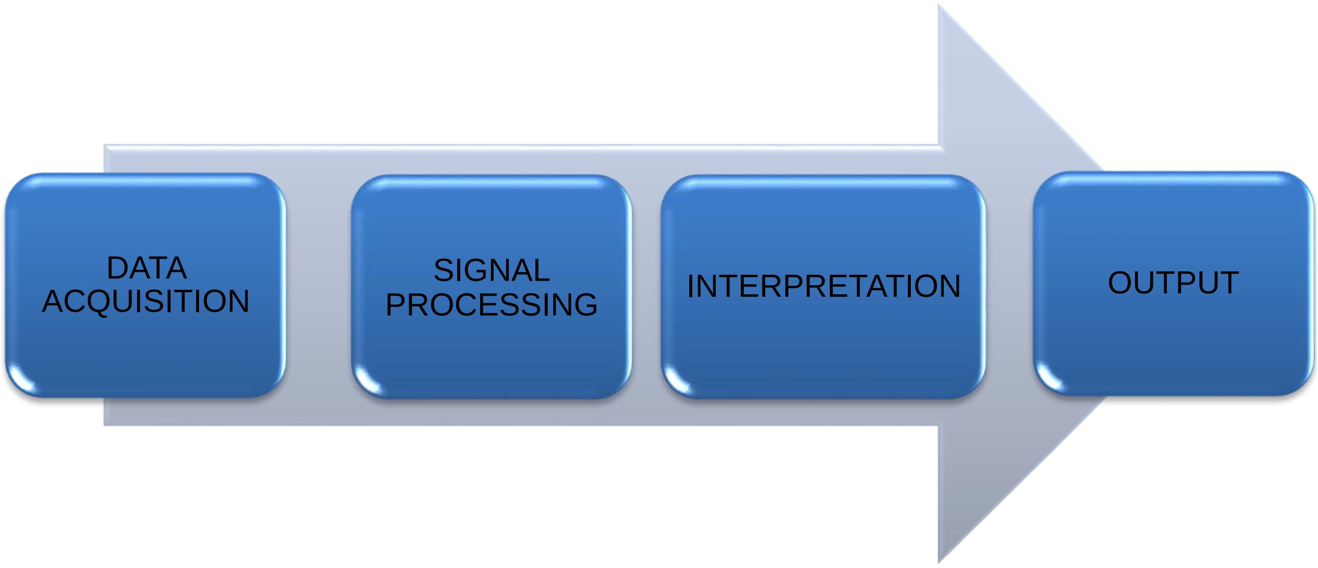

Figure 2.8: Process monitoring flow

Acute sensor information in UPG is required for assessment of the process as regards to material removal at the submicron level, surface finish and subsurface damage and the importance of the sensor feedback information cannot be overemphasised. The integration of sensors as an integral part of in-process monitoring in ultra-precision machining requires a high level of engineering confidence in the ability of the sensor to consistently detect the requisite process conditions (52). Also, for control purposes as regards the variation in process parameters such as tool condition, material removal rate (MRR) and process cycle related characteristics like contact or spark out in grinding (52).

Sensors available for monitoring in-process machining include force and power, vibration. At the submicron level, conventional sensors like force and vibration sensors are prone to inaccurate measurement due to the lack of sensitivity in the exceptionally high frequency range where most micro cutting activities are sensed. But AE sensors are among the few which have demonstrated high signal to noise ratio at the precision level of grinding. Furthermore, AE sensors demonstrate good response at high frequencies where other low-frequency disturbance are diminished and the frequencies from sub-micrometer level precision activities become dominant (Figure 2.9)(52).

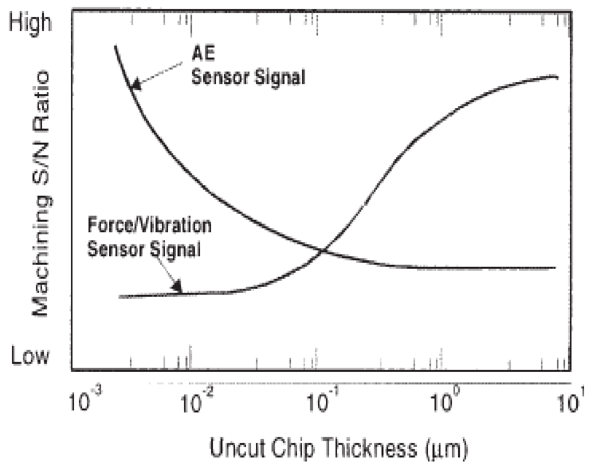

Figure 2.9: AE Signal/Noise ratio (52)

To meet up with the recent development in precision machining, demands are continuously placed on improving sensor based in-process monitoring systems. These sensors are used to generate control signals which are used to enhance both the control and productivity of precision grinding systems aimed at being cost effective during mass production (52). Sensor fusions techniques have also proved to be highly valuable in monitoring precision grinding processes.

Over the years, indirect measuring signals like grinding power, forces, vibration, the surface temperature of the workpiece and acoustic emission have been used for monitoring of the grinding process. These signals are usually related to an output parameter of the grinding system. In most cases where the objective monitoring cannot be efficiently measured directly, indirect methods which measure quantities that directly change with the process condition are adapted. These indirect signals are usually referred to as in-situ or in-process measurements. Amongst them, acoustic emission measurement technique has proved to be one of the most sensitive over the years.

The influence of advanced signal processing techniques and artificial intelligence was observed in the development and application of intelligent sensors and sensing systems and serves as a foundation for input to learning schemes (52).

2.10: AE SENSING TECHNIQUE

Acoustic Emission sensing technique became a popular term for scientific research in the second half of the 20th century. AE signals are known to possess high-frequency bandwidth ranging from infrasound to ultrasound frequency of 10Hz to 50MHz with low amplitude. AE is a physical phenomenon which entails the formation of transient elastic waves within or on the surface of a parent physical centre and is generated by atomic level disturbances (53). Under the influence of localized dynamic modification in the structure of a material, elastic waves are generated and spread out from the source of the change. The elastic waves propagate through the structure of the material where its energy is primarily used for local mechanical work and generation of heat (54). An integral part of this energy radiates towards the edge of the structure, on exiting they are captured by a sensing device as AE.

Glass has low acoustic impedance compared to materials like wood and plastic, hence, it exhibits suitability AE process monitoring. A typical AE sensing system employs the output of a sensor fed through the amplifier with high input impedance and low output impedance.

2.10.1: AE Sensors

Piezoelectric sensors are particularly suitable for AE sensing in machining process monitoring (55). With an efficient data acquisition system and effective signal processing, AE sensors can detect most of the phenomena in machining owing to its very broad and dynamic sensor bandwidth from 100 to 900 KHz (55).

Capacitance AE detection has high sensitivity and can also be used to calibrate other AE sensors but are susceptible to severe environmental conditions (55). Other developing AE sensor technology research areas include depositing thin film piezoelectric sensors on a zinc oxide shim to improve signal quality and minimize geometric propagation loss. Non-contact fibre optic interferometers are also being developed to transmit signals from source to sensor (55).

Another important consideration is the transmission of AE signals from the sensor unit to the data acquisition system, the use of coupling fluids and development of RF and wireless AE transmission and the sensor unit. Furthermore Teti et al attributed the development of a non-intrusive coupling fluid to enhance sensor coupling on the spindle drive to Hutton and Li (55).

2.10.2: Uniqueness of AE sensing technique in precision monitoring

AE signal monitoring is one of the most reliable process monitoring and quality control techniques in manufacturing (53). Although previously observed in the cracking of wood and other structures, modern approach emerged in the 1930"s but the phenomenon was not defined until the 1950s with the works of Kaiser and B.H Schofield (56). Originally applied to the destructive testing of structures, its use has experienced a tremendous growth for manufacturing processes since its discovery in the early 1950s in Germany to its first process monitoring application in 1970 (57).

The incorporation of an in-process sensor requires a high level of engineering confidence in the ability of the sensor to detect the desired process characteristic and reliably detect the quantity being measured (52). In the absence of this confidence, application of in-process sensor technology in monitoring ultra-high precision grinding process is not justifiable. Acoustic Emission signals are suitable for very fast events hence its sensitivity is suitable for ultra-precision grinding process monitoring (31). Since sensor feedback information is critical for higher yields and process throughput, an applicable sensor to UHPG should have the necessary qualities to account for process conditions at sub-micrometre to nanoscale dimensions. At a very high level of precision, AE sensors have the capability for this range of applications compared to displacement force sensors which are better adaptable to conventional machining (Figure 2.10) (52).

Another uniqueness of AE sensing technique is that its frequency of propagation is from 100KHz to 1MHz which is well above most structural natural frequencies, hence its immunity to the influence of machine vibration.

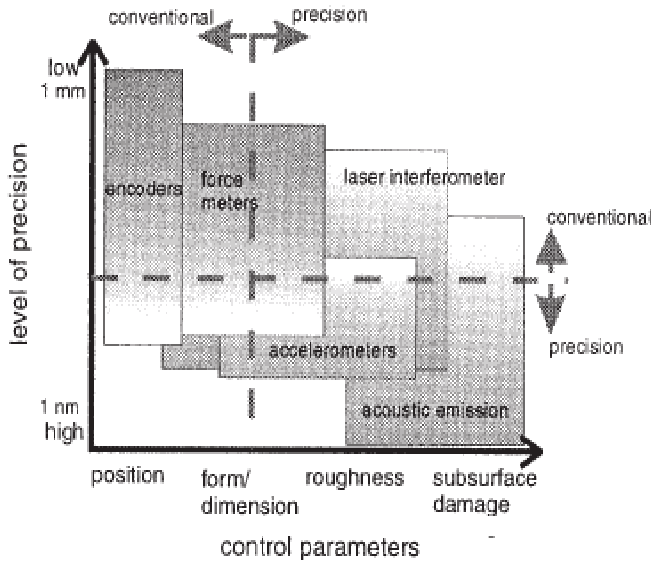

Figure 2.10: Sensor application versus level of precision (52)

2.10.3: Types of AE signals

Theoretically, each grit from the grinding wheel generates a transient or burst AE signal. When numerous grits cut through the work piece almost simultaneously in such a way that the interval of consecutive cuts is shorter than the decay time of each burst, continuous AE signals are generated (51). Also for the initial spark in and spark out stages in a conventional setting, AE is seen as burst signals, sometimes this is because the cutting edges of the grits are not at the same circumferential height (51).

AE_{rms} in its sense its equivalent to a statistical average and is similar to a low pass filtered signal. As a result, its application to unique cases like detection of high-frequency chatter, massive breakage of bonds, initial contact of grits with the workpiece, grinding crack and burns is limited compared to raw AE signals because changes in the process condition would have occurred before any appreciable change in the AE_{rms} signal (51). The limitations of AE monitoring technique include signal saturation and the random oscillation of the RMS level (23).

2.10.4: AE signal processing

Reliable process condition monitoring cannot be based on a single signal feature, therefore, it is necessary to extract pertinent features that best reflect the process conditions (55, 58, 59). This can be achieved through sufficient signal pre-processing and further processing. Pre-processing occurs in the form of filtering, amplification, RMS conversion, A/D conversion, segmentation and some of these signal processing applications come as an integrated part of the sensor (55).

Further signal processing involves transforming raw AE signals into the time and frequency domain and extracting important features. Since not all the features are relevant, the important ones are extracted to diagnose the process conditions. Feature extraction and selection are important considerations for advanced signal processing of AE sensor based process condition monitoring.

Feature extraction is the process of transforming the original sensory signal into potentially discriminant features (60). It is usually enabled by applying different techniques like power spectral density, discrete wavelet decomposition, Fourier transform, Gabor transform, and wavelet decomposition. These techniques can be viewed broadly as relating to the time series domain and frequency domain.

Some important time domain features include:

I. Skewness: the degree to which a statistical distribution is lopsided around the mean. A zero value indicates a perfectly symmetrical statistical distribution. The distribution with outliers above the mean has positive skew while outliers below the mean have negative skew values.

II. Kurtosis: the sharpness of the peak of the frequency distribution. It is also the measure of the ‘tailedness’ of a probability distribution of a real-valued random variable. A positive kurtosis indicates a ‘peaked’ distribution and a negative kurtosis indicates a ‘flat’ distribution

III. Crest factor: the ratio of the peak value to the RMS of a waveform.

IV. Some other time domain features include: peak coefficient, AE ring down count rate, RMS value, peak factor, mean and standard deviation.

Furthermore, autoregressive modelling and wavelet decomposition are methods for extracting features from processed AE signals. ARM essentially involves building a regression model of autocorrelated errors existing in the AE signals while wavelet decomposition involves breaking down a signal into desired levels.

Feature selection is processing and deriving an optimal subset from the extracted features based on an evaluation criterion(60). It entails eliminating redundant and irrelevant features thereby facilitating a reduction in feature dimensions and increase in classification accuracy. Feature selection is not a widely researched area however Lezanski notably classified feature evaluation methods under three broad categories (61):

I. Filter approach: The developed algorithm assesses and selects features based on the overall data characteristics without involving any learning model.
II. Wrapper approach: A learning model is employed and its performance is used as the evaluation criterion. This approach is more accurate but costs higher computationally and has a lower speed.
III. Hybrid approach: Balances the accuracy of the wrapper approach and the speed of the filter approach by applying the wrapper approach exclusively to the set of features selected by the filter approach first.

Also, Zhang while monitoring the online prediction of optics developed a support vector regression model from the famous Vapnik model which was used in classifying and selecting acoustic, vibration and force signals (62). Other feature selection and classification techniques include genetic algorithms like ant colony optimization and particle swarm optimization.

2.10.5: Some research works on AE in grinding monitoring

AE has found widespread application in grinding control and monitoring of grinding processes. Webster et al were able to achieve surface quality control by studying the relationship between material removal rate AE with grinding force (63). Wang et al applied AE in the detection of grinding wheel wear (64). Stephenson et al compared the performance of resin bond diamond wheels and cast iron bond on zerodur and Bk7 workpiece. They discovered that: for fine grit wheels, aggressive dressing parameters correspond with low amplitude AE levels, wheel/workpiece contact area influenced AE during for resin bond wheel (31). Han and Wu applied AE to the precision grinding of composite ceramics to determine the relationship between AE, precision grinding techniques and grinding direction. They concluded that correlation may exist between surface roughness and AErms (65).

2.11: ARTIFICIAL NEURAL NETWORKS

ANN is a mathematical model simulation inspired by biological nervous systems through the imitation of human brain's problem-solving approach. The concept uses real and processed data to develop model systems used for classification, decision making and forecasting. The performance of a neural network is determined by its network structure and connection weights between neurons where a neuron receives input signals externally and transforms them into a single value.

The neural network is made of the input layer, hidden layer(s) and an output layer with weights (w) and several existing connections between the layers (Figure 2.11). The process of introducing additional hidden layers into a network creates a difficulty in training due to the fact that training a large network is more complex and time-consuming (66).

The learning process is the means through which the neural network acquires knowledge by matching patterns in data for adequate classification. As a result, new data is predicted based on the acquired knowledge. Based on the mode of parameter change in the knowledge acquisition, neural network learning process is classified as supervised and unsupervised learning.

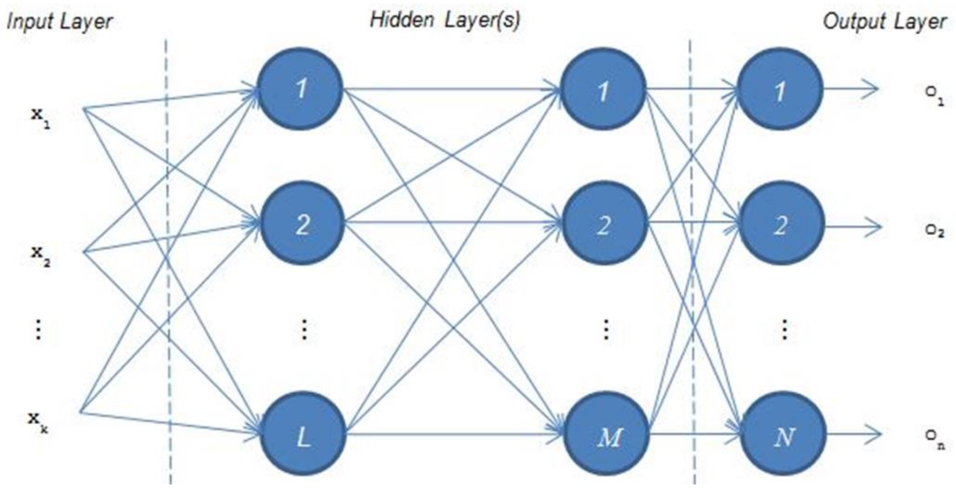

Figure 2.11: Single hidden layer Neural Network structure (67)

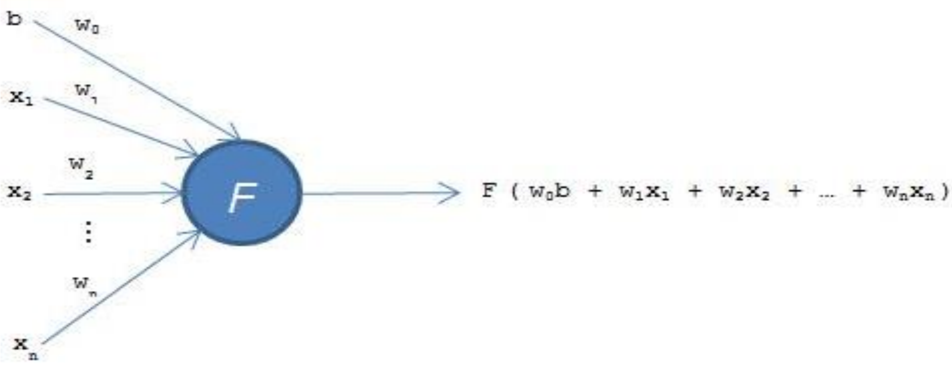

Figure 2.12: Single neuron activation (67)

The back propagation neural networks BPNN which is frequently used is a modified neural network with highly interconnected neurons organised in a layered structure. It is a logically applied in-training multi-layered neural network and its major advantage is in the non-linear solutions to ill-defined problems (68). The standard mode for training BPNN is using a gradient descent algorithm in which each layer is connected through associated weights (w) and the weights are moved along the negative of the gradient of the performance function (Figure 2.12). BPNN is performed using three steps:

I. Develop the network structure and initialize the network
II. Feed the training data repeatedly to train the network
III. Predict with the trained network using sample data

BPNN training process employs a technique of adjusting the assigned weights by comparing the output and the expected target to ensure the output is accurate. This can either be achieved with the batch training or stochastic training.

I. Batch training: The weights are updated once every round because weight updating process is determined by the error of the entire package of training patterns.
II. Stochastic training: The weights are updated for each pattern in one round because the weight updating process is based on the error of a single training pattern.

There are certain considerations for the selection of activation function for ANN (69). A network may be assigned different activation functions for different nodes in the same or different layers. However, most networks use the same activation function predominantly for the node in the same layer.

Application of neural network to detect grinding anomalies includes the use of fast-training radial basis function architecture to detect grinding burns in grinding of steel after feature selection from acquired AE signals based on autoregressive parameters and average statistical properties (64). Kwak et al applied a neural network to detect chatter vibration in grinding using a combination of power and AE signals. They achieved 95% successful diagnosis at a learning rate of 0.6 and with 2 hidden layers (70).

In the optimal process control of creep feed grinding, grinding force signals were modelled to by introducing error distribution function to an improved BPNN algorithm which proved to be a better modelling strategy. The learning algorithm was able to reduce the local maximum to effectively obtain the global maximum and also accelerate the convergence speed of the learning process effectively (71).

Pawel Lezanski concluded that a neuro-fuzzy combination yielded better result compared to fuzzy logic for grinding wheel condition monitoring. However, he also observed that the performance of such systems can be lower than neural network based systems and their potential for knowledge extraction can be limited (61).

2.12: CONCLUSION

With the concise understanding of the several conditions necessary for ductile mode machining of optical glass and acoustic emission process monitoring techniques, it is necessary to carefully design experimental conditions involving the right selection and combination of machining parameters.

CHAPTER THREE
EXPERIMENTAL DESIGN

3.1: INTRODUCTION

This chapter represents the experimental design setup and methods applied in the course of the study. The chapter comprises the ultra-high precision machining systems utilized in the research, choice of grinding wheel, workpiece, acoustic emission sensing equipment, machining process and configuration utilized. It also includes the Box-Behnken design of experiment and parameter selection for the research. Design expert software and Minitab were utilized in the experimental design while LabVIEW was applied to design the AE data acquisition codes.

3.2: ULTRA-HIGH PRECISION MACHINE

The research experimental tests were carried out on a revolutionary, flood coolant compatible 4 axes Nanoform ultra-grind 250 machine manufactured by Precitech (Figure 3.1). This ultra-precision freeform machine is designed for diamond turning, deterministic freeform milling and grinding for the most challenging applications including glass grinding for plane and aspheric lenses, mould inserts for lenses and glass pressing. The Nanoform 250 ultragrind is standardized with Precitech's UPx CNC machine control that provides a user-friendly interface with features designed specifically for increased throughput. It is also equipped with an unprecedented 16 picometer feedback resolution and a high-tech operating system with 0.01 nanometre programming resolution. The sealed natural granite base provides exceptionally long term stability and immunity to external vibration. The Nanoform 250 ultragrind incorporates an FEA optimized dual frame for the ultimate in environmental isolation. The linear motors are driven by true linear amplifiers. The hydrostatic oil bearing sideways with optimized stiffness and damping characteristics are customized by Precitech and the liquid cooled slides enable thermal stability. It can be configured for precision grinding (2 or 3 axes) using a 15,000 rpm spindle in the 45° or 90° orientation for cross-axis grinding in the direct machining of precision glass optics and freeform grinding and (3 or 4-axes) using a 50,000 rpm spindle and a rotary B-axis for parallel grinding or 45° grinding.

Figure 3.1: Nanoform ultragrind 250 lathe machine at the Precision Engineering Laboratory, Nelson Mandela Metropolitan University

3.3: ULTRA-HIGH PRECISION GRINDING SPINDLE

The research utilized a 50,000rpm motorized air bearing spindle manufactured by precitech grinder systems which is one of the latest ultra-high precision grinding technologies with axial and radial error motion which is less than 25nm at full capacity of 50000 rpm (Figure 3.2). The spindle accuracy is capable of eliminating synchronous and asynchronous spindle error which could have an effect on the workpiece surface pattern.

The spindle was maintained at an optimum operating temperature of 23 degrees Celsius using thermoflex 1400 chiller with a dowtherm SR1 heat transfer fluid (Figure 3.3). The heat transfer fluid comprises 95.5% weight of ethylene glycol solution in water and is capable of providing freeze protection below -50°C (-60°F) and burst protection below -73°C (-100°F). The spindle was also operated from a designated controller supplied by the spindle manufacturer.

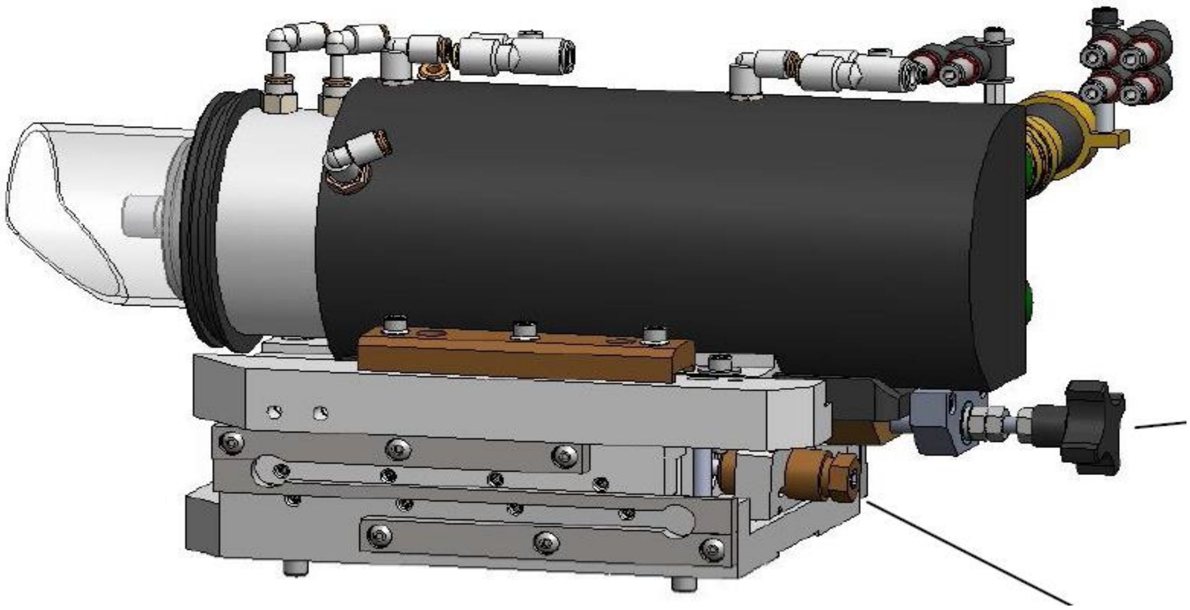

Figure 3.2: Precitech 50000 rpm ultra-high precision spindle

Figure 3.3: Thermoflex 1400 spindle chiller

3.4: GRINDING WHEEL

Resin bond diamond grinding wheel manufactured by Braemer with a grit size of #1200 was used for the experiment. The wheel was mounted on a shaft with an overall length and shank of 3.0 and 0.25 inch respectively (Figure 3.4 and Table 3.1).

The wheels were already dressed by the manufacturer. It was observed under the microscope and a perfect cube between the end and the cylindrical face of the wheel was noticed. This is the desired condition for SPIA hence no further dressing was required at this stage. The average grain size of the wheel is less than 10μm which corresponds to Miyashita's classification range for grinding of brittle materials (10).

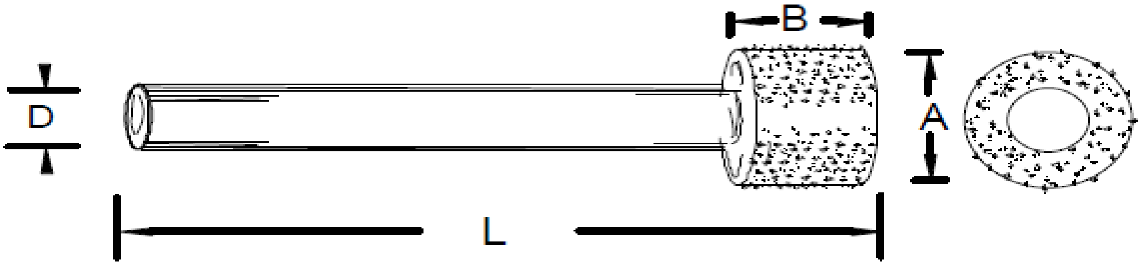

Figure 3.4: Resin bond diamond grinding wheel dimensions

Table 3.1: Resin bond diamond wheel dimensions in inches

Wheel diameter(A)	Wheel width (B)	Shank (D)	Overall length (L)
0.625	0.500	0.250	3.000

3.5: GRINDING FLUID

Water soluble grinding fluids are the best for precision grinding (40). Challenge 300HT was used with suitable unique properties. It is a synthetic fluid capable of optimizing material removal rate and surface finish in grinding operations. Its exceptional heat transfer characteristics ensure the preservation of diamond wheel life and it does not foam during the grinding operation.

3.6: WORKPIECE

Single point inclined axes grinding was carried out on 25mm diameter and 2mm thick uncoated BK7 window manufactured by UQG optics. The properties of the window are listed in Table 3.2.

Table 3.2: Some mechanical properties of Bk7 glass

Knoop hardness	610
Young modulus	82Gpa
Fracture toughness	0.85
Acoustic impedance	Low
Abbe number	64.2
Refractive index	1.157
Thermal expansion	$7.1\text{x } 10^{-6}K^{-1}$
Thermal conductivity	$1.114Wm^{-1}K^{-1}$

3.7: ACOUSTIC EMISSION SENSING UNIT

The AE sensing unit consists of the 8152B piezoelectric sensor which is capable of detecting continuous and burst AE signals within a wide frequency range (Figure3.6a). The AE sensor was calibrated on a Kistler calibration test bench accordingly with the compatible 5125B coupler (Figure 3.6b) and has a high sensitivity value of 57 dB ref 1v/ (m/s) to the surface and longitudinal waves. The sensor and coupler unit are powered by an S-100-24 supply (Figure 3.6c) manufactured by Meanwell. The input of the power supply was set at 220V with the output voltage stepped down to 24V with reference to ground.

The sensor-coupler connection is capable of amplification and filtration and RMS conversion of the acquired AE signals through inbuilt configurable gain of x10 and x100 for 20dB and 40dB amplification, high pass filter range of 50kHz to 700kHz, low pass filter range of 100kHz to 1MHz and RMS conversion range of 0.12ms to 120ms time constant (Figure 3.5). The analogue output voltage signals are connected to a 16bit PIC data acquisition card via BNC 2110 board (Figure3.6d).

The actual data acquisition was realised using a virtual instrumentation Graphical User Interphase (GUI) software which includes a front panel for viewing the AE signal output in real time and a block diagram section for developing the G-code programming.

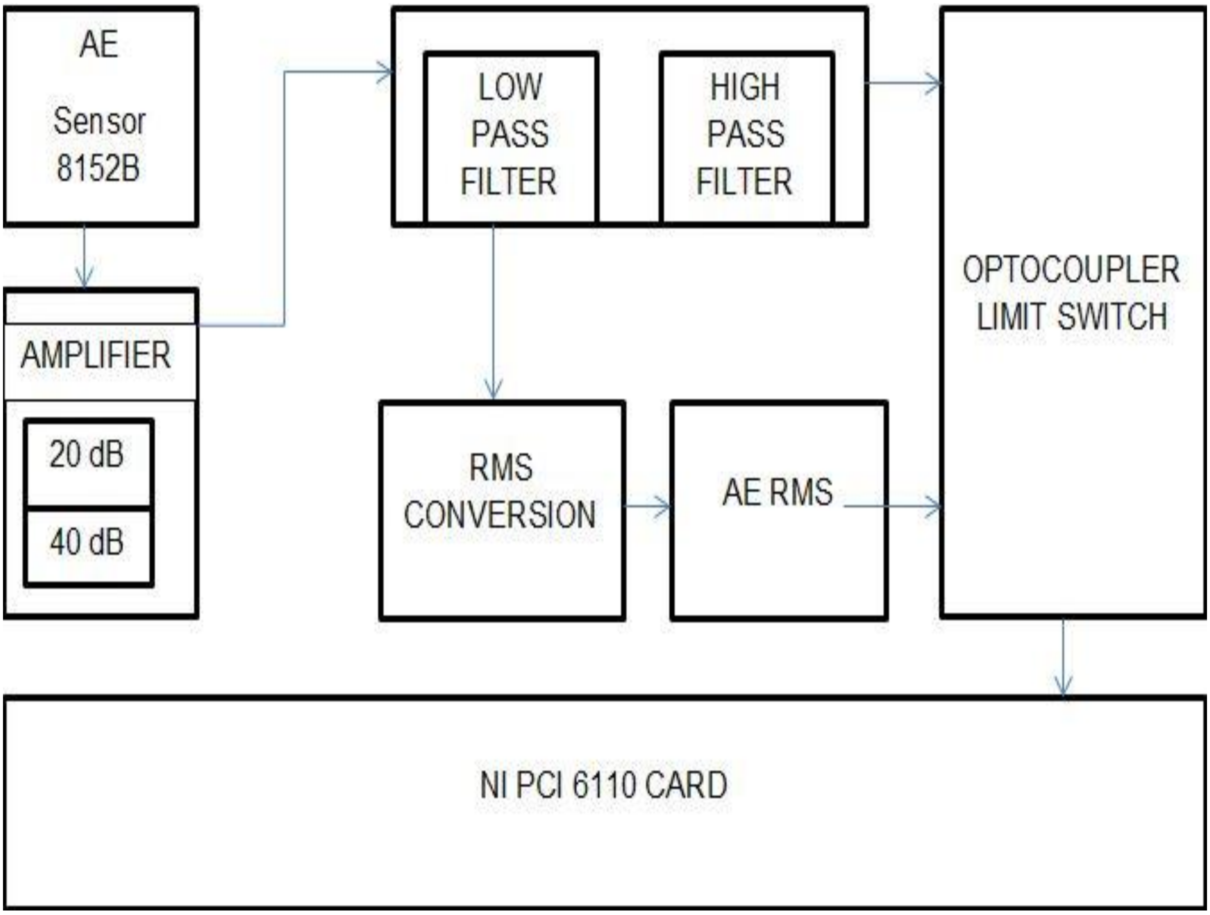

Figure 3.5: Kistler piezotron coupler circuitry from the data sheet

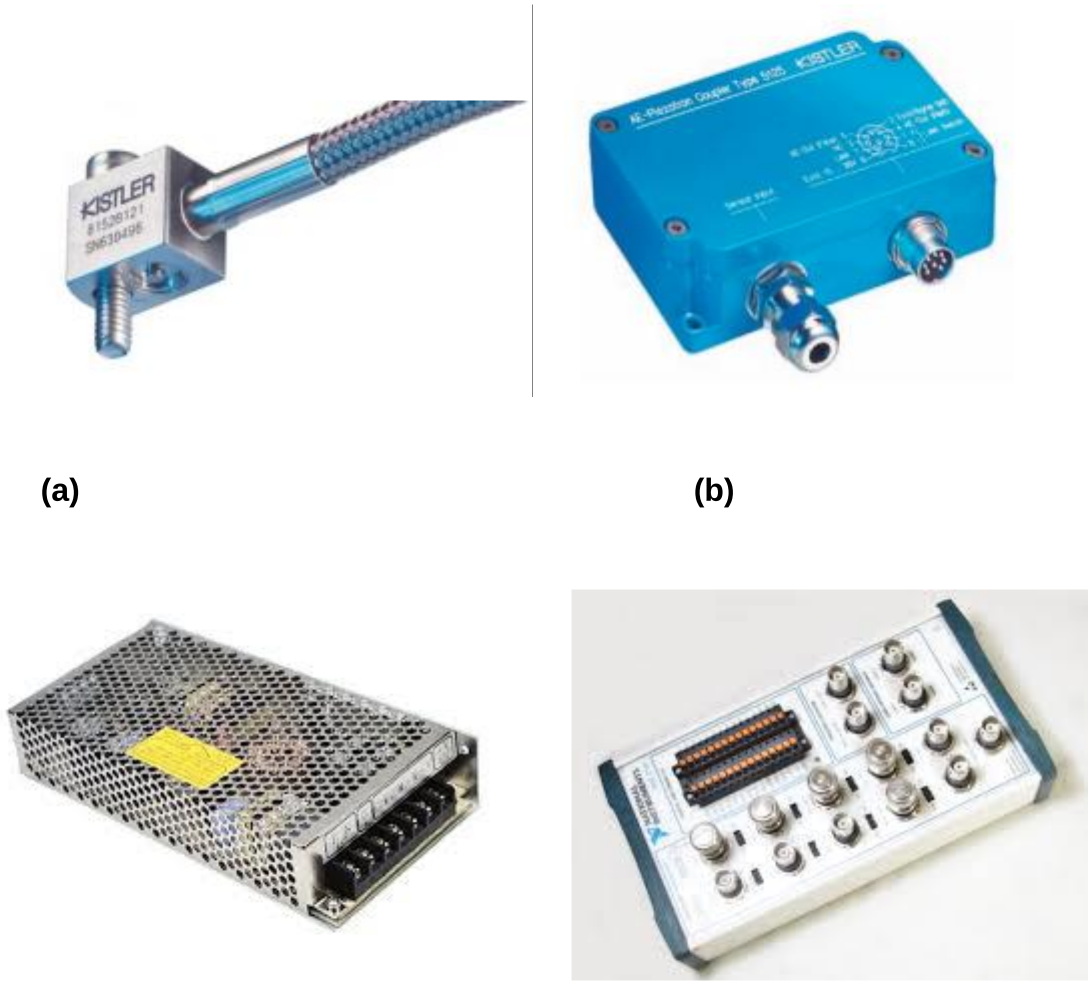

(a) **(b)**

(c) **(d)**

Figure 3.6: (a) Kistler AE sensor (b) Sensor power supply (c) AE coupler (d) NI BNC 2110 board

3.7.1: AE acquisition software design

AE Data acquisition was actualized by using NI LabVIEW virtual instrumentation software in designing the data acquisition interphase. The software consists of a front panel (Figure 3.7) and a block diagram which incorporates a GUI-graphical user interphase approach. The design employed a producer and consumer loop approach to accommodate the high sampling rate. The producer loop consists of the data acquisition VI, buffer, sequence structure, incorporating a stack sequence structure and a for-loop while the consumer loop was dedicated to saving and storing the samples in queued sequence. This concept ensured simultaneous, independent acquisition and storage of AE data thereby facilitating efficient acquisition and storage of samples which were saved for further processing. The block diagram can be viewed at the appendix.

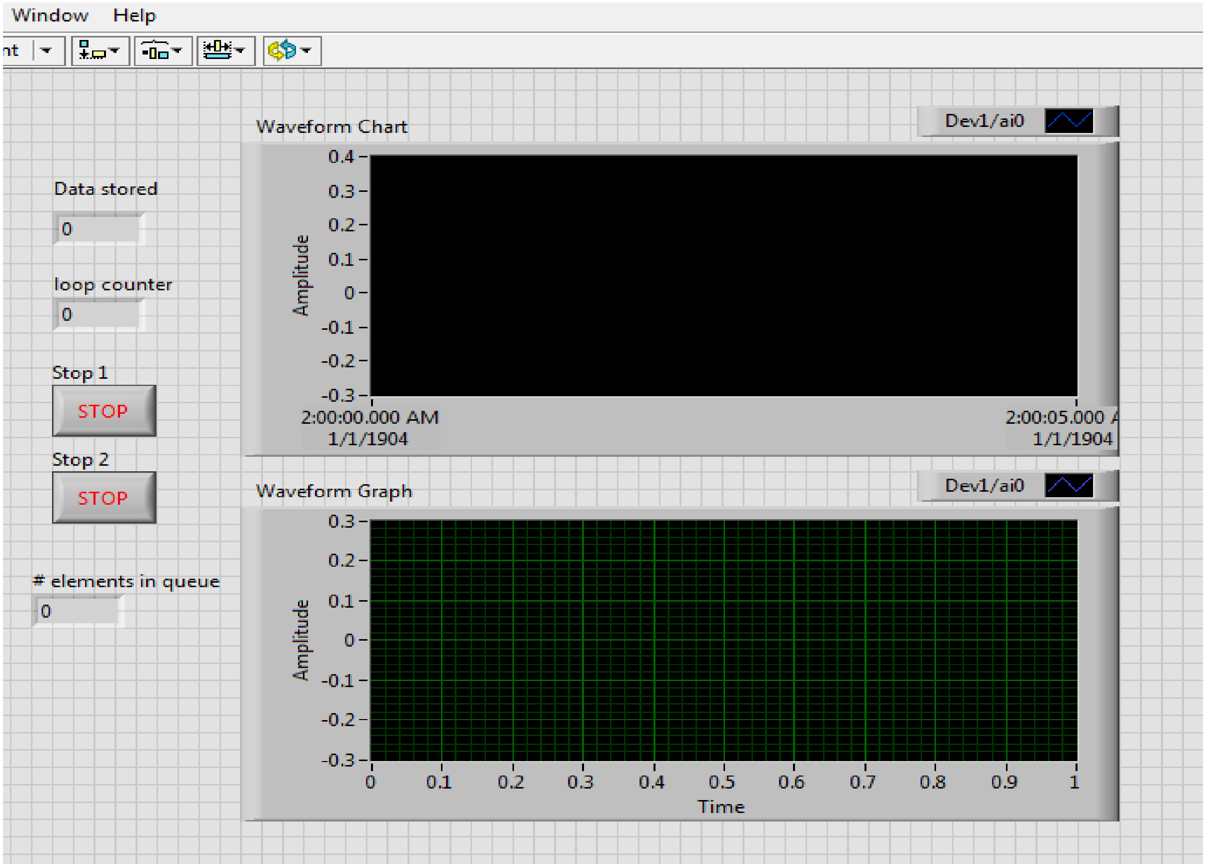

Figure 3.7: LabVIEW front panel design

3.8: SURFACE ROUGHNESS MEASUREMENT

Surface roughness measurement was carried out on a Taylor Hobson optical profiler whose features include (Figure 3.8): 300 mm diameter capability, fast stylus trace speed of 100 mm/s, automated 3D measurement, automated centre and level, high accuracy and repeatability, enhanced roughness measurements of up to 0.2 nm resolution, Steep slope surfaces of up to 85 degrees, Talymap advanced analysis with excellent report building tools.

Figure 3.8: Taylor Hobson optical profiling system

3.9: MACHINING PARAMETERS

Masuzawa and Tonshoff in their keynote paper posited that the conditions to realizing precision grinding of brittle materials are a low depth of cut, slow feed rate, high wheel rotation, and small grain size (72). They also observed a significant improvement on the surface roughness in the high precision surface grinding of ceramics when depths of cut and feed rate were reduced while the wheel speed increased. Therefore, this research considered the controllable factors to be: low depths of cut and feed rate accordingly, using high wheel rotation.

3.9.1: Wheel speed calculation

1500 surface meter per minute was selected for intermediate grinding from the precitech grinder manual.

The rpm conversion is as follows:

Convert surface meter per minute (v) to revolutions per minute (N), $v = \pi DN$

Wheel diameter (D) =0.625 inches = 0.01588 meters

1500 = π(15.89mm)N

$N = 1500/\pi(0.01588)$ = 30000 rpm.

The feed rate and depth of cut were selected to be 3(mm/min) and 5(µm) respectively which made up the center points of the model design. Lower and upper limits of each parameter were selected around the center points.

3.9.2: Box-Behnken design of experiment

Experimental designs are widely applied in controlling the effect of parameters in the precision machining process. Its application helps to reduce the number of experiments, saving time and materials resources. Furthermore, it fosters easy realization of the result, analysis and reduction in experimental errors (73).

In this research, the Box Bencken experimental design was selected to deduce the relationship between surface roughness and machining parameters. It is a spherical revolving design rotatable second order design based on 3-level incomplete factorial designs or 3 interlocking 2^2 design and a center point. The unique arrangement of these design levels allows the number of design points to increase at the same rate as the number of polynomial coefficients.

The advantages of the Box-Behnken design over other designs are such that it employs fewer design points hence it less expensive. The design also ensures that all factors are not set at their high level at the same time thereby allowing efficient estimation of the first and second order coefficients. However, it is not suited for sequential designs(73).

The research design employed a 3-factor Box-Behnken design which consists of 3 blocks of 4 experiments consisting of a full two-factor and 3 central points with the level of the third factor set as zero. A 3x3 Box-Behnken design with one center point will yield 13 runs (Figure 3.9) hence for a three-factor (k) design with three center points (c), the total number of experimental runs (N) are:

$$N = k^2 + k + c \ldots\ldots 3.2$$

$3^2 + 3 + 3 = 15$

Therefore, a 3X3 factor design parameters or control factors were selected as illustrated in Table 3.2. They were factored at three levels each to fit into the Box-Behnken design model. The design was justified with Minitab software and Design Expert as illustrated in Table 3.3.

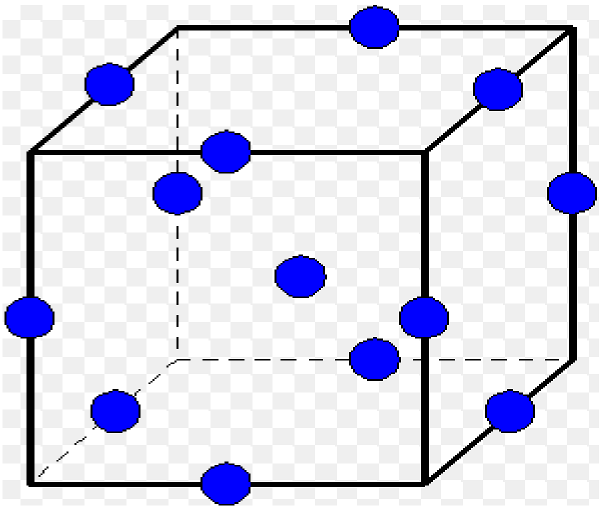

Figure 3.9: Cube representation of 3x3 Box-Behnken design with one centre point

Table 3.3: Grinding parameters and coded levels

Factors	Meaning	-1	0	1
A	DEPTH OF CUT (µm)	2	5	8
B	FEED (mm/min)	1	3	5
C	SPEED (rpm)	15000	30000	45000

Hence, a lower limit of 15000rpm and an upper limit of 45000 rpm were selected respectively with feed rates 1, 3 and 5 mm/min and cutting depths of 2, 5, and 8 µm (Table 3.2) and workpiece spindle speed of 50rpm was selected.

Table 3.4: Experimental run order with point distribution

RUN ORDER	A	B	C	Depth(µm)	Feed(mm/min)	Speed(rpm)
1	0	-1	-1	5	1	15000
2	1	0	-1	8	3	15000
3	-1	-1	0	2	1	30000
4	-1	0	-1	2	3	15000
5	1	0	1	8	3	45000
6	0	0	0	5	3	30000
7	0	1	-1	5	5	15000
8	0	-1	1	5	1	45000
9	0	0	0	5	3	30000
10	1	-1	0	8	1	30000
11	0	1	1	5	5	45000
12	-1	1	0	2	5	30000
13	0	0	0	5	3	30000
14	-1	0	1	2	3	45000
15	1	1	0	8	5	30000

3.10: EXPERIMENTAL SETUP AND PROCEDURE

The section highlights the experimental set for the ultra-high precision machining system and Acoustic emission sensing unit.

3.10.1: Setup

3.10.1.1: Machine set up

I. The work spindle was balanced at 1000rpm clockwise direction thereby achieving a spindle run out error of 3.26µm high, 3.255µm low and 0.005µm P-V. This balancing was done using Precitech's DIFFSYS software interphase to ensure the vacuum chuck was well positioned hence avoiding unwanted oscillation patterns on the surface of the workpiece which would deteriorate the surface roughness of the workpiece and to ensure even contact all through workpiece surface and wheel tip.

II. Once the tool was centred, the bk7 glass was attached to a custom made copper arbour with the help of wax (Figure 3.10). The wax was melted on a heated fluid container and the arbour was dipped into the wax while the glass was quickly attached before the wax solidified.

III. A major challenge was actualising the height setting of the grinding wheel to coincide with the centre point of the workpiece this was achieved at a height setting coordinates of x= 97.493mm and z=-195.738 mm.

Figure 3.10: Wax for the Bk7 mounting process

3.10.1.2: Single point inclined axis set up

I. The spindle was installed with the horizontal configuration on the rotary B axis using A17750 (top) and A16810-04(bottom) mounts (Figure 3.11).

II. To achieve the single point inclined axes configuration, the grinding spindle was rotated on the B axis to an angle of 359 degrees with the help of the balancing software (Figure 3.12). Such that only the cube tip of the wheel was in contact with the workpiece. This was done to allow easy chip removal as the chip storage space of the fine grit resin bond wheel is extremely small

III. Challenge 300-HT grinding fluid was mixed with water at a ratio of 1:50. The grinding fluid was set to trickle down from the nozzle supply at the rate of 0.5ml per second.

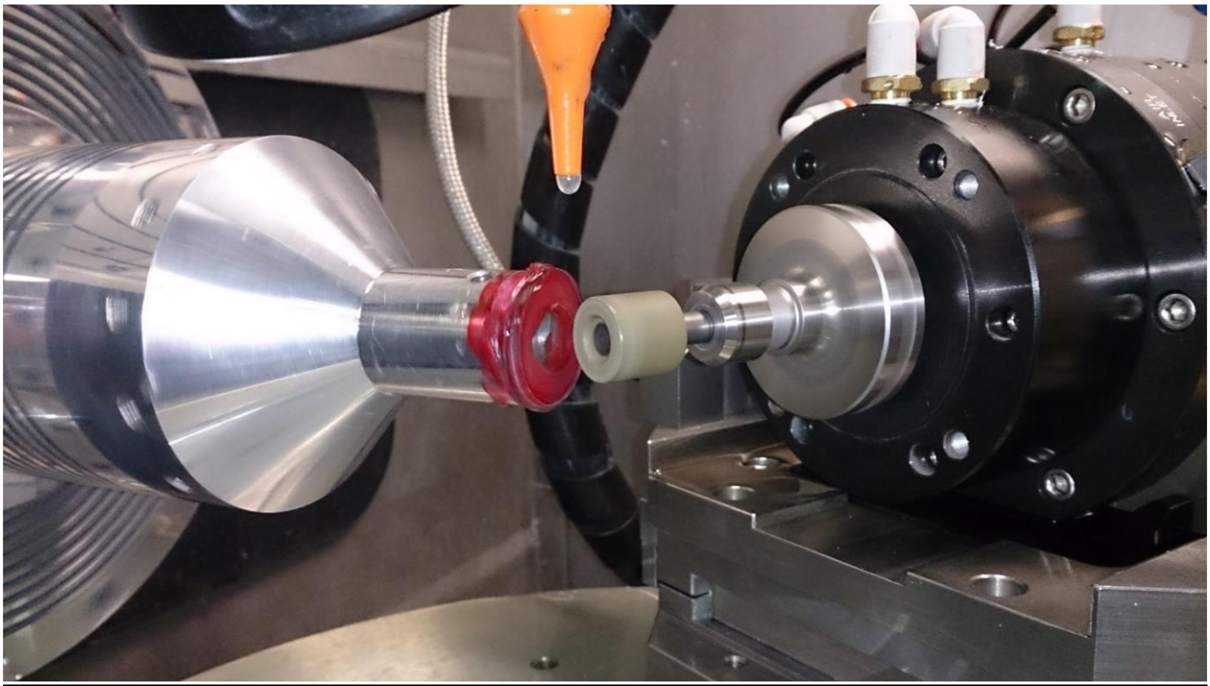

Figure 3.11: Experiment setup

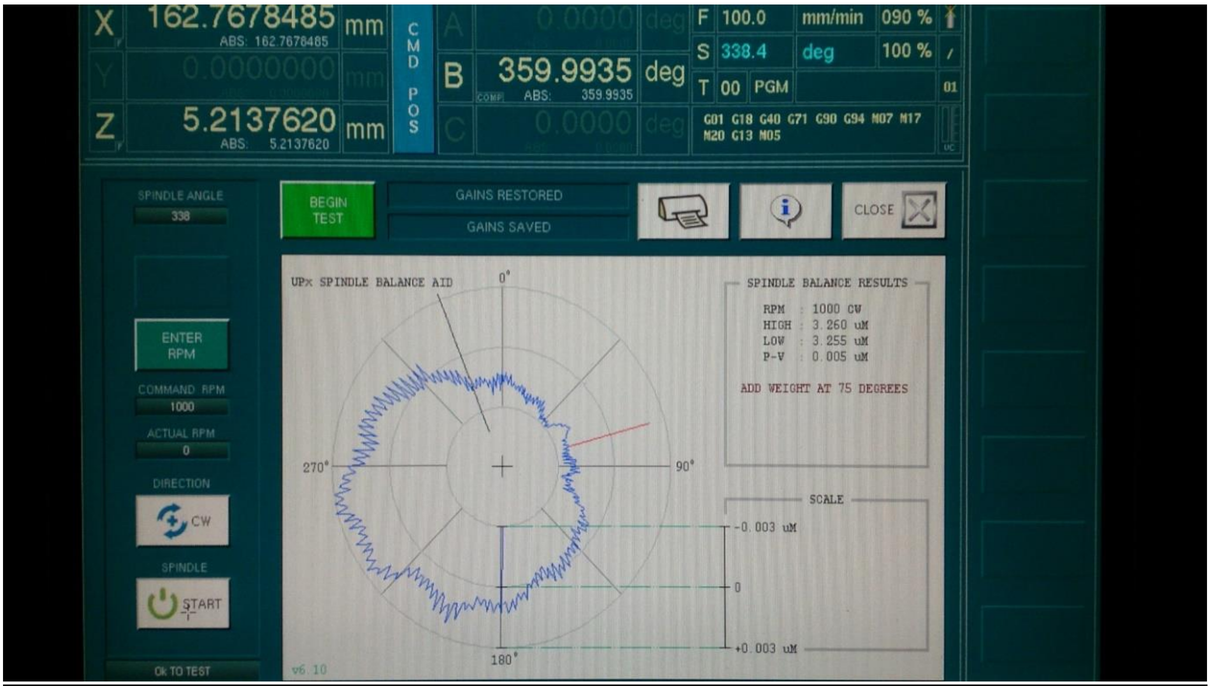

Figure 3.12: Spindle balancing platform DIFFSYS

3.10.1.3 Acoustic Emission set up

I. With the help of a magnetic clamp and M6 bolt, the AE sensor was fastened to the spindle mount at a distance of 4cm from the workpiece (Figure 3.13). The distance is close enough to detect surface and Rayleigh acoustic waves from the workpiece.

II. The AE coupler was attached directly above the set up to give room for the free rotation of the spindle on the B-axis and its travel on the X-axis without interference with the set up (Figure 3.13). This was also necessary to maintain the pre-processing unit as close to the acquisition point as possible and eliminate the effect of workpiece changing distance.

III. Pre-processed signals were channelled to the BNC board and to the NI data card for further processing and storage.

3.10.2: Procedure

I. The experiment was pre-run at a feed rate of 6mm/min and workpiece spindle speed of 100rpm then the work spindle speed was reduced to 50 rpm. This was done to clean the surface of the workpiece and achieve an evenly flat surface on the workpiece.

II. At the point it was previously observed that the contact noise of the wheel tip or edge with the surface was uneven, this was corrected by adjusting the programmed coordinates. Hence, each pass was run at the selected experimental trial parameters.

III. After each pass the arbor was removed from the workpiece spindle, the ground surface was cleaned and placed under the optical profiler for surface roughness measurement (Figure 3.14) without separating the workpiece from the arbor.

IV. Three measurements were taken and the average recorded.

The arbor and workpiece were then centered back on the work spindle using the centering software at the original coordinates to continue with the next selected parameters.

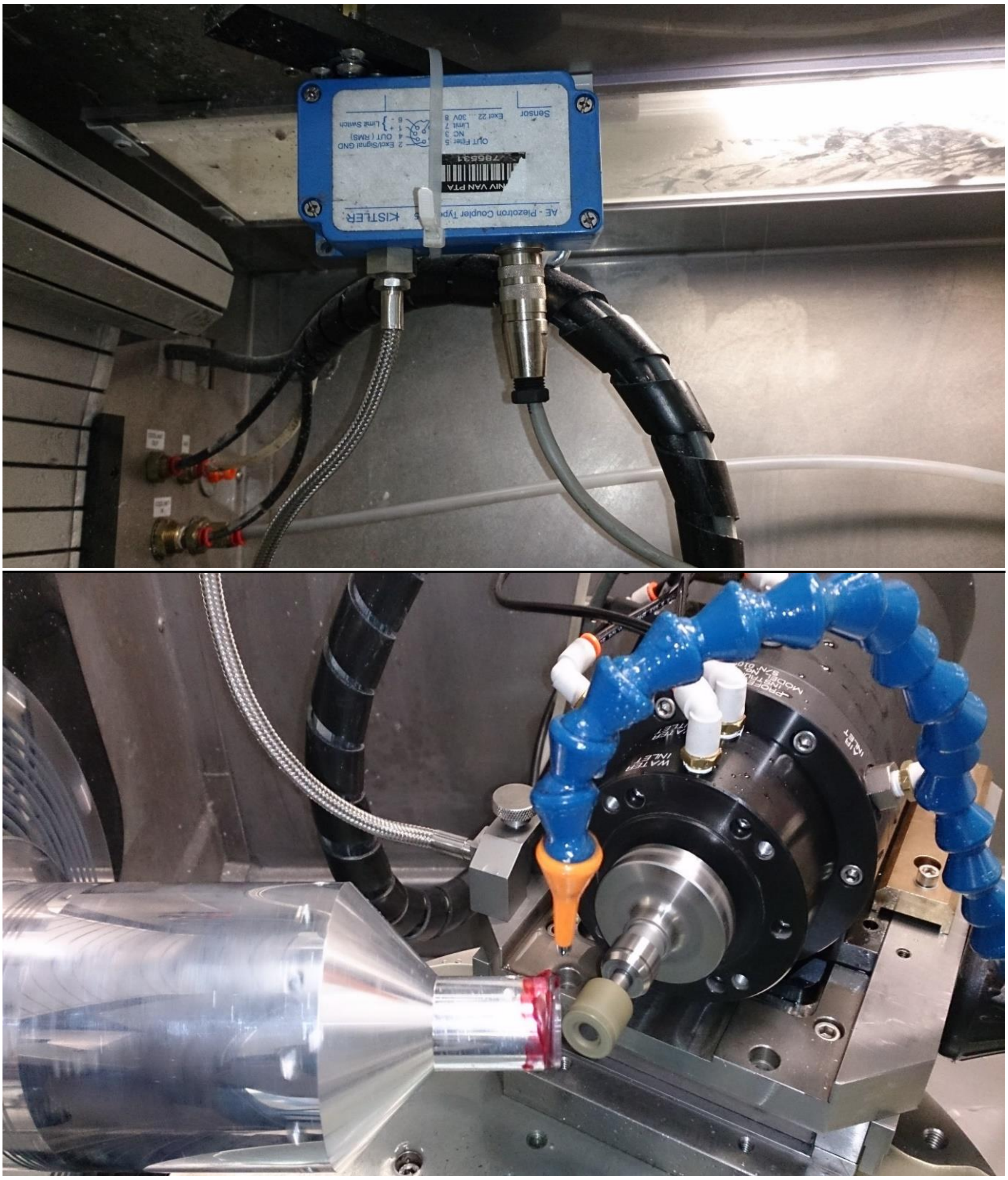

Figure 3.13: Acoustic acquisition set up

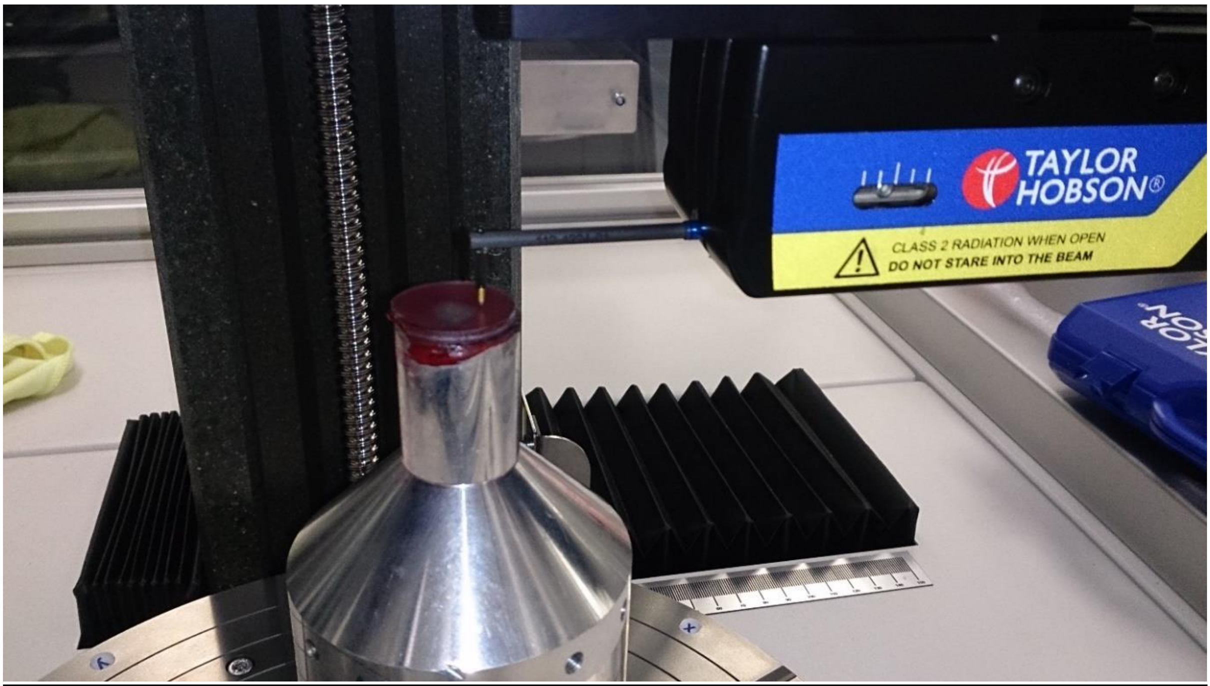

Figure 3.14: Surface roughness measurement with Taylor Hobson optical profiler

3.10.2.1: AE Signal Acquisition procedure

I. The sensor surface was wiped thoroughly clean of previous chips and dirt that may interfere with the sensitivity and acoustic coupling of the acquisition system.

II. Firstly, the data acquisition setup was run without spindle-work piece contact at different spindle speeds of 15000rpm, 30000rpm and 45000rpm respectively with the coolant supply. This procedure was initiated to determine the noise frequency of the grinding spindle and other environmental influence.

III. During the grinding cycle, AE data acquisition was initiated when the wheel must have advanced 12mm into the diameter of the workpiece. The acquisition start time varied with the feed rate of each experimental run. This acquisition was close to the centre of the workpiece.

IV. The AE signal was acquired at a high sampling rate of 2MHz through each grinding cycle and all through the experiment.

3.11 CONCLUSION

The Box-Behnken design was applied in creating 3X3 experimental domain involving careful selection of machining parameters. AE sensing unit was also actualized using LabVIEW. Chapter 4 details the result and analysis.

CHAPTER 4
RESULT AND DISCUSSION

4.1: INTRODUCTION

The first section of this chapter details the application of regression analysis to develop a response surface model for predicting the surface roughness values and the investigation of the interactive terms of the model and its validation. The second section highlights the signal processing of acoustic emission data acquired during the research. It employs the use of Bolls spectral subtraction technique, feature extraction and selection of relevant features in the time, frequency and time-frequency domains using statistical and wavelet decomposition techniques. Finally, details of the training and testing of back a propagation neural network using the selected features as inputs for predicting surface roughness values are discussed. The analysis in this chapter was made possible using Minitab, Statistica, Matlab, Labview and Design Expert software.

4.2: SURFACE ROUGHNESS OBSERVATION

Earlier research has shown that the use of resin bond diamond grinding wheel results in lower normal grinding force compared to metal bonded diamond grinding wheels under the same process conditions (74). As a result, a lower value of grinding force per unit contact area exists between the wheel and the workpiece and also the cumulative sliding length of the cutting edge hence the possibility of low wheel wear. However, this is considered insignificant in this study. Moreover, newly acquired wheels do not require dressing. The diamond wheels used in the research are new, hence, the effect of the wheel dressing on the surface roughness is also considered insignificant for this research.

The measured surface roughness values varied from a lower limit of 130nm to a maximum value of 320 nm over a range of 190nm (Figure 4.1 and Table 4.1). This shows a significant variation of surface roughness from the parameter combination in the experimental design. This variation in the surface roughness values can be attributed to the different grinding conditions, and the effects of small undeformed chip thickness at a lower depth of cut while using diamond grinding wheel in grinding hard and brittle materials (75).

Table 4.1: Experimental run and result

Run Order	Depth(um)	Feed(mm/min)	Speed(rpm)	Ra(nm)
1	5	1	15000	130
2	8	3	15000	300
3	2	1	30000	150
4	2	3	15000	180
5	8	3	45000	220
6	5	3	30000	240
7	5	5	15000	320
8	5	1	45000	180
9	5	3	30000	230
10	8	1	30000	180
11	5	5	45000	210
12	2	5	30000	220
13	5	3	30000	240
14	2	3	45000	215
15	8	5	30000	260

Figure 4.1: Series plot for surface roughness

Table 4.2: Classification of surface roughness values

Experimental run	Interval (nm)	Classification
01,03,04,08,10	130 - 180	Good
05,06,09,11,12,13,14	190 - 250	Average
02,07,15	260 - 320	Poor

For ease of analysis, surface roughness values were divided into three groups to suit the experimental domain (Table 4.2). The lowest roughness value of 130nm occurred at a low feed of 1 mm/min, depth of 5µm and speed of 15000rpm and most good surface roughness ranges were also observed at low levels of feed within the selected machining parameters. Occasionally, medium levels of either feed or depth and increased speed yielded good surface finishes (Table 4.1). This suggests that better surface finish can be obtained preferably at low levels of feed for ultra-high precision grinding of Bk7 glass.

The highest roughness value of 320nm corresponds with a feed rate of 5mm/min at the same wheel speed and cutting depth values for 130nm (Table 4.1). This suggests that the increase in feed played a significant role in the generation of poor surface roughness. These findings are consistent with the critical conditions for brittle to ductile transition since larger feed rate causes deeper penetration depth thereby causing the ground surface to exhibit more degrees of brittle fracture hence increasing the surface roughness values (19).

Other poor roughness conditions of 260nm and 300nm occurred at high levels of cutting depth, high and medium levels of feed but not at a high level of wheel rotation. The high and medium levels of wheel speed (45000rpm and 30000rpm respectively) generated average surface roughness values which were observed to reduce with increase in wheel speed depending on the levels of the other parameters. However, a combination of low depth and feed with low speed resulted in low roughness value (experiment 4, Table 4.1). This suggests the possibility of interaction effects within the different levels of the machining parameters

Furthermore, medium levels of cutting depth and feed rate generated average roughness categories while poor surface finishes generally occurred with increase in feed rate, depth of cut and sometimes wheel speed. However, none of the poor surface finishes correspond to the case of highest wheel speed selection. Although Mazuwa and Tonshoff posited low feed, low cutting depth and high wheel rotation as conditions to realizing precision grinding of brittle materials (72), these conditions have been applied in UHPG of bk7 glass but it is not conclusive to say that an increase in the wheel rotation within the experimental domain impacts positively on the surface roughness at this stage as extremely high speeds within the experimental domain has shown an increase in surface roughness values in the research.

Gu et al while investigating different modes of grinding bk7 glass (19) suggested that the feed to depth ratio determines the surface roughness after all the conditions for brittle to ductile transition are met. He also concluded that the effect of grinding depth on surface roughness is weaker than feed rate hence MRR can be increased by increasing the depth of cut while keeping feed constant(19). Two out of the three poor surface roughness outcomes were observed to coincide with high cutting depth values of 8µm and the third poor outcome of 320nm coincided with medium cutting depth of 5µm. On the other hand, two out of the three poor surface outcomes also coincided with highest feed rates 5mm/min while 300nm value coincided with medium feed value of 3mm/min.

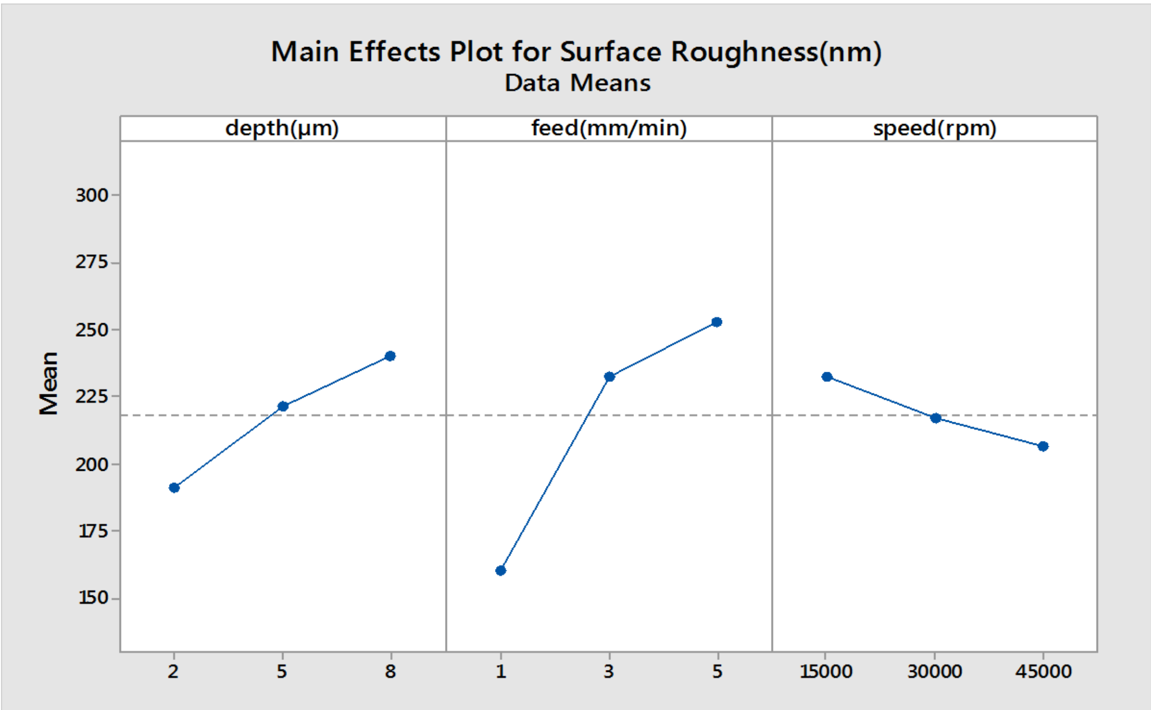

Figure 4.2: Main effects plot from experimental design

Main effects plot generated from the design of experimental points and surface roughness values supports some of the findings, indicating an increase in response surface when feeds and cutting depth levels were increased. However, changes in speed levels are seen to have complete inverse effects on the response surface from the plot (Figure 4.2). To further investigate and understand the nature of the effects of cutting depth, feed, main and interactive effects of the machining parameters, a response surface model was developed.

4.2: RESPONSE SURFACE MODELLING

RSM is a collection of mathematical and statistical methods which are useful for analysing engineering problems. This method employs regression analysis to determine the best fit for a series of responses. The best fit represents the best prediction of values for the modelled response. RSM has the ability to quantify the relationship between controllable input parameters and the generated response surface (76).

Procedure for developing response model:

I. Design of experiment to adequately measure the response
II. Check for normality of responses and transform if necessary.
III. Develop a mathematical model of the second order response surface with best fitting
IV. Finding the optimal set of experimental parameters that produce a maximum and minimum value of response
V. Representing the direct and interactive effects of process parameters through 2 and 3-dimensional plots

If all the variables are assumed to be measurable, the response surface can be expressed as follows.

$$y = f(x_1, x_2, x_3, \dots \dots \dots \dots x_n) \dots \dots \dots \dots \dots \dots \dots \dots \dots \dots \dots \dots \dots \dots \dots \dots \dots \dots \dots .4.1$$

$$y = bX + \varepsilon \dots \dots \dots \dots \dots \dots \dots \dots \dots \dots \dots \dots \dots \dots \dots \dots \dots \dots \dots \dots \dots \dots \dots \dots \dots \dots \dots \dots \quad 4.2$$

$$y = \beta + \sum_{i=1}^{n} \beta_i x_i + \sum_{i=1}^{n} \beta_{ii} x_{i^2} + \sum_{i=1}^{k-1} \quad \sum_{j=2}^{k} \beta_{ij} x_i x_j + \varepsilon \dots \dots \dots \dots \dots \dots \dots . .4.3$$

4.2.1: Normality Test

The Null Hypothesis (H_0) for the Normality test is that the data is normally distributed. Therefore, a p-value which is greater than or equal to 0.05 should indicate a normal distribution of the response data. A p-value of 0.667 from the probability plot (Figure 4.3) supports the null hypothesis. The low Anderson-Darling statistic which is a measure of the goodness of fit indicates a good fit. Therefore, there was no need for transformation of the roughness data.

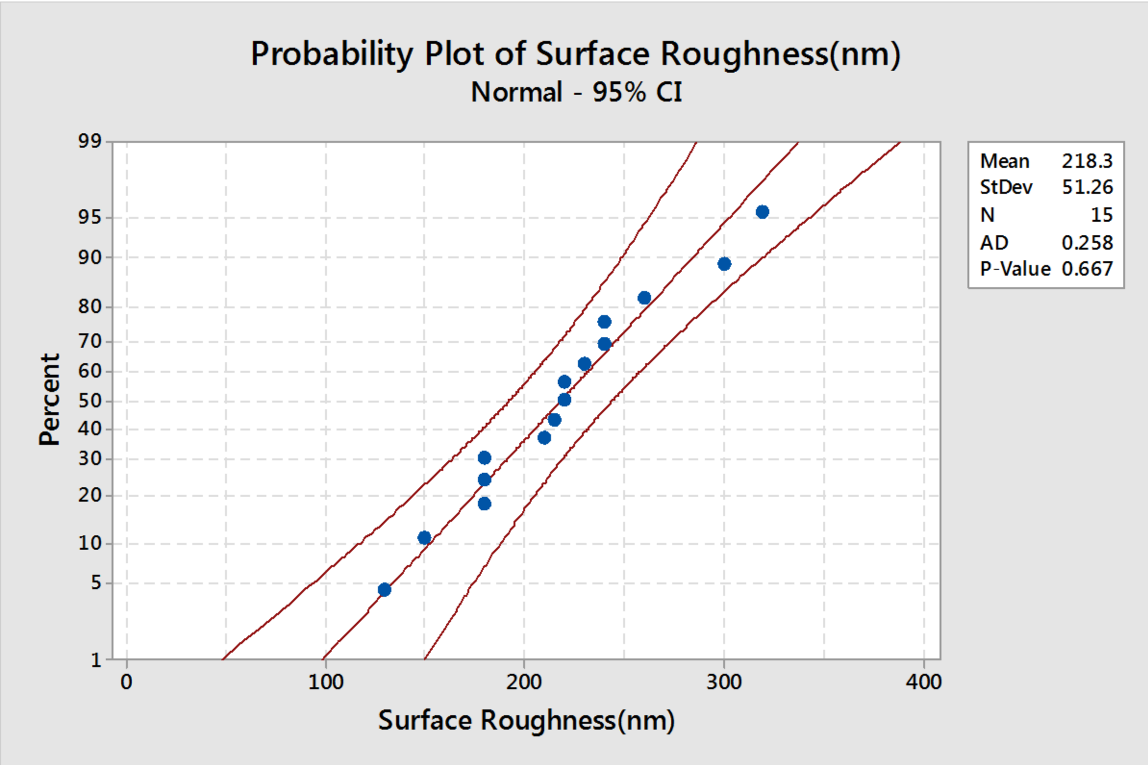

Figure 4.3: Probability plot for Normality test

4.2.2: Determination of appropriate polynomial equation for the RSM

The sequential sum of square and lack of fit test were used to determine the suitable terms for the polynomial. The goal is to select the highest order polynomial where the additional terms are significant and the model is not aliased while the lack of fit test ensures the model has an insignificant lack of fit. From the results (table 4.3 and table 4.4): A Lack of fit value of 3 indicates that the quadratic model lack of fit is insignificant. Hence quadratic and 2FI (two-factor interaction) model was selected for the response surface polynomial.

Table 4.3: Sequential sum of squares result

Source	df	Sum of squares	Mean square	f-value	p-value	Remark
Mean vs total	1	$7.1x10^5$	$7.1x10^5$			
Linear vs mean	3	23243.75	7747.92	6.29	0.0096	
2FI vs Linear	3	9731.25	3243.75	6.81	0.0136	
Quadratic vs 2FI	**3**	**2722.92**	**907.64**	**4.18**	**0.0788**	**Suggested**
Cubic vs Quadratic	3	1018.75	339.58	10.19	0.0907	Aliased
Residual	2	66.67	33.33			
Total	15	$7.1x10^5$	50121.67			

Table 4.4: Lack of fit test result

Source	df	Sum of squares	Mean square	f-value	p-value	Remark
Linear	9	13472.93	1496.9	44.9	0.0022	
2FI	6	3741.67	623.61	18.71	0.0516	
Quadratic	**3**	**1018.75**	**339.58**	**10.19**	**0.0907**	**Suggested**
Cubic	0	0.00				Aliased
Pure error	2	66.67	33.33			

4.2.3: Regression Analysis

Regression analyses have been utilized to determine the significance of the individual parameters in a fitted response, their powers and interactions on the response surface. It entails fitting the independent and response variables to validate if the relationship between them is linear, two-factor interaction (2FI), or involving second order or higher order functions. A proposed response surface model with coefficients of independent variables, cross terms and higher order terms is highlighted in equation 4.4

A **3x3** Box Behnken design with 3 center points will reflect 10 coefficients in a quadratic and 2FI model as follows:

$\check{R} = B_o + B_1 d + B_2 f + B_3 s + B_4 d^2 + B_5 f^2 + B_6 s^2 + B_7 df + B_8 ds + B_9 fs$ ……………… 4.4

Where:

$\check{R}$= Response surface

B_0= Intercept

d= depth of cut

f= feed

s= speed

B_1-B_3= coefficients of the first order term in the model.

B_4-B_6= coefficients of the second order term in the model.

B_7-B_9= coefficients of the cross term in the model.

4.2.3.1: Assumptions for a regression model

The p-value of an observed value $t_{observed}$ of some random variable T used as a test statistic is the probability that, given the null hypothesis is true, T will assume a value as or more unfavourable to the hypothesis as the $t_{observed}$ value in the analysis of variance (ANOVA (77). Hence, the p-value represents the significance of a result. The smaller the p-value in relation with the set confidence interval, the more significant the result (78). The p-value tests the null hypothesis that the corresponding coefficient equals zero (no effect), therefore low p-values indicate that the predictor is a meaningful addition to the model.

Five iterations were used to determine the best fit model. The significant terms after the fifth iteration were used to develop the response surface model since their p-values were less than 0.05 (Table 4.5).

Table 4.5: Regression analysis showing significant terms

	b	Std error of b	t(5)	p-value
Intercept	-125.69	34.148	-3.681	0.00621
Depth	27.29	4.559	5.986	0.00033
Feed	101.96	12.124	8.410	0.00003
Speed	0.006	0.001	6.253	0.00025
Feed*Feed	-6.473	1.669	-3.880	0.00468
Depth*speed	-0.001	0.0001	-4.459	0.00211
Feed*Speed	-0.001	0.0002	-6.204	0.00026

.

Equation 4.5 and 4.6 are the developed response surface model.

$$\check{R}a = B_o+B_1d+B_2f+B_3s+B_5f^2+B_7df+B_8ds+B_9fs \quad \ldots\ldots 4.5$$

$$Ra = -125.699 + 27.292d + 101.964f + 0.006s - 6.473f^2 - 0.001ds - 0.001fs \quad 4.6$$

The standardized coefficients in Table 4.5 depict how many standard deviations the response variable will increase per standard deviation increase in a predictor variable, therefore, it helps to understand the effect of the independent variable on the response when they are measured in different units. The coefficients of the developed model are summarized in (Table 4.5). Although feed has the highest standardized coefficient which means that the effect of feed is the most significant on the response surface (Figure4.4), this cannot be considered alone because of the significant interaction terms present between feed and speed then depth and speed. The second order feed term has the highest p-value of 0.00468, on the other hand, does not indicate the least value of standardized coefficients (Figure 4.4). The percentage contribution of the model terms and their f-values can be found in (Table 4.6).

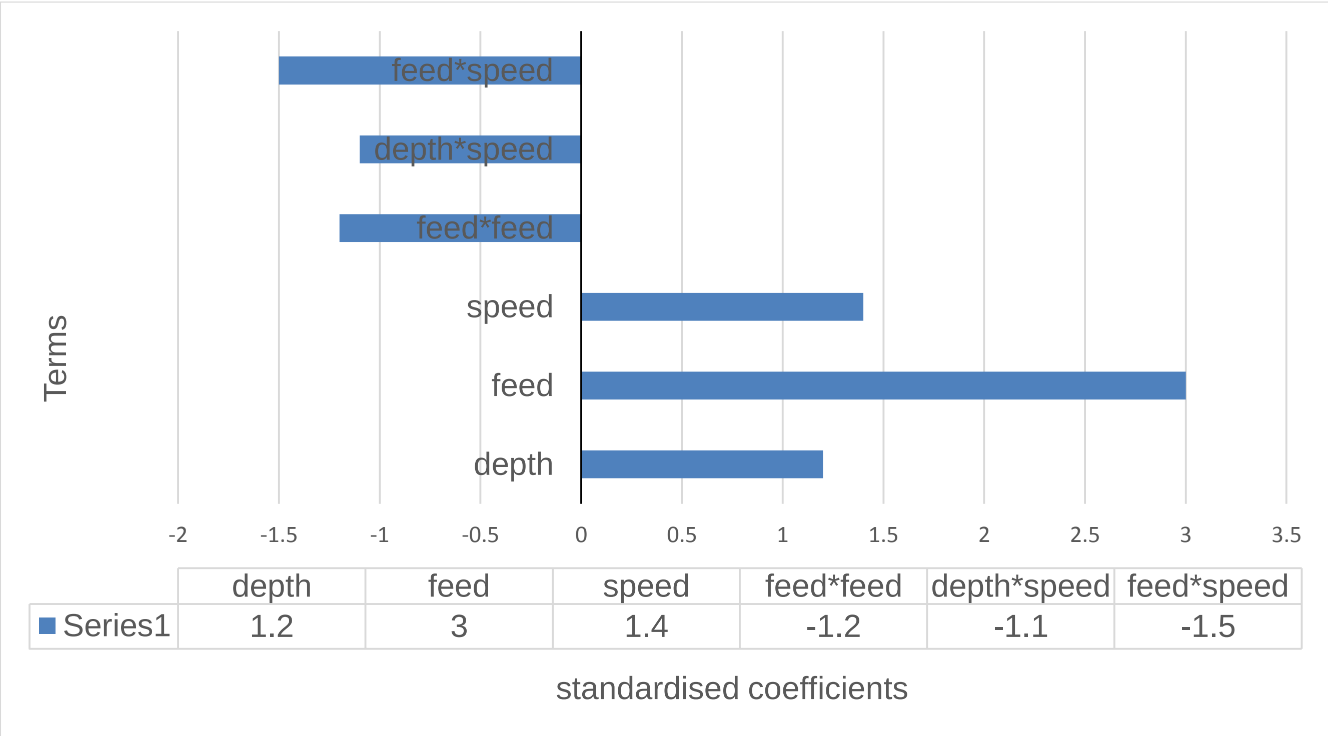

Figure 4.4: Standardized coefficient plot

Table 4.6: F-test

source	Contribution (%)	F-value

Model	96.38	35.53
Depth	12.12	35.83
Feed	46.52	70.73
Speed	3.75	39.10
Feed*Feed	6.8	15.05
Depth*speed	8.9	19.88
Feed*Speed	17.4	38.49

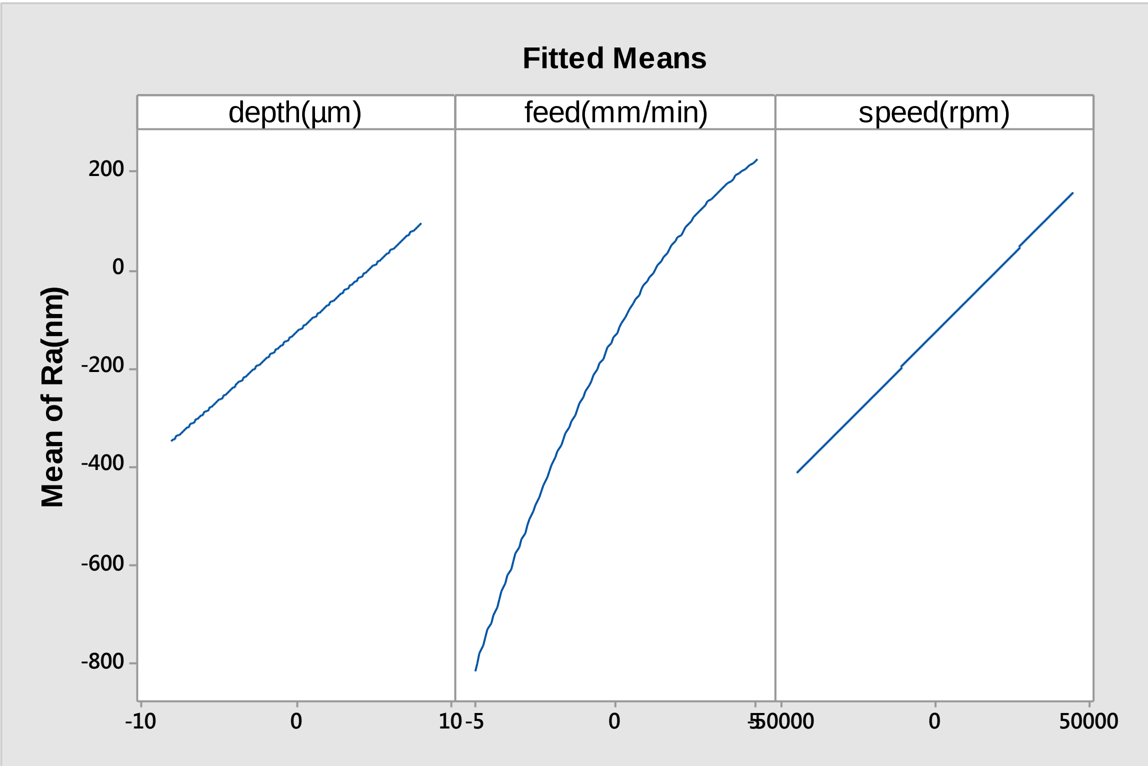

Figure 4.5: Main effect plots for surface roughness from developed model

Fitted means are helpful for obtaining more precise results by accessing response differences due to changes in factor level rather than differences due to unbalanced experimental condition (79). The main effects plot from a model helps to examine the differences between level means for one or more factors. A horizontal line parallel to the x-axes indicates that there is no main effect hence the response mean is the same across all factor levels. On the other hand, a steep slope indicates greater main effect.

Figure 4.5 highlights the effect of the predictor variables on the response surface from the model. The feed has a very steep slope compared to the depth and speed therefore indicating a high correlation between surface roughness and feed rate. This relationship is not perfectly linear as can be seen with the slight curve at the higher values of feed showing the influence of the significant quadratic feed term in the model. The curve on the feed term also suggests that the impact of the feed on the response surface changes after a certain level, hence further investigation is needed.

The steep slopes of the depth and speed also indicate main effects on the response. In the absence of interactions, the feed rate could be imagined to hugely influence the response variable followed by the depth of cut and speed as seen from the steepness of the slope. Ideally, the main effect of these factors cannot be considered alone. According to Montgomery et al whenever a strong interaction exists between two factors or variables, the corresponding effects of the main factors have little or no practical significance (78). In this case, the effect of the main factors are of practical significance but cannot be considered alone due to significant interactions as seen from the p-values.

It is also observed that the speed effect is quite different from the main effects plot Figure 4.2 and Figure 4.5. A possible explanation of this occurrence can be found in section 4.2.4.3.

4.2.4: Interaction effects in the response surface model

From equation 4.6, the effect of feed rate and depth of cut on the response variable are both dependent on the speed. The developed model does not indicate a direct significant interaction between the feed and depth of cut this is indicated by the empty blocks in the combined matrix plot of Figure 4.6.

Fitted means were employed to analyze the effect of one factor dependent on the level of another. Parallel lines in an interaction plot indicate no interaction

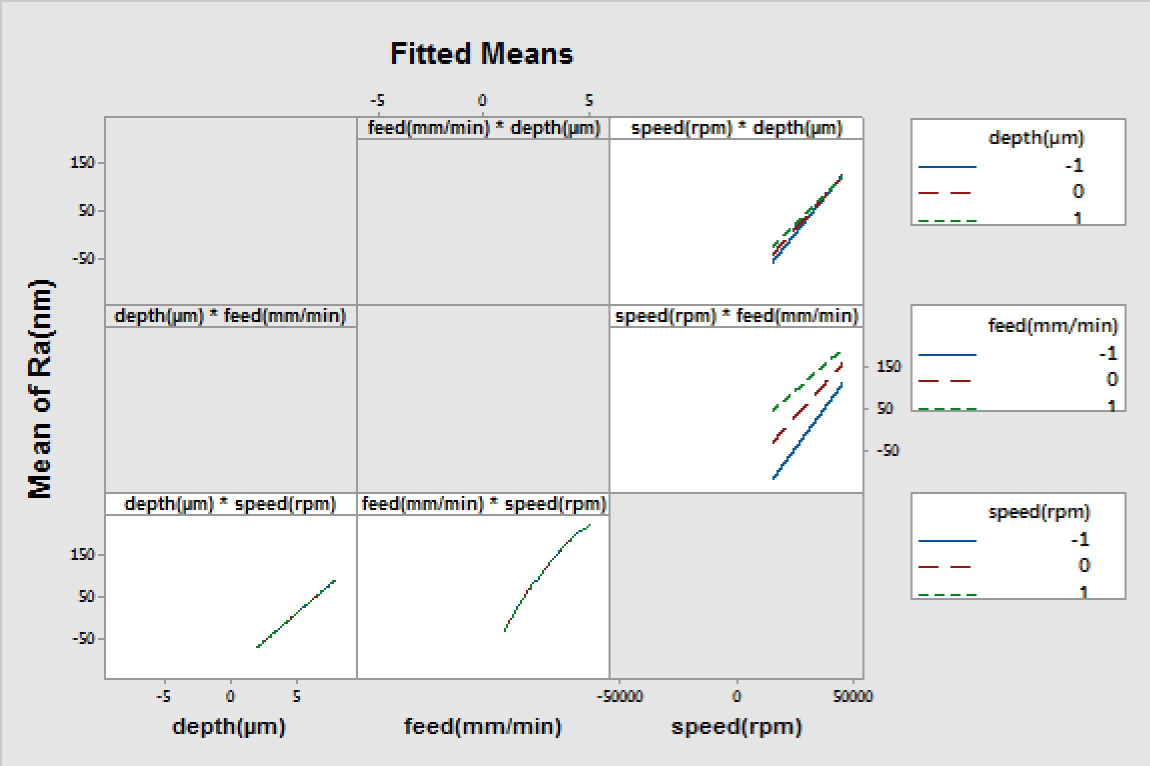

Figure 4.6: Interaction matrix plot of model terms and surface roughness

.

4.2.4.1: Feed and speed interaction

Interactions are observed with the superimposition of the coloured lines when the speed increases with an increase in the feed, the mean surface roughness increases both linearly and in a quadratic manner, this pattern of increase in the surface roughness is similar at different levels of speed (Figure 4.6). On the other hand, reversing the axes of speed and feed gives another perspective which indicates an increase in mean surface roughness with a corresponding increase in speed and feed. This suggests that better surface roughness conditions can be achieved with low feed and speed.

4.2.4.2: Speed and depth interaction

The interaction plot shows that surface roughness value increases with an increase in depth and speed. The effect is such that lower depth of cut and low speeds give the best surface roughness value but an increase in the depth of cut while keeping the speed constant will yield a higher roughness value while an increase in speed values at the same depth of cut gives a similar surface roughness values (Figure 4.6).

4.2.4.3: More investigation

So far, we have investigated the effect of the interaction terms on the model. If we recall, the model doesn't indicate a significant interaction between feed and depth but the speed interaction is common to both feed and depth hence it is necessary to access these combined interactions. To further access the effect of the model and the predicted values, the combined interaction of the predictor variables were investigated with 2D and contour plots.

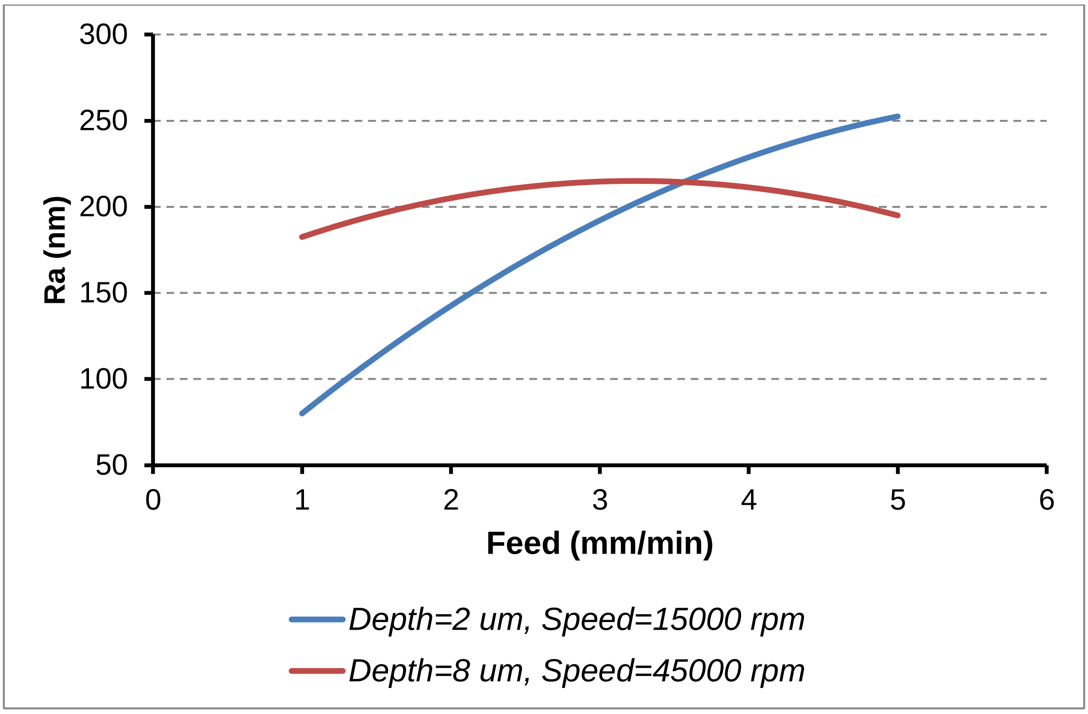

Figure 4.7: 2D profile plot of feed against depth and speed.

It was observed that at the constant low value of depth and speed, the surface roughness increases almost linearly with increased feed and the surface roughness values for the high values of speed and depth are higher (Figure 4.7). Interestingly, for the high constant values of speed and depth, the surface roughness values begin to drop beyond 3mm/min feed value as indicated with the red line (Figure 4.7).

It is also observed that at high speeds and cutting depth, an increase in feed does not result in a wider range of change in surface roughness values compared to the range of change at low speeds and depth, therefore, the maximum and minimum values in this condition are almost the same (Figure 4.7). This further highlights the effect of the quadratic feed term in the model and justifies the fact that at higher values of feed and depth, the surface roughness can be improved by increasing the speed.

On the other hand, at the constant low level of feed, an increase in speed and cutting depth generated good and average surface roughness values (Figure 4.8a). These findings from the interaction effect explain the discrepancy between main effects plot obtained from the experimental design (Figure 4.2) and model (Figure 4.5).

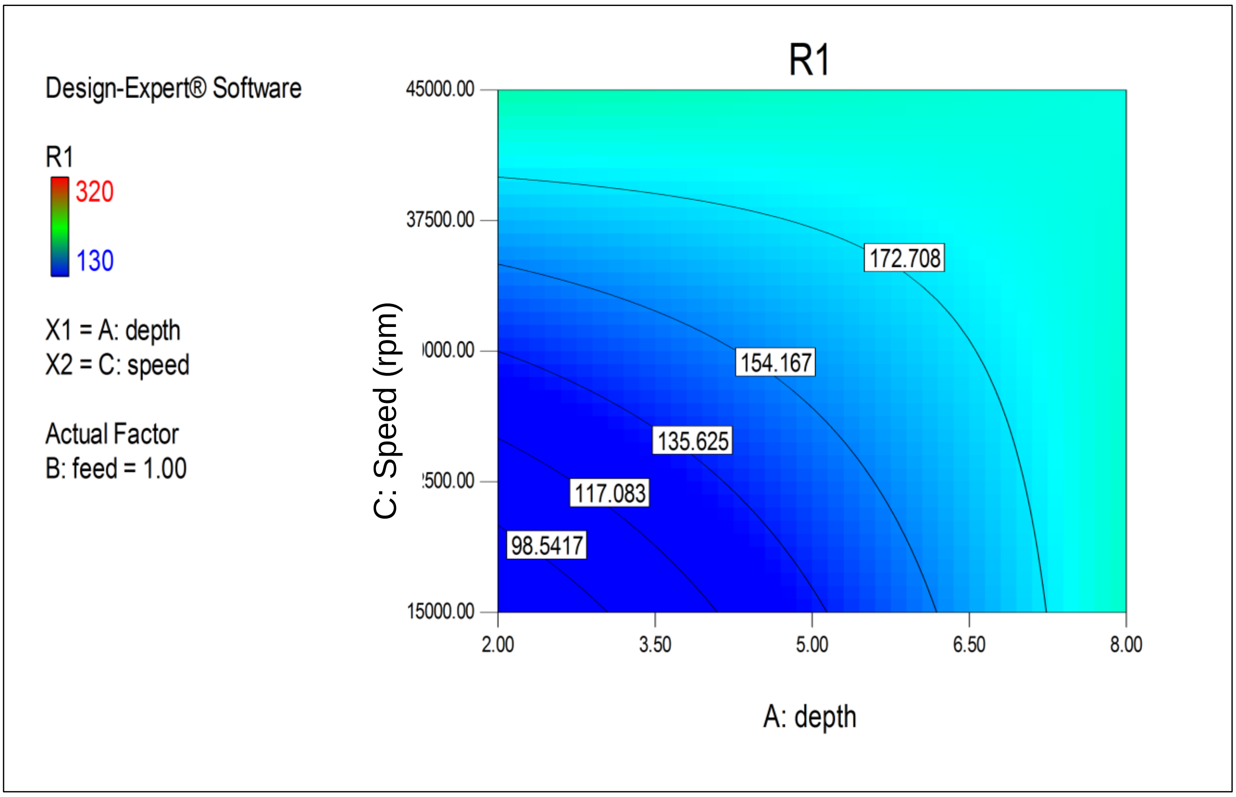

Figure 4.8a: Contour plot at low level of feed

The red zone from the contour plot (Figure 4.8b) also shows that a high level of feed, an increase in the depth of cut generates very poor surface roughness values.

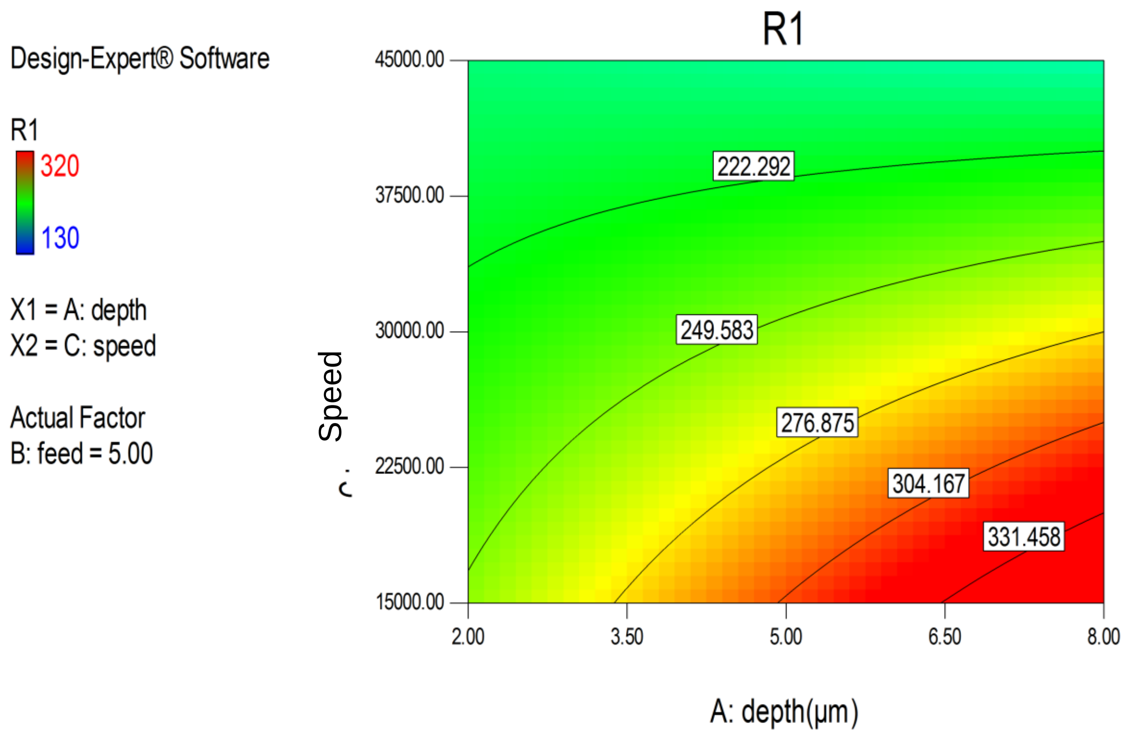

Figure 4.8b: Contour plot at high level of feed

4.2.5: Optimization

One of the major goals in manufacturing precision optics is to minimize the surface roughness with the ideal combination of variables. An individual desirability (D) accesses how well a set of combination of variables identifies the defined target for a single response. A desirability value of zero signifies that the response is outside the acceptable limit. From the model prediction and machining conditions, a target value of 80nm was set for the optimization. For the response, a range of weight values from 0.1 to 10 can be chosen to emphasize or de-emphasize the target. The significance of this value is such that:

I. Values less than 1(minimum is 0.1) assigns less emphasis on the target.
II. A weight of 1 places equal importance on the target and the bounds.
III. A value between 1 and 10 assigns huge emphasis on the target.

A weight of 10 was assigned to the target value. The optimization plot (Figure 4.9) from Minitab highlights 80nm is achievable with feed=1mm/min, depth=2μm and speed=15000nm. These values correspond to the lowest machining parameters obtainable from the design. The desirability value of 1 indicates the parameter combination achieves a favourable result. Their effects are shown in Figure 4.10.

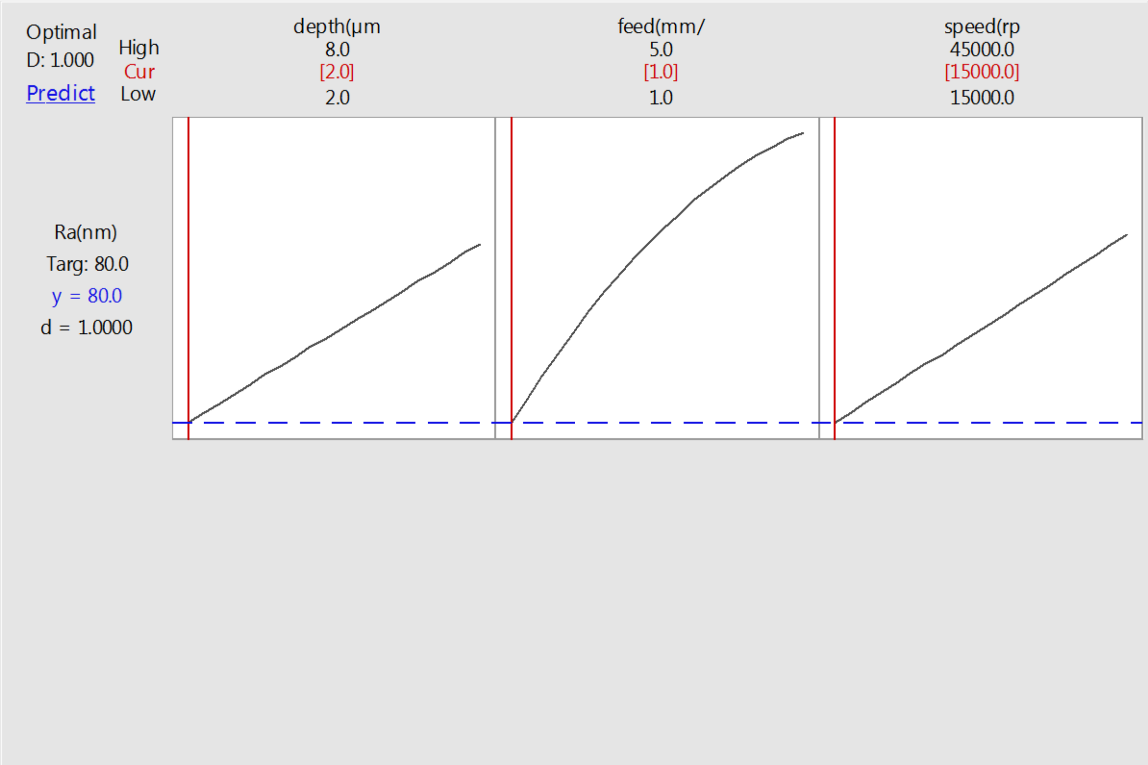

Figure 4.9: Optimization plot

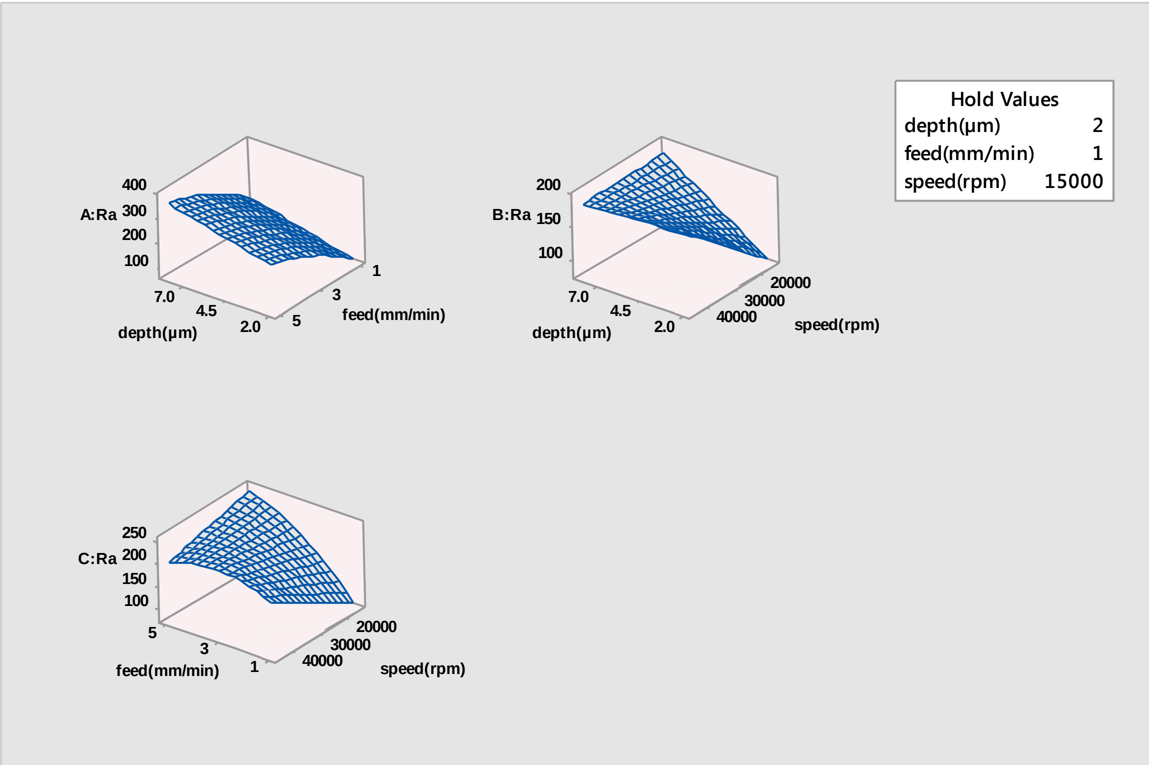

Figure 4.10: 3D optimised surface plot

4.2.6: Validation of model

The model F-value 35.53 infers the model is significant (Table 4.8). There is only a 0.01% chance that a model with an F-value this large could occur due to noise.

In order to further access the quality of a model, it is necessary to check the lack of fit to ensure that it is not significant. An insignificant lack of fit (F-value) falling within the range of 6.32 indicates that the data fit well in the model and implies there is a 14.29% chance that a 'lack of fit' value this large could occur due to noise. The Full ANOVA table at the appendix

It is also important to evaluate the coefficient of determination in R^2 and adjusted R^2. R^2 is a measure of the amount of in variability of a response using regression variables but its value can be artificially inflated by adding insignificant model terms hence R^2 is not a good statistical measure (78) . However, adjusted R^2adj is a better statistical measure of the amount of observed variability in the response because its value will only increase if the additional terms are statistically significant. For an ideal model, R^2adj should be greater than or equal to 70% (77).

The standard error of estimate(S) represents the standard deviation of the response value from the fitted values. The lower the S-value, the better the model describes the response. The predicted R^2 indicates how well the model predicts the response for new observations. It is a very useful tool in accessing a model since it is calculated with observations that are not included in the model calculation. A larger value gives a better predictive power. Also, a predicted R^2 value that is substantially less than R^2 may indicate that the model is over fit .

Table 4.7: Summary of regression analysis

S	R-square	R-square(adj)	Pred. R-square
12.9nm	96.4%	93.7%	82.9%

From the regression summary (Table 4.7) it is evident that the standard error of estimate is acceptable, R^2adj value indicates that the developed model explains 93.7% of the variation in the surface roughness response data. That is to say that 93.7% of the total variability in the surface roughness is explained by the independent variables of feed, speed and depth of cut. The value of predicted R^2 is also high enough and is not substantially less than R^2 therefore the model is not over fit but can be used to navigate the design space.

4.2.6.1: Analysis of variance

The significance of the model factors was carried out using analysis of variance (ANOVA). This is done to analyze statistically the relative significance of the model and the response and to further validate the model. The parameters in the ANOVA are calculated as:

$$Mean\ square = (sum\ of\ square)/(degree\ of\ freedom\ (df))$$

$$Fvalue = (respective\ mean\ square\ of\ a\ model\ and\ terms)/(residual\ mean\ square)$$

The mean square has been used to determine whether terms in the model are significant while the *F* -values are used to compare models and their terms with a residual variance.

The following applies to the ANOVA analysis in this research:

I. The null hypothesis (H_o) for the main effect is that the surface roughness means for all parameter factor levels are equal.
II. The null hypothesis (H_o) for an interaction effect is that the surface roughness means for the level of one factor does not depend on the level of the factor.
III. The statistical significance of the terms and effect depends on the assigned p-value of 0.05. A significant level of 0.05 indicates of 5% risk of concluding that an effect exists when there is no actual effect.

If the variances are similar in range, the ratio will be close to 1 and it is less likely that any of the factors have a significant effect on the response. Accordingly, a p-value of less than 0.05 indicates that the terms in the model have a significant effect in the surface roughness.

Table 4.8: Summary of ANOVA table

ANOVA					
	df	*SS*	*MS*	*F*	*Significance F*
Model	6	35452.97619	5908.829	35.53228934	0.000024
Residual	8	1330.357143	166.2946		
Total	14	36783.33333			

Table 4.8 shows the summary of ANOVA studies for the surface roughness model in this research the ANOVA table can be found in the appendix. The p-value of 0.000024 indicates that the model is extremely significant. The extended ANOVA table with the mean square error and the mean square model can be found in the appendix section.

From the plot residual plot of standardized residuals, the probability distribution indicates that no outliers are present in the fitted model and the fitted values are evenly distributed around the zero thresholds. This indicates the absence of patterns or correlation in the fitted model and the absence of homoscedasticity (Figure 4.11). The table of prediction indicates that the highest percentage error of prediction is 9.6% which is within the acceptable 25% for a model with 82.9% predicted R^2.

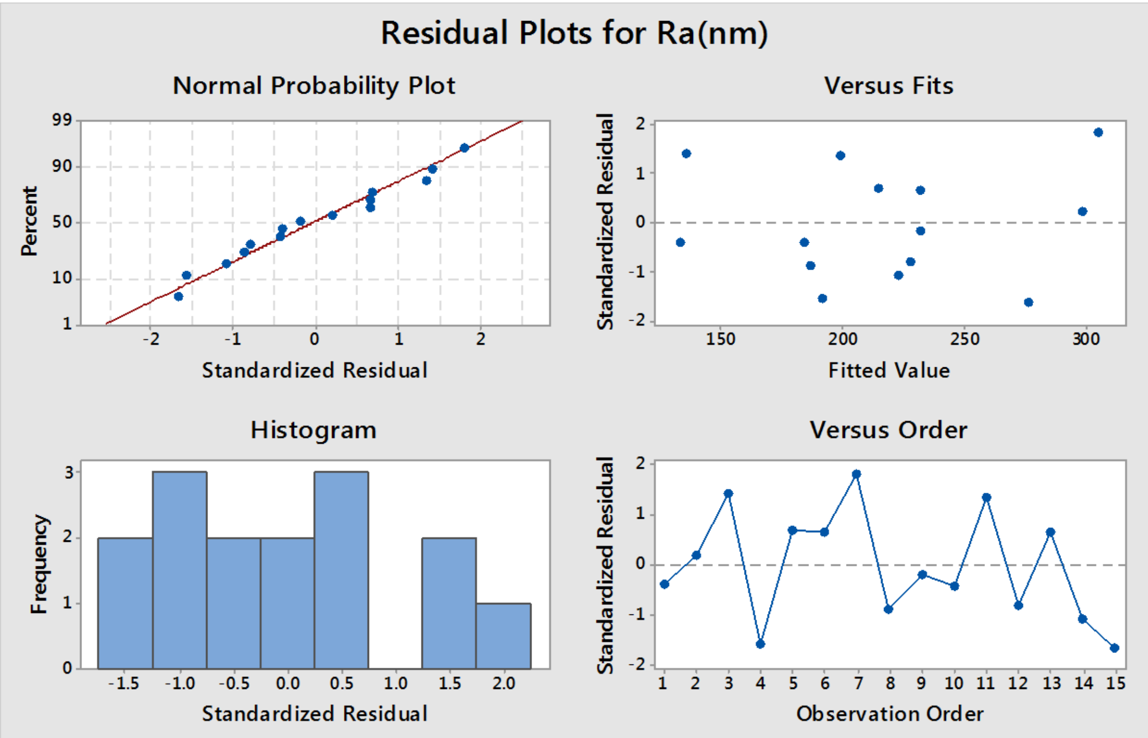

Figure 4.11: Residual plots for Ra

Table 4.9: Percentage error of predicted Ra

Run Order	Depth(um)	Feed(mm/min)	Speed(rpm)	Ra(nm)	Predicted(nm)	% error
1	5	1	15000	130	133	-2.4
2	8	3	15000	300	298	0.5
3	2	1	30000	150	136	9.6
4	2	3	15000	180	192	-6.7
5	8	3	45000	220	215	2.4
6	5	3	30000	240	232	3.3
7	5	5	15000	320	306	4.5
8	5	1	45000	180	187	-3.8
9	5	3	30000	230	232	-0.9
10	8	1	30000	180	184	-2.4
11	5	5	45000	210	199	5.1
12	2	5	30000	220	228	-3.7
13	5	3	30000	240	232	3.3
14	2	3	45000	215	223	-3.9
15	8	5	30000	260	277	-6.5

Table 4.9 highlights the predicted outcomes of surface roughness values from the developed response model.

4.3: AE SIGNAL ANALYSIS

Below is the summary of the process flow adopted for the signal processing, feature extraction and selection in this research using NI LabVIEW, Matlab, Statistica and Minitab (Fig 4.12). Acquired AE signals were electronically filtered through a band pass filter (50 kHz-1000 kHz) at the point of acquisition. This was able to eliminate machine vibration and environmental noise occurrence at low frequencies.

4.3.1 AE Data segmentation

A total of 270 million samples of AE data were acquired during the research at the rate of 2million samples per second (Table 4.10). With the use of Minitab software, the AE data was segmented into a time frame of 0.1s which corresponds to a length of 200000 samples per segment and one tenth of a sampling window as observed in (Table 4.11). The segmentation was necessary to check for consistency in AE data, reduce processing time and eliminate redundancy. As highlighted in section 3.10.2.1, AE data acquisition was carried out as the wheel progressed towards the center of the workpiece.

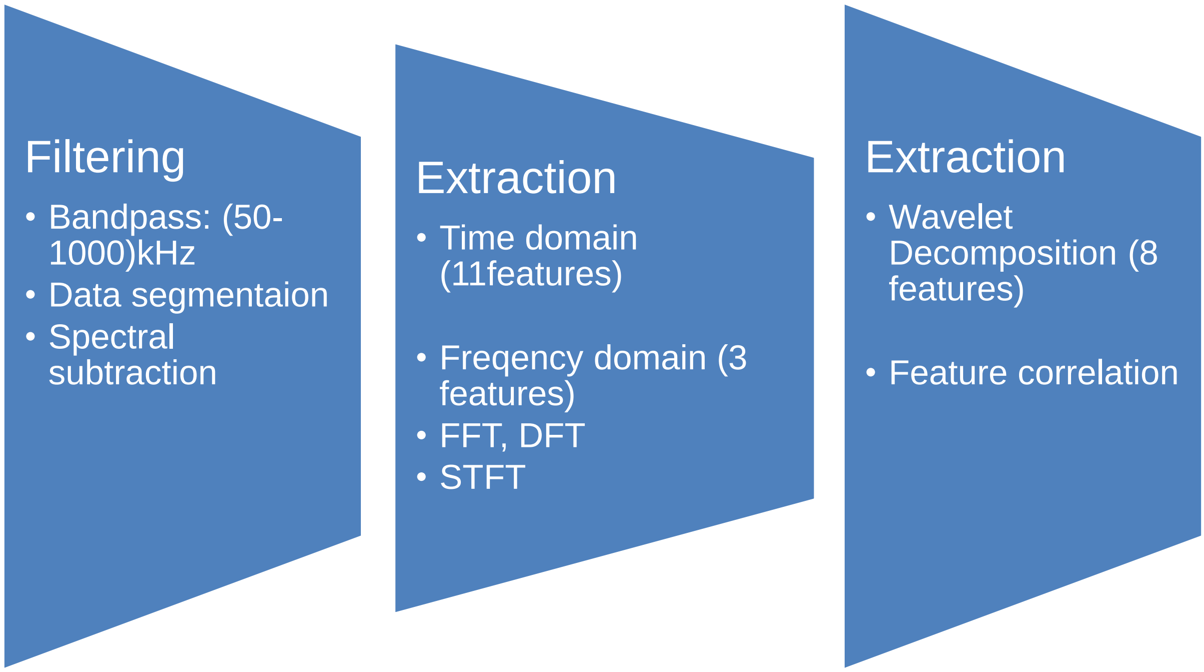

Figure 4.12: AE signal process summary

Table 4.10: Acquired AE samples

Experiment number	Number of AE samples in millions
1	18
2	14
3	12
4	12
5	20
6	20
7	6
8	34
9	16
10	22
11	20
12	20
13	18
14	24
15	14
TOTAL	270

Table 4.11: AE data segmentation

Wheel speed	15000rpm	30000rpm	45000rpm
Window segment length in seconds	0.1	0.1	0.1
Number of wheel revolutions per segment	25	50	75
Surface contact length for window segment	Varied according to feed rate		
Number of samples per segment	200000		
Sampling rate	2000000		

4.4: AE SIGNAL PROCESSING

Noise frequency effects were observed in the AE data. This could be due to the interference of the spindle resonant frequency with the AE data. The noise frequencies were observed to increase with an increase in speed ranging from 15000rpm to 45000 rpm. When viewed with a spectrogram the frequency was observed to coincide with the range of useful AE frequency all through the entire window segment in the research. The noise could be as a result of frequency harmonics present from the high-speed grinding and workpiece spindles (80). The harmonic frequencies were observed to vary with the spindle speed (Figure 4.13). Also, they were within the useful AE frequency range hence the use of a band filter may not be efficient in this circumstance. Spectral subtraction technique was applied.

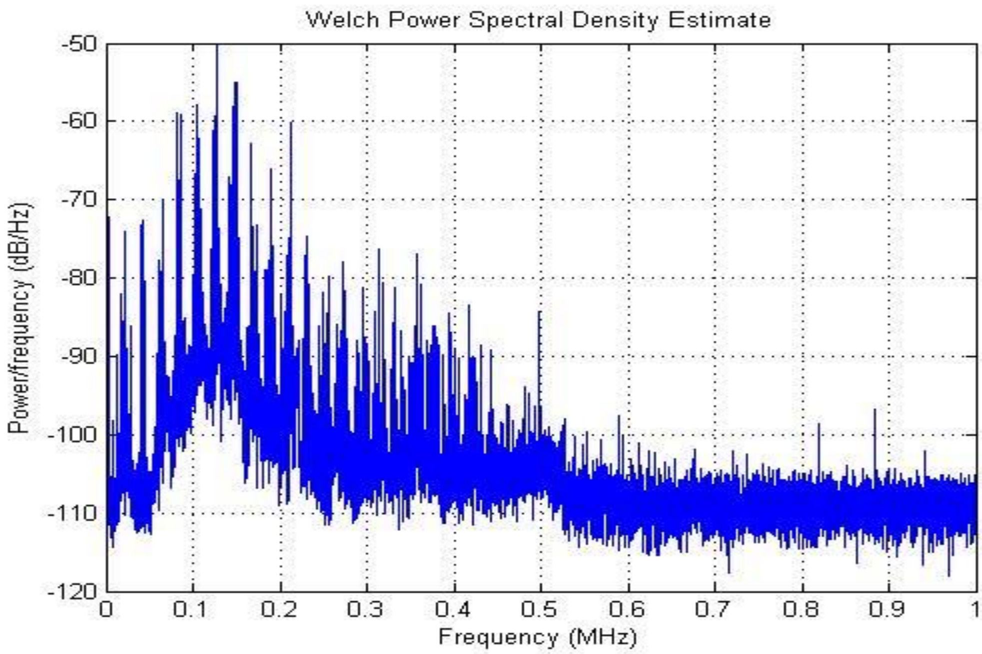

Figure 4.13: Spectral density estimates of spindle harmonics at 15000 rpm

4.4.1: Spectral subtraction technique

Steven Boll proposed a spectral subtraction method which is a computationally effective technique for noise reduction in signals and serves as a basis for reducing noise on the level of the frequency spectrum (81). This technique hinges on the homogeneity and additive property of the Fourier transform and is highly efficient where the frequency signature of the signal and noise are known (82). Spectral subtraction technique has proven to achieve a higher correlation coefficient of AE features compared to other methods like wavelet shrinkage in real time monitoring with AE.

As a benchmark to determine the reference noise, data sampling was carried out with spindle running at 15000, 30000, and 45000 rpm without any contact with the workpiece as indicated in section 3.10.2.1. These set of acquired noise data contained both spindle harmonic frequencies and other environmental noise influence which could not be thoroughly filtered. The subtraction process was done in three categories based on the wheel speed parameter value obtainable from the experimental design.

The set of equations below for the 15000 rpm noise data were applied to experiments 1, 2, 4 and 7 while the other experimental runs were subtracted according to respective noise data.

$x(t) = s(t) + n15000(t)$: Time domain

$X(J\tilde{\omega}) = S(J\tilde{\omega}) + N15000(J\tilde{\omega})$: Frequency spectrum

$S(J\tilde{\omega}) = ((X(J\tilde{\omega}) - N15000(J\tilde{\omega}))$: Spectral subtraction (residual)

$s(t) = \text{ifft}\ ((X(J\tilde{\omega}) - N15000(J\tilde{\omega}))$: Inverse Fourier Transform of the residual

The subtraction process was carried out on the experiment grouping with their unique wheel speed, by subtracting the appropriate noise data. In order to validate the effectiveness of the spectral subtraction process, feature extraction was carried out both the noisy data and the noiseless data. It turned out that the spectral subtraction improved the correlation coefficient of extracted features. This validation table can be found in the appendix.

4.5: SIGNAL ANALYSIS AND FEATURE EXTRACTION

The feature extraction process was carried out in three domains which are time domain analysis, frequency domain and time-frequency domain.

4.5.1: Time domain observations

The amplitude levels of the AE data was observed to vary with the different combination of machining parameters in the time domain. The following were observed:

I. The amplitude levels of the AE voltage signals were observed to change with the combined effects of speed, feed and depth of cut.
II. Burst AE signals were very noticeable at high speeds of 45000 rpm while lower speeds yielded continuous AE signals.
III. Some amplitude voltage of the raw AE signals increased with an increase surface roughness values but the trend was not consistent through all the acquired data for the experimental runs
IV. The RMS level of the acquired AE signals increased with an increase in the surface roughness values but the increasing trend was not consistent.

The amplitude levels of some raw AE signals were observed to increase with some of the surface roughness values and the corresponding variation in machining parameters (Figure 4.14). The peak to peak AE voltage values of the raw signal were also observed to increase with an increase in some surface roughness values. Table 4.12 shows some roughness values with the corresponding peak to peak voltage values.

The burst AE signals were as a result of the higher rate of AE events resulting in quick transients which create the inability to form continuous signals.

Table 4.12: Peak to peak voltage and surface roughness

Ra(nm)	130	180	210	215
Range(V)	0.52	0.79	0.91	0.95

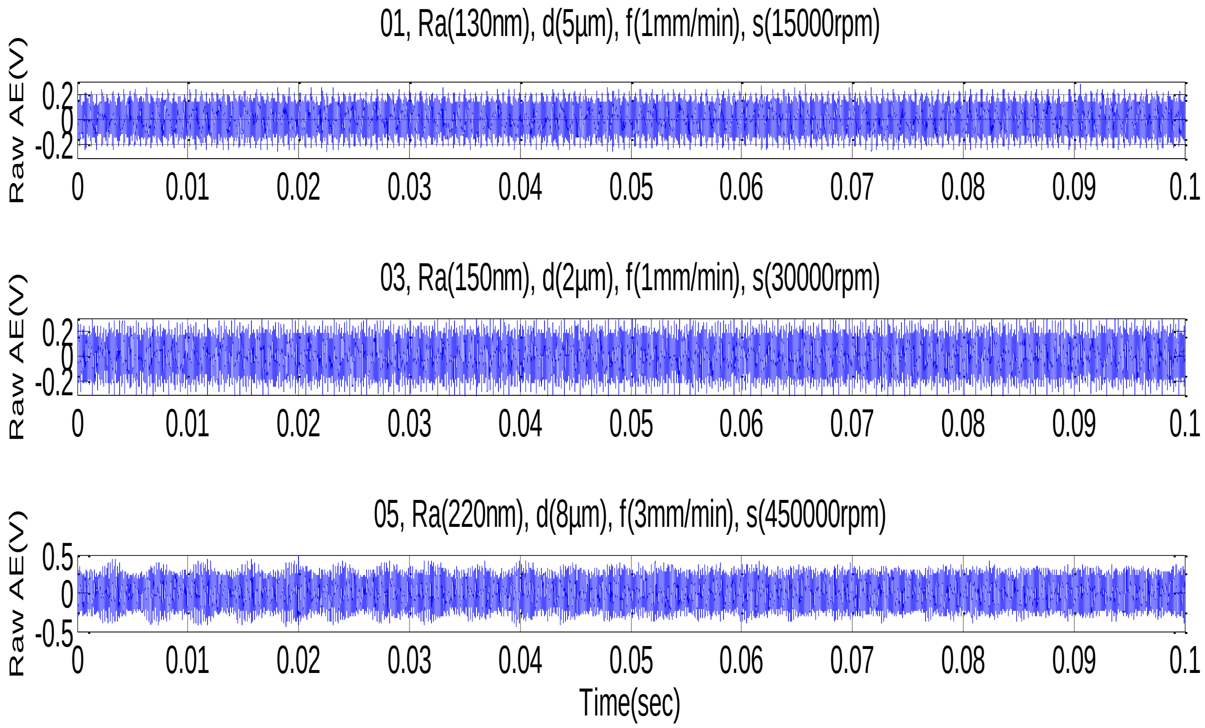

Figure 4.14: AE amplitude variations in time series

Figure 4.15 shows a complete cycle of some RMS AE signals. The RMS levels also increased with an increase in some surface roughness values with the highest RMS peak observed at 300nm (Figure 4.15).

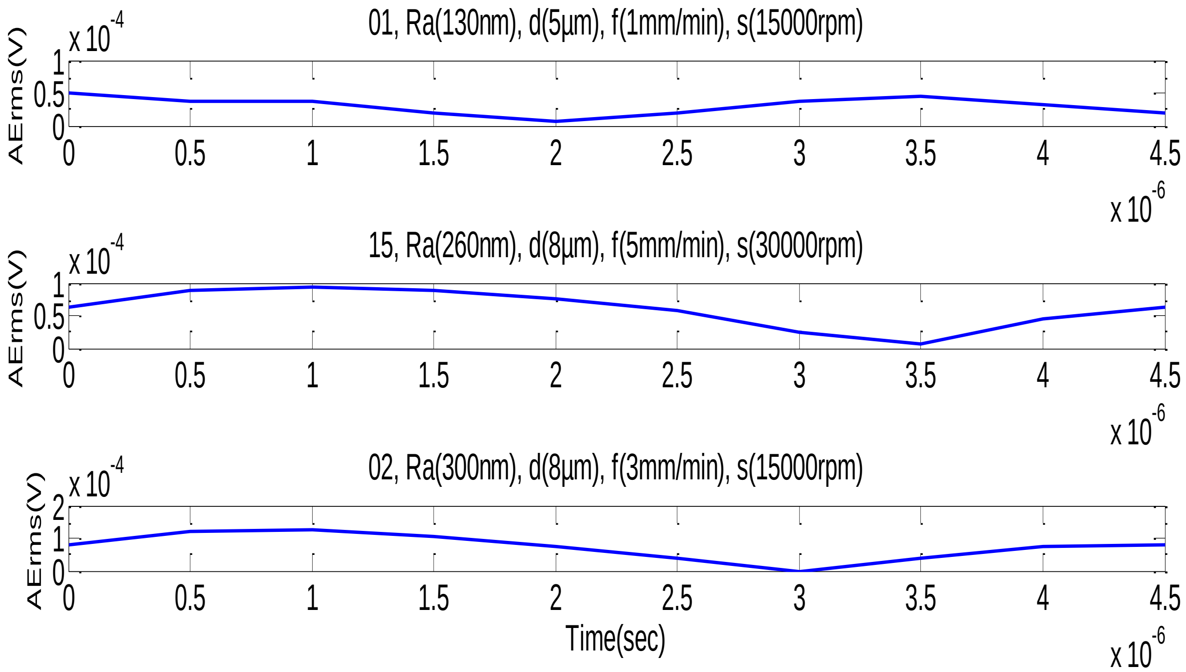

Figure 4.15: RMS Level of AE signals

The effect of increased speed and feed showed the presence of burst AE signals in the time domain.This is due to a higher rate of AE events at high speeds resulting to transients which create the inability to form continuous signals. This could be due to the fact that at high feed and speed, AE events increase but reduced cutting depth makes it easier to exit the surface faster as the bursts become more spaced out (Figure 4.16.)

Hence, it is suggested that for real-time monitoring, burst AE signals signify average to poor surface roughness conditions due to the occurrence of transients at medium to a high combination of machining parameters. While steady AE signals are sometimes indicators of good surface finishes. However raw AE amplitude levels are not sufficient for monitoring surface roughness in ultra-high precision grinding of Bk7 glass.

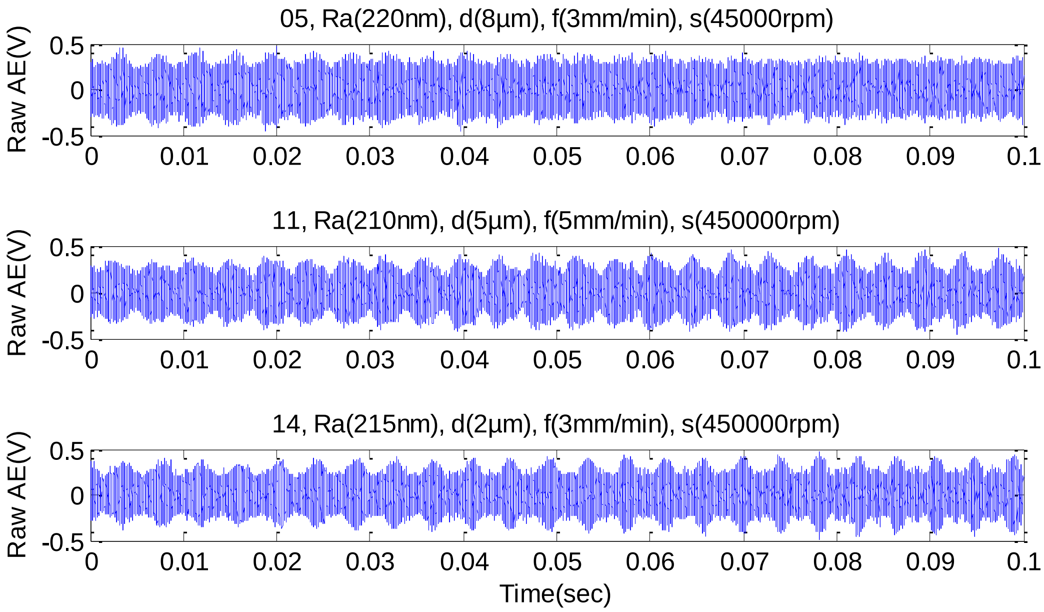

Figure 4.16: Burst AE signals

4.5.1.1: Time domain feature extraction

The following time series features were extracted from the AE data: AE mean, root mean square, skewness, kurtosis, crest factor, peak amplitude, peak to peak voltage, standard deviation, variation, minimum amplitude values.

4.5.2: Frequency domain observation

Fast Fourier Transforms (FFT) and Short Time Fourier Transforms (STFT) were employed to observe and analyze the spectral contents of the AE data in the frequency domain. Power spectral density was applied to investigate the nature of the frequency spectrum and where the frequencies are concentrated.

The AE data was observed to have similar fundamental frequencies and varying harmonics between 0.05 to 0.6MHz frequency bands (Figure 4.17 and 4.18).These harmonics varied with the machining parameters and surface roughness data and contain relevant information about the energy content in the frequency spectrum of the AE data.

The spectrograms (Figure 4.19 and Figure 4.20) revealed that at low speeds, feed and depth, the harmonics are concentrated within 100 kHz-200 kHz while variations are noticed between 300 kHz-400 kHz frequency range. These variations were observed to be dependent on the changes in machining parameters and surface roughness. The higher surface roughness values reflected higher harmonics which are in the magnitude range of -80dB to -70dB. More harmonics were observed between 300 kHz-500 kHz at higher surface roughness values of 300nm (Figure 4.20).

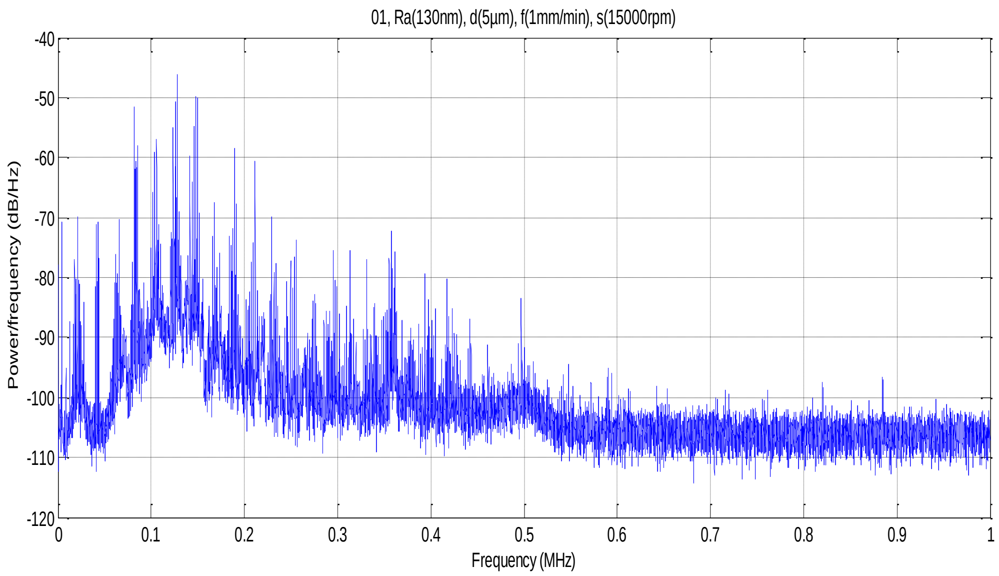

Figure 4.17: Power spectral density plot at 130nm

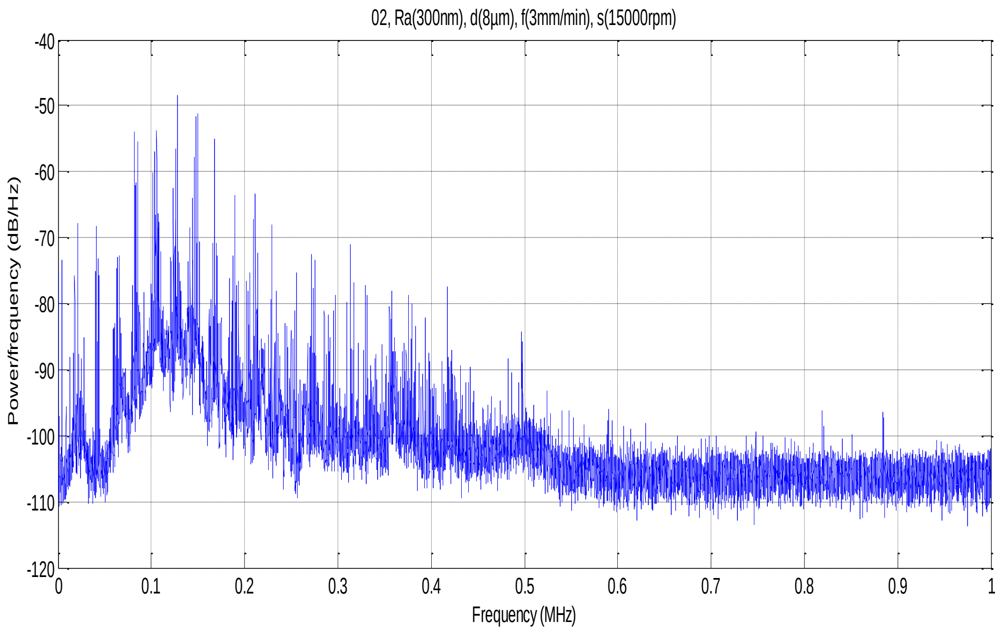

Figure 4.18: Power spectral density plot at 300nm

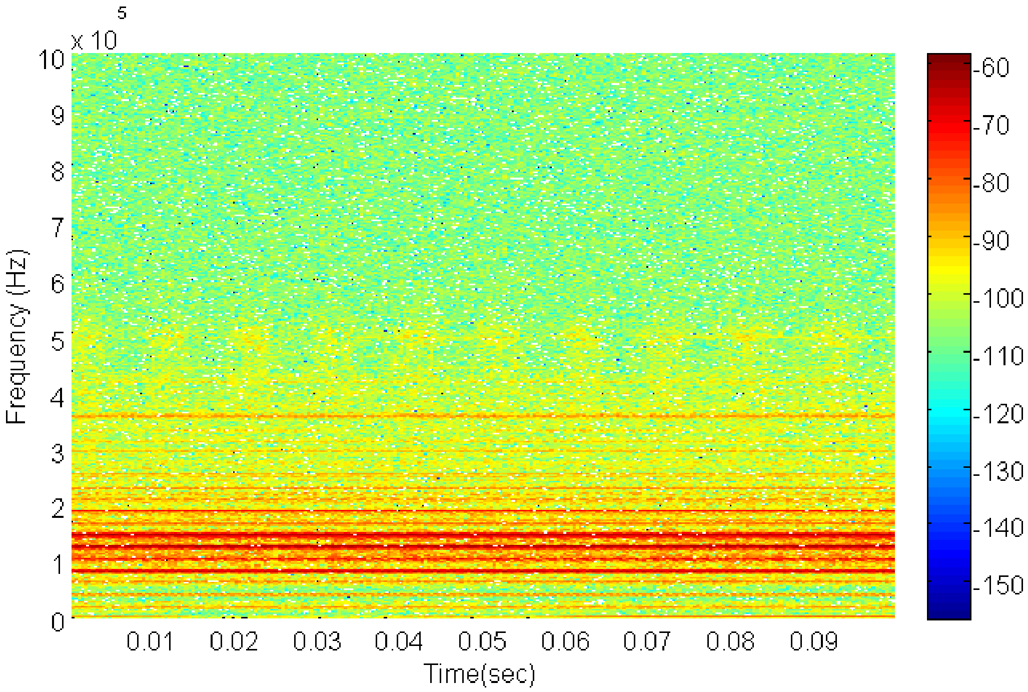

Figure 4.19: Spectrogram at 130nm

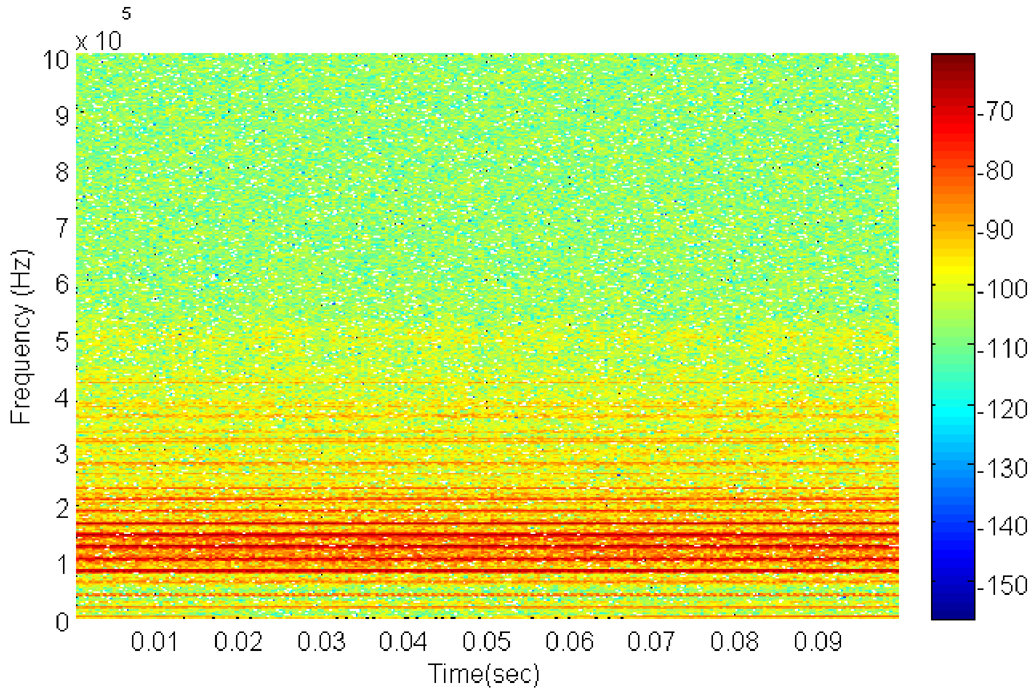

Figure 4.20: Spectrogram at 300nm

The following frequency domain features were extracted:

I. Mean frequency: A pitch measure that accesses the center of power distribution across the frequencies.

II. Spectral peaks: The maximum energy in the frequency spectrum.

III. Frequency deviation: The deviation of the frequency components from the mean frequency.

The frequency components of the acoustic signal showed a better variation with the surface roughness values compared to the amplitude levels of the raw AE signals. Hence raw AE amplitudes may not be best suited for monitoring the ultra-high precision grinding of BK7 glass.

4.5.3: Wavelet decomposition

Time-Frequency localization is advantageous because it is possible to vary the time-frequency aspect ratio in order to produce good frequency localization at low frequencies with a long time window and good time localization at high frequencies with short time windows thereby resulting in segmentation or tiling that is suitable for signals with transient nature like acoustics (83).

There are several “mother wavelets”. The Haar wavelet is very simple but a serious disadvantage is that it is not continuous. Ingrid Daubechies set of orthonormal basis function have proven to be elegant and has become the cornerstone for modern wavelet applications (84).

Debauchies discrete wavelet transform db3 is utilized for the decomposition analysis in this research. The wavelet decomposition technique was used to decompose the signal into several details hence giving a final approximation segmentation of the signal into different bandwidth for the frequency observation.

Base wavelet db3 with 7 levels was used for the wavelet features extraction in this research. Figure 4.21 shows that the sub-band d3 had the highest amplitude, followed by d4.This implied that majority of the AE spectral contents for the wavelets are centered within the frequency range of 125 kHz-250 kHz and 62.5 kHz-125 kHz respectively (Table 4.13). A vivid correlation was also observed with variations in sub-bands d2, d3, d4, d5 and the surface roughness.

The following features were extracted from the wavelet decomposition:

I. Frequency distribution in each sub-band.
II. Mean absolute value of coefficients in each sub-band.
III. The average power of wavelets in each sub-band.
IV. Total energy in sub-bands
V. Frequency deviation in each sub-band.

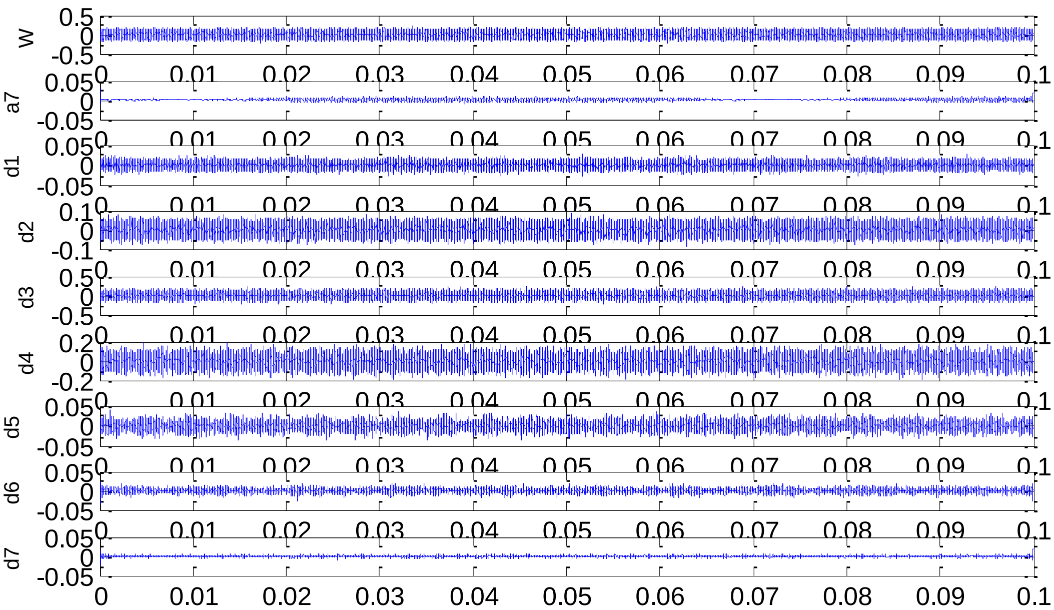

Figure 4.21: Wavelet decomposition at level 7

Table 4.13: Wavelet decomposition frequency levels

Decomposition level	Frequency Band
D1	500kHz-1MHz
D2	250kHz-500kHz
D3	125kHz-250kHz
D4	62.5kHz-125kHz
D5	31.25kHz-62.5kHz
D6	15.625kHz-31.25kHz
D7	7812.5Hz-15.625kHz
A8	0-7812.5Hz

A total of 22 features were extracted from the time, frequency and time-frequency domains. The extracted features were observed to vary in an ill- pattern across the generated surface roughness values. Figure 4.22 shows the ill-pattern variation of some extracted features with the surface roughness including standard deviation (std), total energy in sub-band (et), mean absolute frequency in sub-band 3 (f3), mean absolute frequency in sub-band 4 (f4), standard deviation of frequency in sub-band 3 (s3) and peak to peak time series voltage (p-p). The values in Figure 4.22 have been scaled to avoid superimposition of legends.

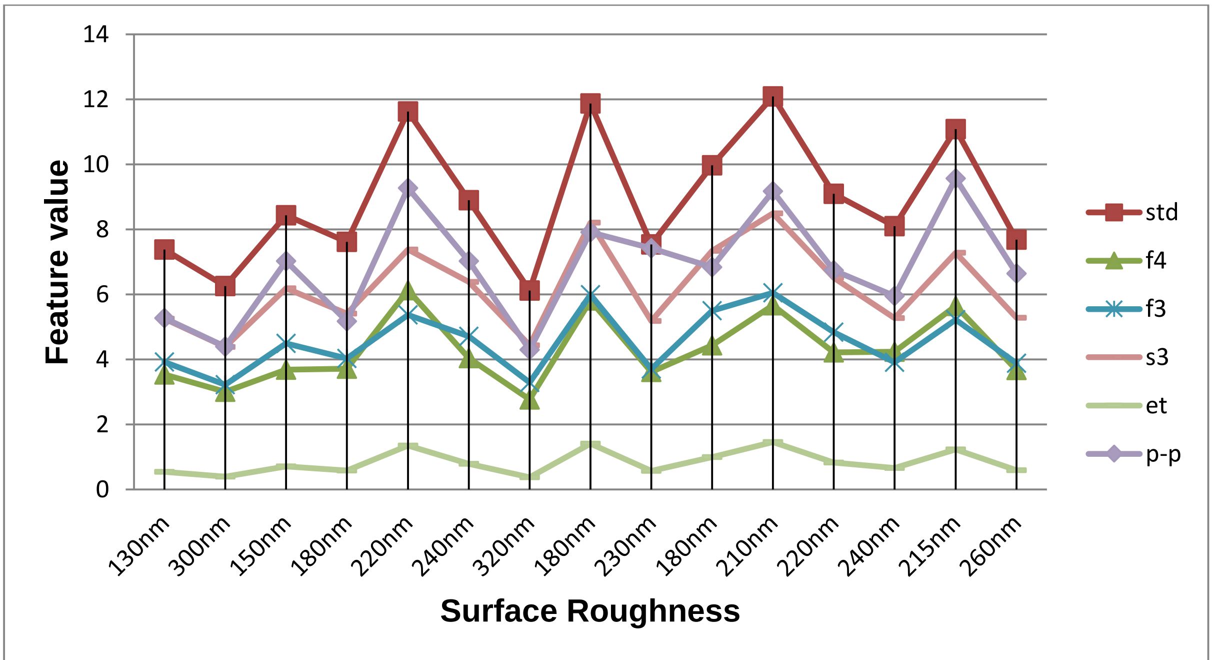

Figure 4.22: Variation of some extracted features with surface roughness

4.6: FEATURE SELECTION

A total of 22 features were extracted from the time and time-frequency domain. To determine the optimal feature sets to be used as input to neural network training, the correlation coefficient was implemented.

$$r = \frac{cov(Target, Output)}{\sigma target \sigma output} \ldots\ldots\ldots\ldots\ldots\ldots\ldots\ldots\ldots\ldots\ldots\ldots\ldots\ldots\ldots 4.7$$

Where:

$cov(Target, Output)$: Covariance of surface roughness and feature and

$\sigma target \sigma output$: Standard deviation of target and output.

Pearson's correlation (r) is normally used as a test of linear correlation between variables. A value of 1 represents a perfect positive linear relationship, 0 no correlation and -1 represents a perfect negative linear relationship. Table 4.14 shows the correlation coefficient of some extracted features in the research, including the coefficients of the machining parameters.

The coefficient value of 0.7 for feed supports the developed response surface model in section 4.2, which indicates that the feed influence is highest but not totally linear. Other coefficient values of 0.4 and -0.2 for depth and speed respectively also support the previous findings from the response surface model, indicating that the influence of cutting depth on the surface roughness is higher than the influence of speed.

The highest extracted feature value of 0.5 is the mean absolute value of the frequency (f3) in sub-band d3 in the time-frequency domain and the standard deviation -0.4 in the time domain. This indicates that a relationship exists between the extracted features and the surface roughness but none of the relationships are perfectly linear (Figure 4.22). Neural networks models are well suited for investigating such non-linear relationships.

Table 4.14: Correlation coefficient

Feature	R
Feed	0.7
Speed	-0.2
Depth	0.4
RMS	-0.4
F3 (mean absolute value in sub band 3)	-0.5
F4 (mean absolute value in sub-band 4)	-0.3
F9 (ratio of mean value in bands 3 and 4)	-0.1
F10(ratio of mean value in bands 2 and 5)	0.1
E3 (energy in sub-band 3)	-0.4
E4 (energy in sub-band 4)	-0.3
Et (total energy in sub-bands)	-0.3
S3 (standard deviation of frequency sub-band 3)	-0.4
S4 (standard deviation of frequency in sub-band 4)	-0.3

4.7: NEURAL NETWORK

A total 10 feature sets were selected for building the neural network, based on correlation coefficients and literature, including the machining parameters, mean, root mean square and standard deviation, frequency content and deviations in sub-band d3, d4and the total energy of wavelets.

4.7.1: Transformation of data set

The selected feature dataset was transformed to values ranging between 0 and 1 using equation 4.8 where 0 and 1 value correspond to the lowest and highest feature value in the subset respectively (Table 4.15). The transformation was done to achieve standardization of the feature values and reduce redundancy before feeding them into the network for training.

$$Yt = (Yo - Ymin)/(Ymax - Ymin) \quad \ldots\ldots\ldots\ldots\ldots\ldots\ldots\ldots\ldots\ldots\ldots\ldots \; 4.8$$

Where:

Yt - Transformed value of Yo, Yo - observed value, $Ymax$ – maximum observed value in the subset and $Ymin$ – minimum observed value in the subset.

Table 4.15: Transformation of some feature subsets

	Ra	Ra(t)	Feed	Feed(t)	Rms	Rms(t)
1	130	0	1	0	0.07	0.21
2	300	0.89	3	0.5	0.06	0.02
3	150	0.11	1	0	0.08	0.39
4	180	0.26	3	0.5	0.07	0.25
5	220	0.47	3	0.5	0.12	0.92
6	240	0.58	3	0.5	0.09	0.46
7	320	1	5	1	0.06	0
8	180	0.26	1	0	0.12	0.96
9	230	0.53	3	0.5	0.07	0.24
10	180	0.26	1	0	0.10	0.64
11	210	0.42	5	1	0.12	1
12	220	0.47	5	1	0.09	0.50
13	240	0.58	3	0.5	0.08	0.33
14	215	0.45	3	0.5	0.11	0.83
15	260	0.68	5	1	0.07	0.26

4.7.2: Neural Network Architecture

A three layer feed forward BPNN with one hidden layer was adopted to train the network for the classification process. The network architecture comprises 10 input neurons, 20 hidden layer neurons and a single output (Table 4.16).

The transfer function for the individual layers is log sigmoid (equation 4.9). Log-sigmoid activation function can only generate output values between 0 and 1 hence it was selected because it is suitable for the transformed data pattern.

$$f(x) = \frac{1}{1 + \exp(-x)} \quad \ldots \ldots \ldots \ldots \ldots \ldots \ldots \ldots \ldots \ldots \ldots \ldots \ldots \ldots \ldots \ldots \ldots \ldots \ldots \ldots \ldots \ldots \ldots \ldots \ldots \ldots \; 4.9$$

Table 4.16: Network model and architecture

Parameters	Values
Maximum iterations	500000
Number of layers	3
Transfer function at layer 1	Log-sigmoid
Transfer function at layer 2	Log-sigmoid
Transfer function at layer 3	Log-sigmoid
Layer 1 size	10
Layer 2 size	20
Layer 3 size	1
Learning rate	0.1-0.9
Momentum	0.1-0.9
Weights	Random from [-1,1]
Training function	Gradient descent
Training method	Batch process

4.7.3: Training and Prediction

Training of the network was done programmatically with SQL on SAPHANA platform. SAPHANA is robust software capable of handling a huge amount of data and has been successfully applied in extremely large sets of data including financial data. The developed codes for training and testing can be viewed at the appendix section. The transformed data set was divided into two categories for training and testing. Ten data sets (experiment: 1-10) were selected for training while five data sets (experiment: 11-15) were selected for network testing and prediction.

Several simultaneous training and prediction tests were carried out to determine the optimum function by varying the learning rate and the momentum function. The goal for training is to predict at least an accurate single value within the prediction data set while maintaining a low mean square error value generally. In all the combination of learning rates and momentum function for the five prediction data sets, experiment 14 (215nm) showed the closest prediction accuracy in all the tests therefore this value was used as the benchmark for the best training condition and subsequent prediction.

Different combinations of momentum function and learning rate resulted in different prediction accuracies for the target value of 215nm (Table 4.17). The highest prediction accuracy for a single value of 215nm occurred at learning rate of 0.1 and momentum function of 0.2 (Table 4.18) while the lowest mean square error occurred at learning rate of 0.3 and momentum function 0.1 (Table 4.17).

Figure 4.23 and Figure 4.24 show a training and prediction process in SAPHANA with the mean square error, training speed, server runtime and some SQL codes.

The selected training condition was successfully achieved in 193ms and 55 µs with a server processing time of 2ms and 794µs and a maximum iteration of 50000 epochs. Table 4.17 also shows a comparison of the highest prediction accuracy for 215nm for different training conditions with some of the different learning rates, momentum function and mean square error values observed while training the BPNN neural network. Table 4.18 shows a prediction set (experiment 11- 14) from the selected training condition (at learning rate 0.1 and momentum function 0.2) with transformed values of the response and their respective conversions.

Table 4.17: Comparison of predicted values for experiment 14 (215nm)

Learning rate	Momentum function	Response	(Response*(320-130))+ 130nm	Error
0.3	0.1	0.51052	227	1.1×10^{-8}
0.8	0.5	0.34736	196	1.7×10^{-4}
0.8	0.1	0.51052	227	2.7×10^{-6}
0.1	0.8	0.21052	177	7.4×10^{-6}
0.1	0.1	0.50966	226	3.8×10^{-6}
0.1	0.2	0.44976	215	1.1×10^{-4}
0.2	0.2	0.42631	211	1.1×10^{-4}
0.2	0.1	0.51052	227	2.4×10^{-7}

Table 4.18: Neural network prediction set (Experiment 11- 15)

ID	Response	Predicted =(Response*(320-130))+ 130nm	Actual (nm)	Accuracy (%)
11	0.74025	270.65	210	78
12	0.79421	280.90	220	79
13	0.46691	218.71	240	91
14	0.44976	215.45	215	100
15	0.99250	318.57	260	82

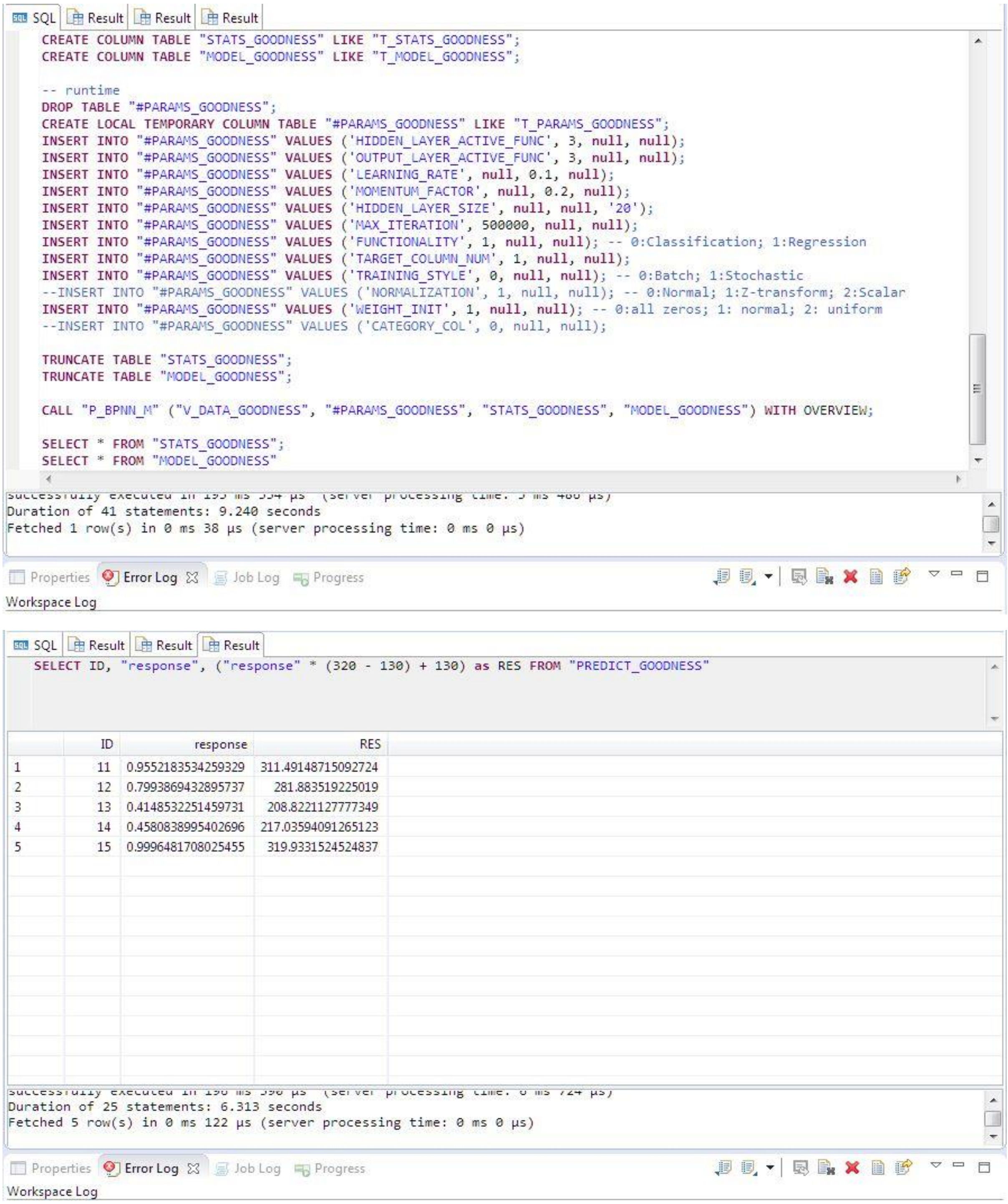

Figure 4.23: ANN training and prediction with SAPHANA platform

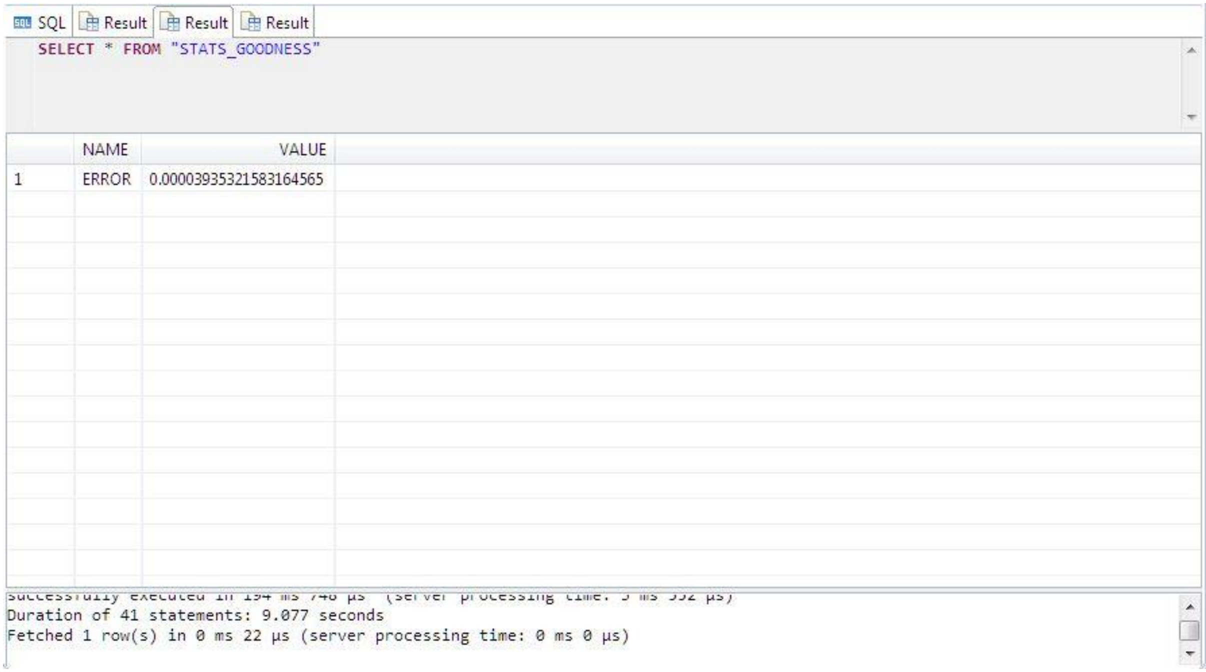

Figure 4.24: Mean square error

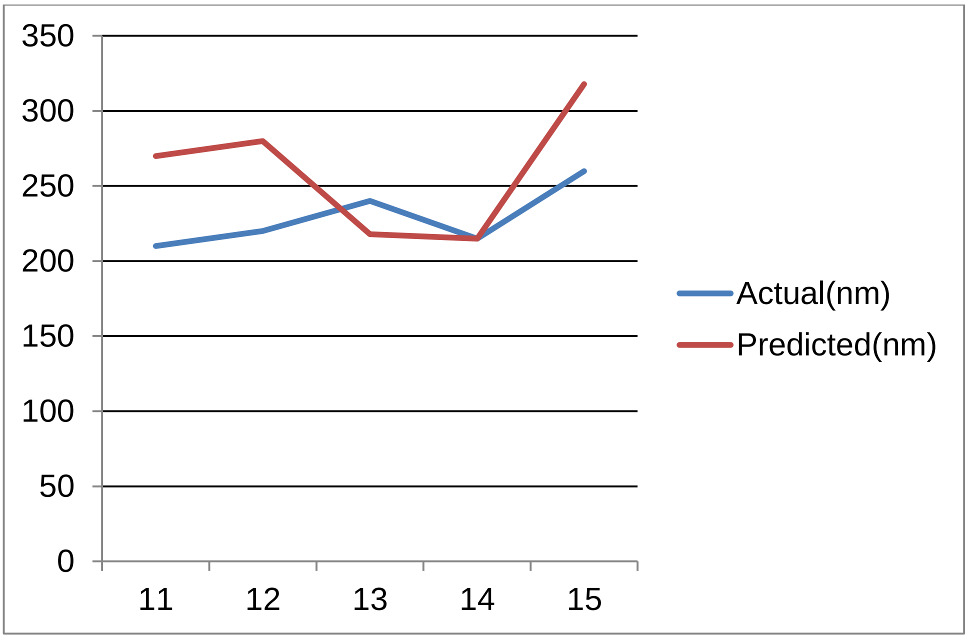

Figure 4.25: Actual and predicted values for the selected learning rate and momentum factor (training condition)

A variation of the predicted values with the original experimental values for the selected training condition indicates a close margin of prediction for 240nm and 215nm (experiment 13 and 14) (Figure 4.25). Wider variations were observed for the remaining prediction data set with the lowest occurring at 210nm value (experiment 11). This suggests that the developed network can be improved with further tests.

Figure 4.26 shows the structure of the developed neural network with 10 input neurons, 20 hidden layer neurons and a single output neuron.

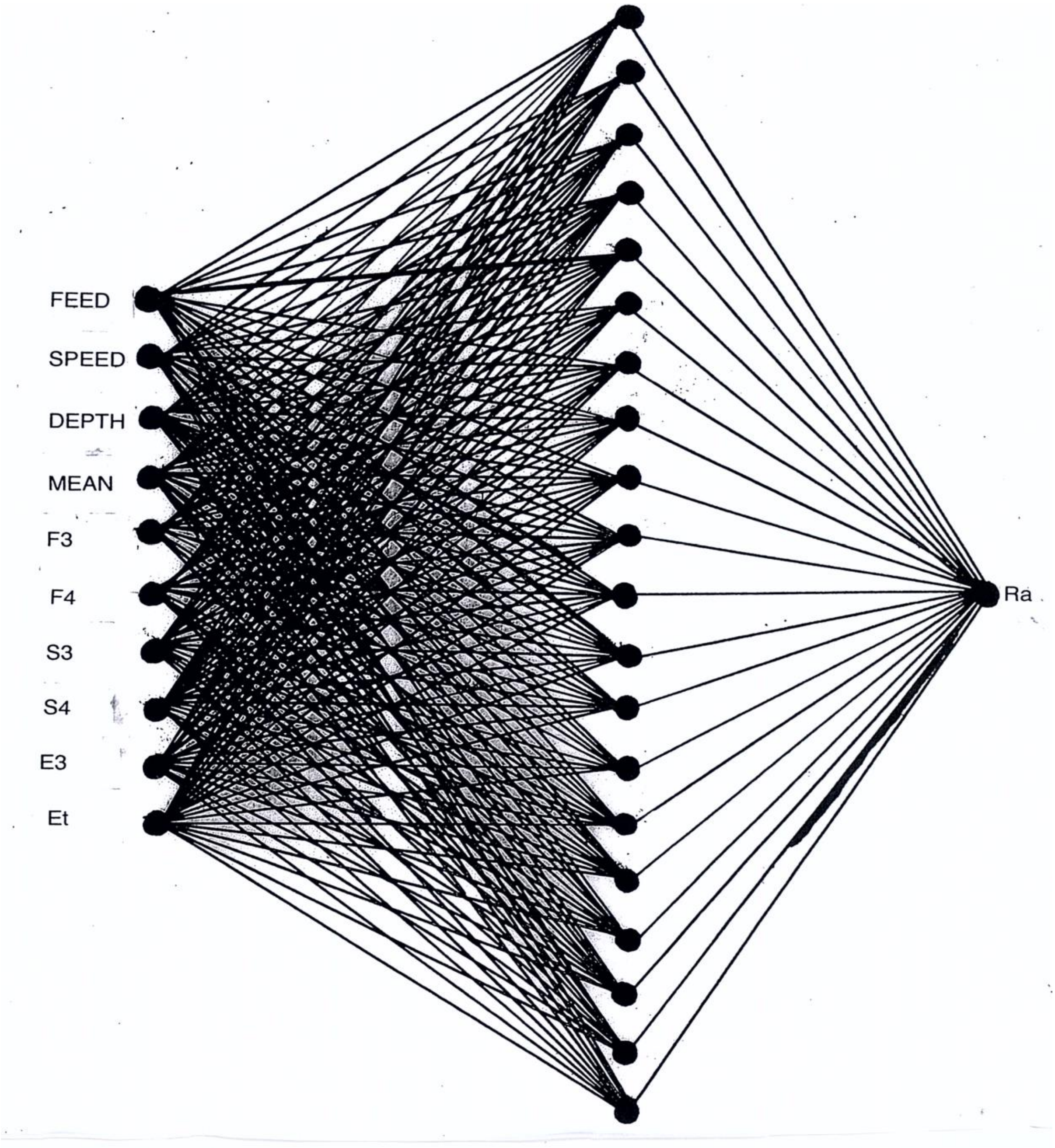

Figure 4.26: Network structure

The proposed neural network model structure can be found in the equations below.

$$G = F(f_n - f_{n-1}, d_n - d_{n-1}, s_n - s_{n-1}, et_n - et_{n-1}, f3_n - f3_{n-1}, s3_n - s3_{n-1}, r_n - r_{n-1}, f4_n - f4_{n-1}, m_n - m_{n-1}, e3_n - e3_{n-1})$$

$$Ra = \frac{1}{1 + \exp G}$$

The terms n and n-1 represent the transformed value of the nth iteration and the previous iteration respectively where:

m = mean (time domain)

r =root mean square (time domain)

f = feed

s = speed

d = depth

f3 = mean absolute value of frequency in sub-band 3(wavelet)

f4 = absolute value of frequency in sub-band 4(wavelet)

et = total energy in sub-bands (wavelet)

s3 = standard deviation of frequency components in sub-band 3(wavelet)

e3 = total energy in sub-band 3 (wavelet)

Chapter 5
Conclusion and Recommendation

5.1: CONCLUSION

Through the careful selection of machining parameters and efficient design of the experiment, SPIA has been applied to the ultra-high precision grinding of BK7 optical glass and the grinding process has been monitored using acoustic emission sensing technique. A quadratic model has been developed using response surface methodology while neural network prediction has been applied to the extracted AE signal features, therefore, we reject the null hypothesis in section 1.7. The study exposed some important results in ultra-high precision grinding of BK7 glass which include:

I. SPIA configuration is able to prevent wheel loading and rubbing from occurring by ensuring easy chip removal from the surface of the wheel.
II. The developed response model is able to predict 93.7% of the total variability in the surface roughness.
III. The feed rate has the highest effect on the surface roughness.
IV. A minimum surface roughness value of 80nm has been achieved through optimization at low values of feed, speed and depth of cut. Hence, better surface finishes can be achieved by using lower machining parameters.
V. At high feed and cutting depth, it is possible to improve the surface roughness by increasing the wheel speed.
VI. The amplitudes of the raw AE voltage do not follow a consistent increasing trend with the increase in surface roughness values therefore, they may not be suitable for online monitoring.
VII. It is possible to initiate online monitoring by analyzing the real-time burst AE signals in the time domain.
VIII. Time-frequency domain features (wavelets) show a better correlation with the surface roughness compared to time domain features and frequency domain features. Therefore, they serve as a better choice of input to the neural network scheme.
IX. The overall extracted AE features show a unique ill- pattern with the changes in surface roughness values.

X. The extracted wavelet features from sub-bands 3 and 4 show the most significant correlation with surface roughness compared to other sub-bands. Hence, they are more suitable features for predicting the surface roughness.
XI. Artificial Neural Network models are suitable in predicting such ill-pattern variations derived from the study by achieving a hundred percent prediction accuracy for 215nm value.

5.2: RECOMMENDATION

Some recommendations have been suggested during this study. These include:

I. The use of microscopy evaluation to observe the surface metrology in the form of ductile streaks and direction of lay.
II. Initiation of further study on subsurface damage that may have occurred
III. Extending the study to other important surface roughness parameters like maximum peak to valley height.
IV. The use of wireless AE sensor to acquire signals from a point closer to the workpiece and an AE sensor with a wider frequency range.
V. Implementation of electronic counters to measure the AE ring down count rate and constant false alarm rate (CFAR).
VI. Possible investigations of the wheel wear over time to determine its relationship with the surface roughness and AE data.
VII. The implementation of a wider processing time-window frame for AE signal processing

REFERENCE LIST

1. M M, B H. Article on Borosilicate glass [online] [cited 2014 May 27]. Available from: http://www.wisegeek.org/what-is-borosilicate-glass.htm#didyouknowout.
2. CIDRA precision services LLC [online] [cited 2014 17 May]. Available from: http://www.cidraprecisionservices.com/precisions-services-glass-bk7.html
3. Prazisions Glas and Optik [online]

[cited 2014 15 May]. Available from: www.pgo-online.com/intl/katalog/Bk7.html
4. Lv D, Huang Y, Wang H, Tang Y, Wu X. Improvement effects of vibration on cutting force in rotary ultrasonic machining of BK7. Journal of Materials Processing Technology. 2013;213:1548-57.
5. Kumar AS, Lim H, Rahman M, Fathima K. A study on the grinding of glass using electrolytic in-process dressing. Journal of electronic materials. 2002;31(10):1039-46.
6. F M. Encapsulating smaller and smarter implantables is a glass act [online] 2014. Available from: http://medicaldesign.com/materials/encapsulating-smaller-and-smarter-implantables-glass-act
7. Perveen A, Jahan M, Rahman M, Wong Y. A study on microgrinding of brittle and difficult-to-cut glasses using on-machine fabricated poly crystalline diamond (PCD) tool. Journal of Materials Processing Technology. 2012;212(3):580-93.
8. Heinzel C, Rickens K. Engineered wheels for grinding of optical glass. CIRP Annals - Manufacturing Technology. 2009 //;58(1):315-8.
9. Sun X, Stephenson DJ, Ohnishi O, Baldwin A. An investigation into parallel and cross grinding of BK7 glass. Precision Engineering. 2006 4//;30(2):145-53.
10. Brinksmeier E, Mutlugünes Y, Klocke F, Aurich J, Shore P, Ohmori H. Ultra-precision grinding. CIRP Annals-Manufacturing Technology. 2010;59(2):652-71.
11. Jackson MJ. Microfabrication and Nanomanufacturing. 1st Edition ed: CRC Press Taylor & Francis Group 6000 Broken Sound Parkway NW, Suite 300 ,Boca Raton, FL 33487-2742; 2006 2015/10/15. 80,1 p.
12. Nakazawa H. Principles of Precision Engineering. USA: Oxford University Press, USA; 1994. November 24, 1994.
13. V C Venkatesh SI. Presicion Engineering: TaTa Mc Graw-Hill Publishing Compoany Limited, New Delhi; 2007.
14. Taniguchi N. Current status in and future trends of ultra precision machining and ultra-fine processing. Annals of the CIRP, 1983, Vol 32, No 2, 573–582. Vol. 32(No. 2): 573–82.
15. Brinksmeier E, Preuss W. Micro-machining. Philosophical Transactions of the Royal Society of London A: Mathematical, Physical and Engineering Sciences. 2012 2012-08-28 00:00:00;370(1973):3973-92.
16. Schulz. H, and Moriwaki, T., . High speed machining Ann CIRP, 41, . 1992;41:637-43.
17. Venkatesh VC, Sudin I. PRECISION ENGINEERING. Precision Engineering: McGraw Hill Professional, Access Engineering; 2007.
18. Bifano TG, Dow TA, Scattergood RO. Ductile-Regime Grinding: A New Technology for Machining Brittle Materials. Journal of Engineering for Industry. 1991;113(2):184-9.
19. Gu W, Yao Z, Li H. Investigation of grinding modes in horizontal surface grinding of optical glass BK7. Journal of materials processing technology. 2011;211(10):1629-36.

20. Blake PN, Scattergood RO. Ductile-Regime Machining of Germanium and Silicon. Journal of the American ceramic society. 1990;73(4):949-57.
21. Venkatesh VC, Sudin I. MECHANICS OF MATERIALS CUTTING. Precision Engineering: McGraw Hill Professional, Access Engineering; 2007.
22. Blackley WS, Scattergood RO. Ductile-regime machining model for diamond turning of brittle materials. Precision Engineering. 1991 4//;13(2):95-103.
23. Bifano TG, Dow T, Scattergood R. Ductile-regime grinding: a new technology for machining brittle materials. Journal of Manufacturing Science and Engineering. 1991;113(2):184-9.
24. Fathima K, Senthil Kumar A, Rahman M, Lim HS. A study on wear mechanism and wear reduction strategies in grinding wheels used for ELID grinding. Wear. 2003 11//;254(12):1247-55.
25. Chen M, Zhao Q, Dong S, Li D. The critical conditions of brittle–ductile transition and the factors influencing the surface quality of brittle materials in ultra-precision grinding. Journal of materials processing technology. 2005;168(1):75-82.
26. Malkin S, Hwang T. Grinding mechanisms for ceramics. CIRP Annals-Manufacturing Technology. 1996;45(2):569-80.
27. Pei Z, Billingsley S, Miura S. Grinding induced subsurface cracks in silicon wafers. International Journal of Machine Tools and Manufacture. 1999;39(7):1103-16.
28. Venkatesh VC, Sudin I. ADVANCES IN PRECISION GRINDING. Precision Engineering: McGraw Hill Professional, Access Engineering; 2007.
29. Wang L, Gao RX. Condition monitoring and control for intelligent manufacturing: Springer Science & Business Media; 2006.
30. Liu JH, Pei ZJ, Fisher GR. Grinding wheels for manufacturing of silicon wafers: A literature review. International Journal of Machine Tools and Manufacture. 2007 1//;47(1):1-13.
31. Stephenson D, Sun X, Zervos C. A study on ELID ultra precision grinding of optical glass with acoustic emission. International Journal of Machine Tools and Manufacture. 2006;46(10):1053-63.
32. Tong S, Gracewski S, Funkenbusch P. Measurement of the Preston coefficient of resin and bronze bond tools for deterministic microgrinding of glass. Precision engineering. 2006;30(2):115-22.
33. Ohmori H, Marinescu ID, Katahira K. Electrolytic In-Process Dressing (ELID) Technologies: Fundamentals and Applications: CRC Press; 2011.
34. P S. Machining of Optical Surfaces in Brittle Materials using an Ultra-precision Machine Tool: Cranfield University; 1995.
35. Shore P. Machining of optical surfaces in brittle materials using an ultra-precision machine tool: Cranfield University; 1995.
36. Grimme D, Rickens K, Zhao Q, Heinzel C. Dressing of coarse-grained diamond wheels for ductile machining of brittle materials. Towards Synthesis of Micro-/Nano-Systems: Springer; 2007. p. 305-7.
37. Zhao L, Liang Y, Stephenson D, Corbet J. Surface and Subsurface Integrity In Diamond Grinding of Optical Glass with Tetraform C. International Journal Of Machine Tools and Manufacture. 2007;47:2091-7.
38. Shaw MC. Principles of abrasive processing: Oxford University Press; 1996.
39. Shore P. «ELID» for efficient grinding of super smooth surfaces. IDR Industrial diamond review. 1993;53(559):318-22.
40. Zhong Z, Venkatesh V. Recent developments in grinding of advanced materials. The International Journal of Advanced Manufacturing Technology. 2009;41(5-6):468-80.

41. Oliveira JFG, Silva EJ, Guo C, Hashimoto F. Industrial challenges in grinding. CIRP Annals - Manufacturing Technology. 2009 //;58(2):663-80.
42. Fung Y-c, Tong P. Classical and computational solid mechanics: World scientific; 2001.
43. Chen F, Yin S, Huang H, Ohmori H. Fabrication of small aspheric moulds using single point inclined axis grinding. Precision Engineering. 2015;39:107-15.
44. Chen WK, Kuriyagawa T, Huang H, Yosihara N. Machining of micro aspherical mould inserts. Precision Engineering. 2005 7//;29(3):315-23.
45. E D, P B, J k. Materials and Processes in Manufacture. 9th ed: John Wiley & Sons Inc 2003.
46. Field M, Khales JF. Review of surface integrity of machined components: Defense Technical Information Center.; 1971.
47. Ayomoh MK, Abou-El-Hossein KA, Ghobashi SF, editors. Surface Roughness Prediction Using Numerical Scheme and Feedback Control. ASME 2015 International Manufacturing Science and Engineering Conference; 2015: American Society of Mechanical Engineers.
48. K S, E D, Sullivan P. Atlas of machined surfaces. 1st ed: Chapman and Hall publishers; 1990.
49. Inasaki I. Sensor fusion for monitoring and controlling grinding processes. The International Journal of Advanced Manufacturing Technology. 1999;15(10):730-6.
50. Lee D-E, Hwang I, Valente CM, Oliveira J, Dornfeld DA. Precision manufacturing process monitoring with acoustic emission. International Journal of Machine Tools and Manufacture. 2006;46(2):176-88.
51. Webster J, Dong W, Lindsay R. Raw acoustic emission signal analysis of grinding process. CIRP Annals-Manufacturing Technology. 1996;45(1):335-40.
52. Dornfeld D, Lee Y, Chang A. Monitoring of ultraprecision machining processes. The International Journal of Advanced Manufacturing Technology. 2003;21(8):571-8.
53. Bhaskaran J, Murugan M, Balashanmugam N, Chellamalai M. Monitoring of hard turning using acoustic emission signal. Journal of mechanical science and technology. 2012;26(2):609-15.
54. Sutowski P, Nadolny K, Kaplonek W. Monitoring of cylindrical grinding processes by use of a non-contact AE system. International Journal of Precision Engineering and Manufacturing. 2012;13(10):1737-43.
55. Teti R, Jemielniak K, O'Donnell G, Dornfeld D. Advanced monitoring of machining operations. CIRP Annals-Manufacturing Technology. 2010;59(2):717-39.
56. Grosse C. Acoustic Emission Testing. Berlin Heidelberg New York: Springer-Verlag; 2002.
57. Dornfeld D. Application of acoustic emission techniques in manufacturing. NDT & E International. 1992 12//;25(6):259-69.
58. Li X. A brief review: acoustic emission method for tool wear monitoring during turning. International Journal of Machine Tools and Manufacture. 2002;42(2):157-65.
59. Dimla DE. Sensor signals for tool-wear monitoring in metal cutting operations—a review of methods. International Journal of Machine Tools and Manufacture. 2000;40(8):1073-98.
60. Liao TW. Feature extraction and selection from acoustic emission signals with an application in grinding wheel condition monitoring. Engineering Applications of Artificial Intelligence. 2010;23(1):74-84.
61. Lezanski P. An intelligent system for grinding wheel condition monitoring. Journal of Materials Processing Technology. 2001 2/15/;109(3):258-63.

62. Zhang D, Bi G, Sun Z, Guo Y. Online monitoring of precision optics grinding using acoustic emission based on support vector machine. The International Journal of Advanced Manufacturing Technology. 2015:1-14.
63. Webster J, Marinescu I, Bennett R, Lindsay R. Acoustic Emission for Process Control and Monitoring of Surface Integrity during Grinding. CIRP Annals - Manufacturing Technology. 1994 //;43(1):299-304.
64. Wang Z, Willett P, DeAguiar PR, Webster J. Neural network detection of grinding burn from acoustic emission. International Journal of Machine Tools and Manufacture. 2001 1//;41(2):283-309.
65. Han X, Wu T. Analysis of acoustic emission in precision and high-efficiency grinding technology. The International Journal of Advanced Manufacturing Technology. 2013 2013/08/01;67(9-12):1997-2006. English.
66. Evans C, Pappas K, Xhafa F. Utilizing artificial neural networks and genetic algorithms to build an algo-trading model for intra-day foreign exchange speculation. Mathematical and Computer Modelling. 2013;58(5):1249-66.
67. SAP. Back propagation neural network 2015 [cited 2015 5 August]. Available from: http://help.sap.com/saphelp_hanaplatform/helpdata/en/dd/d236d66f394dea885f61cf5fdf8897/content.htm.
68. Wu S-j, Gebraeel N, Lawley M, Yih Y. A neural network integrated decision support system for condition-based optimal predictive maintenance policy. Systems, Man and Cybernetics, Part A: Systems and Humans, IEEE Transactions on. 2007;37(2):226-36.
69. Zhang G, Patuwo BE, Hu MY. Forecasting with artificial neural networks:: The state of the art. International journal of forecasting. 1998;14(1):35-62.
70. Kwak J-S, Ha M-K. Neural network approach for diagnosis of grinding operation by acoustic emission and power signals. Journal of Materials Processing Technology. 2004 3/30/;147(1):65-71.
71. Fuh K-H, Wang S-B. Force modeling and forecasting in creep feed grinding using improved bp neural network. International Journal of Machine Tools and Manufacture. 1997 8//;37(8):1167-78.
72. Masuzawa T, Tönshoff HK. Three-Dimensional Micromachining by Machine Tools. CIRP Annals - Manufacturing Technology. 1997 //;46(2):621-8.
73. Aslan N, Cebeci Y. Application of Box–Behnken design and response surface methodology for modeling of some Turkish coals. Fuel. 2007 1//;86(1–2):90-7.
74. Inasaki I. Grinding of Hard and Brittle Materials. CIRP Annals - Manufacturing Technology. 1987 //;36(2):463-71.
75. Agarwal S, Venkateswara Rao P. Predictive modeling of undeformed chip thickness in ceramic grinding. International Journal of Machine Tools and Manufacture. 2012 5//;56:59-68.
76. Kwak J-S. Application of Taguchi and response surface methodologies for geometric error in surface grinding process. International Journal of Machine Tools and Manufacture. 2005 3//;45(3):327-34.
77. Alao A-R, Konneh M. Surface finish prediction models for precision grinding of silicon. The International Journal of Advanced Manufacturing Technology. 2012 2012/02/01;58(9-12):949-67. English.
78. Montgomery D, Runger G, Hubele N. Engineering Statistics, 1998. John Wiley, New York.

79. Gonzalo O, Jauregi H, Uriarte L, de Lacalle LL. Prediction of specific force coefficients from a FEM cutting model. The International Journal of Advanced Manufacturing Technology. 2009;43(3-4):348-56.
80. Rowe WB. Principles of Modern Grinding Technology: Elsevier Science; 2013.
81. Boll SF. Suppression of acoustic noise in speech using spectral subtraction. Acoustics, Speech and Signal Processing, IEEE Transactions on. 1979;27(2):113-20.
82. Shen G, Wu Z, Zhang J. Advances in Acoustic Emission Technology: Proceedings of the World Conference on Acoustic Emission–2013: Springer New York; 2014. 694 p.
83. Subasi A. EEG signal classification using wavelet feature extraction and a mixture of expert model. Expert Systems with Applications. 2007;32(4):1084-93.
84. Liao TW, Ting C-F, Qu J, Blau PJ. A wavelet-based methodology for grinding wheel condition monitoring. International Journal of Machine Tools and Manufacture. 2007;47(3):580-92.

APPENDIX A: FULL ANOVA TABLE

Source	df	Seq. SS	Contribution (%)	Adjusted Ss	Adjusted MS	F-value	p-value
Model	6	35453.0	96.38	35453.0	5908.8	35.3	0.000
linear	3	23243.8	63.19	17857.8	5952.6	35.8	0.000
depth	1	4753.1	12.12	5958.7	5958.7	35.83	0.000
feed	1	17112.5	46.52	11761.9	1176.1	70.73	0.000
speed	1	1378.1	3.75	6582.0	96502.0	39.10	0.000
square	1	2503.0	6.8	2503.0	2503.0	15.05	0.005
feed*feed	1	2503.0	6.8	2503.0	2503.0	15.05	0.005
2-way interaction	2	9706.3	26.39	9706.3	4853.1	29.18	0.000
Depth*speed	1	3306.3	8.9	3306.3	3306.3	19.88	0.002
Feed*speed	1	6400.0	17.4	6400.0	6400.0	38.49	0.000
Residual Error	8	1330.4	3.62	1330.4	166.3		
Lack of fit	6	1263.7	3.4	1263.7	210.6	6.32	0.143
Pure error	2	66.7	0.18	66.7	33.3		
Total	14	36783.3	100				

APPENDIX B: SPECTRAL VALIDATION TABLE

Feature	Raw feature correlation value	Spectral subtracted feature correlation value
F3	-0.22	-0.5
F4	-0.17	-0.3
F9	-0.17	-0.1
F10	0.08	0.1
E3	-0.20	-0.4
E4	-0.15	-0.3
Et	-0.18	-0.3
S3	-0.23	-0.4
S4	-0.16	-0.3

APPENDIX C: SAPHANA CODES FOR ANN TRAINING AND PREDICTION

```
Training

-- cleanup
DROP TYPE "T_DATA_GOODNESS";
DROP TYPE "T_PARAMS_GOODNESS";
DROP TYPE "T_STATS_GOODNESS";
DROP TYPE "T_MODEL_GOODNESS";
DROP TABLE "SIGNATURE_GOODNESS";
CALL "SYS"."AFLLANG_WRAPPER_PROCEDURE_DROP"('MASTER_KA',
'P_BPNN_M');
DROP VIEW "V_DATA_GOODNESS";
DROP VIEW "V_DATA1_GOODNESS";
DROP TABLE "STATS_GOODNESS";
DROP TABLE "MODEL_GOODNESS";

-- procedure setup
CREATE TYPE "T_DATA_GOODNESS" AS TABLE (

            "DEPTH" DOUBLE,
         "FEED" DOUBLE,
         "SPEED" DOUBLE,
         "s3" DOUBLE,
         "et" DOUBLE,
         "e3" DOUBLE,
            "f4" DOUBLE,
            "f3" DOUBLE,
         "rms" DOUBLE,
            --"std" DOUBLE,
         "mean" DOUBLE,
         "response" DOUBLE

     );

CREATE TYPE "T_PARAMS_GOODNESS" AS TABLE ("NAME" VARCHAR(60),
"INTARGS" INTEGER, "DOUBLEARGS" DOUBLE, "STRINGARGS" VARCHAR(100));
CREATE TYPE "T_STATS_GOODNESS" AS TABLE ("NAME" VARCHAR(100), "VALUE"
DOUBLE);
CREATE TYPE "T_MODEL_GOODNESS" AS TABLE ("NAME" VARCHAR(100), "MODEL"
CLOB);

CREATE COLUMN TABLE "SIGNATURE_GOODNESS" ("POSITION" INTEGER,
"SCHEMA_NAME" VARCHAR(100), "TYPE_NAME" VARCHAR(100),
"PARAMETER_TYPE" VARCHAR(100));
INSERT INTO "SIGNATURE_GOODNESS" VALUES (1, 'MASTER_KA',
'T_DATA_GOODNESS', 'IN');
INSERT INTO "SIGNATURE_GOODNESS" VALUES (2, 'MASTER_KA',
'T_PARAMS_GOODNESS', 'IN');
```

```sql
INSERT INTO "SIGNATURE_GOODNESS" VALUES (3, 'MASTER_KA', 'T_STATS_GOODNESS', 'OUT');
INSERT INTO "SIGNATURE_GOODNESS" VALUES (4, 'MASTER_KA', 'T_MODEL_GOODNESS', 'OUT');

CALL "SYS"."AFLLANG_WRAPPER_PROCEDURE_CREATE"('AFLPAL', 'CREATEBPNN', 'MASTER_KA', 'P_BPNN_M', "SIGNATURE_GOODNESS");

-- data & view setup
CREATE VIEW "MASTER_KA"."V_DATA1_GOODNESS" AS
 SELECT TOP 10

            "DEPTH" ,
         "FEED" ,
         "SPEED" ,
         "s3" ,
         "et" ,
         "e3" ,
            "f4" ,
            "f3" ,
         "rms" ,
            --"std" ,
         "mean" ,
         "response"
FROM "MASTER_KA"."NN_GOODNESS"; --(Predict 15 days)

CREATE VIEW "MASTER_KA"."V_DATA_GOODNESS" AS
 SELECT
      *
FROM "MASTER_KA"."V_DATA1_GOODNESS";

CREATE COLUMN TABLE "STATS_GOODNESS" LIKE "T_STATS_GOODNESS";
CREATE COLUMN TABLE "MODEL_GOODNESS" LIKE "T_MODEL_GOODNESS";

-- runtime
DROP TABLE "#PARAMS_GOODNESS";
CREATE LOCAL TEMPORARY COLUMN TABLE "#PARAMS_GOODNESS" LIKE "T_PARAMS_GOODNESS";
INSERT INTO "#PARAMS_GOODNESS" VALUES ('HIDDEN_LAYER_ACTIVE_FUNC', 3, null, null);
INSERT INTO "#PARAMS_GOODNESS" VALUES ('OUTPUT_LAYER_ACTIVE_FUNC', 3, null, null);
INSERT INTO "#PARAMS_GOODNESS" VALUES ('LEARNING_RATE', null, 0.1, null);
INSERT INTO "#PARAMS_GOODNESS" VALUES ('MOMENTUM_FACTOR', null, 0.2, null);
INSERT INTO "#PARAMS_GOODNESS" VALUES ('HIDDEN_LAYER_SIZE', null, null, '20');
INSERT INTO "#PARAMS_GOODNESS" VALUES ('MAX_ITERATION', 500000, null, null);
INSERT INTO "#PARAMS_GOODNESS" VALUES ('FUNCTIONALITY', 1, null, null); -- 0:Classification; 1:Regression
INSERT INTO "#PARAMS_GOODNESS" VALUES ('TARGET_COLUMN_NUM', 1, null, null);
INSERT INTO "#PARAMS_GOODNESS" VALUES ('TRAINING_STYLE', 0, null, null); -- 0:Batch; 1:Stochastic
```

```sql
--INSERT INTO "#PARAMS_GOODNESS" VALUES ('NORMALIZATION', 1, null, null); -- 0:Normal; 1:Z-transform; 2:Scalar
INSERT INTO "#PARAMS_GOODNESS" VALUES ('WEIGHT_INIT', 1, null, null);
-- 0:all zeros; 1: normal; 2: uniform
--INSERT INTO "#PARAMS_GOODNESS" VALUES ('CATEGORY_COL', 0, null, null);

TRUNCATE TABLE "STATS_GOODNESS";
TRUNCATE TABLE "MODEL_GOODNESS";

CALL "P_BPNN_M" ("V_DATA_GOODNESS", "#PARAMS_GOODNESS", "STATS_GOODNESS", "MODEL_GOODNESS") WITH OVERVIEW;

SELECT * FROM "STATS_GOODNESS";
SELECT * FROM "MODEL_GOODNESS"
```

```sql
PREDICT

-- cleanup
DROP TYPE "T_DATA_P_GOODNESS";
DROP TYPE "T_PREDICT_GOODNESS";
DROP TABLE "SIGNATURE_GOODNESS";
CALL "SYS"."AFLLANG_WRAPPER_PROCEDURE_DROP"('MASTER_KA', 'P_BPNN_P');
DROP TABLE "DATA_P_GOODNESS";
DROP TABLE "PREDICT_GOODNESS";
DROP VIEW "DATA_PV_GOODNESS";

-- procedure setup
CREATE TYPE "T_DATA_P_GOODNESS" AS TABLE (
            "ID" INT,
         "DEPTH" DOUBLE,
         "FEED" DOUBLE,
         "SPEED" DOUBLE,
         "s3" DOUBLE,
         "et" DOUBLE,
         "e3" DOUBLE,
            "f4" DOUBLE,
            "f3" DOUBLE,
         "rms" DOUBLE,
           -- "std" DOUBLE,
         "mean" DOUBLE


         );

CREATE TYPE "T_PREDICT_GOODNESS" AS TABLE ("ID" INT, "response" DOUBLE);
```

```
CREATE COLUMN TABLE "SIGNATURE_GOODNESS" ("POSITION" INTEGER,
"SCHEMA_NAME" VARCHAR(100), "TYPE_NAME" VARCHAR(100),
"PARAMETER_TYPE" VARCHAR(100));
INSERT INTO "SIGNATURE_GOODNESS" VALUES (1, 'MASTER_KA',
'T_DATA_P_GOODNESS', 'IN');
INSERT INTO "SIGNATURE_GOODNESS" VALUES (2, 'MASTER_KA',
'T_MODEL_GOODNESS', 'IN');
INSERT INTO "SIGNATURE_GOODNESS" VALUES (3, 'MASTER_KA',
'T_PARAMS_GOODNESS', 'IN');
INSERT INTO "SIGNATURE_GOODNESS" VALUES (4, 'MASTER_KA',
'T_PREDICT_GOODNESS', 'OUT');

CALL "SYS"."AFLLANG_WRAPPER_PROCEDURE_CREATE"('AFLPAL',
'PREDICTWITHBPNN', 'MASTER_KAYODE', 'P_BPNN_P',
"SIGNATURE_GOODNESS");

-- data & view setup
CREATE COLUMN TABLE "DATA_P_GOODNESS"(
         -- "ID" INT not null primary key generated by default as
IDENTITY,
          "ID" INT,
 "DEPTH" DOUBLE,
         "FEED" DOUBLE,
         "SPEED" DOUBLE,
         "s3" DOUBLE,
         "et" DOUBLE,
         "e3" DOUBLE,
            "f4" DOUBLE,
            "f3" DOUBLE,
         "rms" DOUBLE,
           -- "std" DOUBLE,
         "mean" DOUBLE

        );

Insert Into "DATA_P_GOODNESS" (
       "ID",
             "DEPTH" ,
         "FEED" ,
         "SPEED" ,
         "s3" ,
         "et" ,
         "e3" ,
            "f4" ,
            "f3" ,
         "rms" ,
           -- "std" ,
         "mean"

       )
 (SELECT
       "ID",
        "DEPTH" ,
         "FEED" ,
         "SPEED" ,
         "s3" ,
```

```
         "et" ,
         "e3" ,
            "f4" ,
            "f3" ,
         "rms" ,
            --"std" ,
         "mean"

FROM "MASTER_KAYODE"."NN_GOODNESS" WHERE "ID" > 10); --(Predict 15
days)


CREATE VIEW "MASTER_KA"."DATA_PV_GOODNESS" AS
 SELECT
      *
 FROM "MASTER_KA"."DATA_P_GOODNESS";

CREATE COLUMN TABLE "PREDICT_GOODNESS" LIKE "T_PREDICT_GOODNESS";

-- runtime
DROP TABLE "#PARAMS_GOODNESS";
CREATE LOCAL TEMPORARY COLUMN TABLE "#PARAMS_GOODNESS" LIKE
"T_PARAMS_GOODNESS";

TRUNCATE TABLE "PREDICT_GOODNESS";

CALL "P_BPNN_P" ("DATA_PV_GOODNESS", "MODEL_GOODNESS",
"#PARAMS_GOODNESS", "PREDICT_GOODNESS") WITH OVERVIEW;


SELECT ID, "response" FROM "PREDICT_GOODNESS";

SELECT ID, "response", ("response" * (320 - 130) + 130) as RES FROM
"PREDICT_GOODNESS";
```

APPENDIX D: SOME MATLAB CODES FOR SIGNAL ANALYSIS

```
% Plot raw AE signals.
t=(0.0000005:0.0000005:.1);
subplot(3,1,1); plot(t,res(:,1));
ylabel('Raw AE(V)');
title('01, Ra(130nm), d(5µm), f(1mm/min), s(15000rpm)')

subplot(3,1,2); plot(t,res(:,9));
ylabel('Raw AE(V)');
title('09, Ra(230nm), d(5µm), f(3mm/min), s(300000rpm)')

subplot(3,1,3); plot(t,res(:,5));
xlabel('Time(sec)'); ylabel('Raw AE(V)');
title('05, Ra(220nm), d(8µm), f(3mm/min), s(450000rpm)');

ts=(0:0.0000005:.0000995);
subplot(3,1,1), plot(ts,res500rms(1:200,1));
ylabel('AErms(V)');
title('01, Ra(130nm), d(5µm), f(1mm/min), s(15000rpm)')

ts=(0:0.0000005:.0000995);
subplot(3,1,2), plot(ts,res500rms(1:200,9));
ylabel('AErms(V)');
title('09, Ra(230nm), d(5µm), f(3mm/min), s(30000rpm)')

ts=(0:0.0000005:.0000995);
subplot(3,1,3), plot(ts,res500rms(1:200,5));
ylabel('AErms(V)');
title('05, Ra(220nm), d(8µm), f(3mm/min), s(45000rpm)')



%wavelet decomposition levels
[c,l]= wavedec(res(:,15),7,'db3');
A7=wrcoef('a',c,l,'db3',7);
D1=wrcoef('d',c,l,'db3',1);
D2=wrcoef('d',c,l,'db3',2);
D3=wrcoef('d',c,l,'db3',3);
D4=wrcoef('d',c,l,'db3',4);
D5=wrcoef('d',c,l,'db3',5);
D6=wrcoef('d',c,l,'db3',6);
D7=wrcoef('d',c,l,'db3',7);



%plot the wavelet decomposition levels
fs=2000000; tp=1/fs; tr=linspace(tp,0.1,200000);
X=tr;

%subplot for wavelet decomposition
subplot(9,1,1);plot(X,FINALT(:,15));
subplot(9,1,2);plot(X,A7);
```

```
subplot(9,1,3);plot(X,D1);
subplot(9,1,4);plot(X,D2);
subplot(9,1,5);plot(X,D3);
subplot(9,1,6);plot(X,D4);
subplot(9,1,7);plot(X,D5);
subplot(9,1,8);plot(X,D6);
subplot(9,1,9);plot(X,D7);
% Feature category 1
f3= mean (abs (D3));
f4= mean (abs (D4));
f9= f3/f4;
f10= mean (abs (D2))/mean(abs(D5));

d1=D1.*D1; d2=D2.*D2; d3=D3.*D3; d4=D4.*D4; d5=D5.*D5; d6=D6.*D6;
d7=D7.*D7;
a7=A7.*A7;
tp=1/fs; tm=tp:0.0000005:0.1;

% Feature category 2
e1= trapz (tm,d1);
e2= trapz(tm,d2);
e3= trapz(tm,d3);
e4= trapz(tm,d4);
e5= trapz(tm,d5);
e6=trapz(tm,d6);
e7=trapz(tm,d7);
e8=trapz(tm,a7);
et=e1+e2+e3+e4+e5+e6+e7+e8;

% Features category 3
s3=std(abs(D3));
s4=std(abs(D4));

% Total feature set
setfinalt15=[f3;f4;f9;f10;e3;e4;et;s3;s4];


t=(0.0000005:0.0000005:.1);
subplot(3,1,1); plot(t,res(:,1));
ylabel('Raw AE(V)');
title('01, Ra(130nm), d(5µm), f(1mm/min), s(15000rpm)')

subplot(3,1,2); plot(t,res(:,9));
ylabel('Raw AE(V)');
title('09, Ra(230nm), d(5µm), f(3mm/min), s(300000rpm)')

subplot(3,1,3); plot(t,res(:,5));
xlabel('Time(sec)'); ylabel('Raw AE(V)');
title('05, Ra(220nm), d(8µm), f(3mm/min), s(450000rpm)');

ts=(0:0.0000005:.0000995);
subplot(3,1,1), plot(ts,res500rms(1:200,1));
ylabel('AErms(V)');
title('01, Ra(130nm), d(5µm), f(1mm/min), s(15000rpm)')

ts=(0:0.0000005:.0000995);
```

```
subplot(3,1,2), plot(ts,res500rms(1:200,9));
ylabel('AErms(V)');
title('09, Ra(230nm), d(5µm), f(3mm/min), s(30000rpm)')

ts=(0:0.0000005:.0000995);
subplot(3,1,3), plot(ts,res500rms(1:200,5));
ylabel('AErms(V)');
title('05, Ra(220nm), d(8µm), f(3mm/min), s(45000rpm)')
```

APPENDIX E: LABVIEW SOFTWARE DESIGN